Process Design and Modeling of the Horizontal Ribbon Growth Method for Continuous Production of Silicon Wafers

Submitted in partial fulfillment of the requirements for

the degree of

Doctor of Philosophy

in

Department of Chemical Engineering

Jiaying Ke

B.S., Chemical Engineering, Purdue University

Carnegie Mellon University

Pittsburgh, PA

April, 2018

Acknowledgments

First and foremost I would like to express my sincerest gratitude to my advisor and mentor, Professor B. Erik Ydstie, for his valuable and insightful guidance, patience, encouraging, and support during the past five years of my phd studies. I would not be able to make it without his kindness, help, and support.

I am grateful to my co-advisor, Professor Aditya S. Khair and my doctoral committee members, Lisa Porter, Chrysanthos E. Gounaris, John Kitchin. I would also like to acknowledge the undergraduate and graduate students involved in the experiments, some of the results of whom are included in this thesis.

I would like to thank my undergraduate research advisor at Purdue university, Professor Chongli Yuan. Dr. Yuan introduced me for the first time to scientific research and motivated me to pursue a Ph.D. I also want thank the National Science Foundation (CBET-1438231) and CAPD for the financial support of my doctoral project.

Finally, I have to thank all my friends in Pittsburgh and China, my friends back from Purdue, as well as the amazing Ydstie research group. I had so many joyful memories during the past five years. I would especially like to thank Nikos Lappas who stood by me through the difficulties of the Ph.D. Last but not least, I would like to thank my family in China for their unconditional love and support.

Jiaying Ke

This thesis is dedicated to my parents, my family, and my friends.

Abstract

This thesis contains theoretical development and experimental verification of the Horizontal Ribbon Growth (HRG) method for continuous silicon wafer manufacturing. In the HRG process, heat is removed through the top surface of the molten silicon pool, meanwhile, a thin silicon solid sheet is produced and extracted continuously, in this way minimizing material losses. We assessed three technical issues regarding the design and operation of the proposed process using mathematical modeling approaches: the overall process modeling, corrugated wavy interface, and front wedge formation.

A Mathematical field model that governs the mass, momentum and energy balances is developed to provide a platform for alternative cooling/heating setups evaluation, as well as, various candidate process designs. The results of our study showed a relationship between the pulling velocity and the thickness of the ribbon that is qualitatively in agreement with available experimental results.

A linear stability theory is used to investigate the wavy instability occurred at the wafer-melt interface. The conditions for the onset of stability were identified theoretically and numerically on the basis of diffusion-convection equations for the thermal, solutal fields coupled with the Navier-Stokes equation describing the flow field in the molten pool near the interface. The interface stability conditions of the system under different operating conditions were

examined to establish the optimal range of operation.

A cellular automata algorithm is coupled with finite difference scheme to study to evolution of crystallization for the system. The formation of dendrites at the crystal front, non-smooth/unstable solid-liquid interface, and sharp wedge were simulated. We demonstrate a more homogeneous segregation of impurities in the bottom portion of the resulting wafer, while an aggressive cooling rate results in an unsmooth interface formation.

Two experimental pilot facilities were developed and utilized to validate theoretical findings and study the scale-up of the proposed process. In particular, an ice machine was built as a prototype to examine the feasibility of the process and test different preliminary design ideas, while a silicon pilot facility is utilized for experimenting with extracting silicon wafers continuously from the melt.

Contents

Acknowledgments **i**

Abstract **iii**

1 Introduction **1**

1.1 Silicon photovoltaic industry 1

1.2 Alternative Direct Kerfless Ribbon Techniques 4

1.2.1 Vertical Ribbon Growth (VRG) Methods 4

1.2.2 Horizontal Ribbon Growth Method 5

1.3 Outline of the thesis 6

2 The Horizontal Ribbon Growth Process **8**

2.1 Introduction 8

2.2 Literature review of the HRG process 9

2.3 Open Challenges in the HRG process 15

3 Development of the Ice-Water HRG process **18**

3.1 Introduction 18

3.2 Ice-water HRG Experiment 19

3.3 Solidification in the HRG process 23

3.4 Mathematical model of the HRG process 25

3.4.1 Governing Equations 25

3.4.2 Approximation of Solid Phase 26
3.4.3 Mushy Zone Theory 27
3.4.4 Discontinuity in physical properties 28
3.4.5 Flow and thermal boundary conditions 29
3.4.6 Numerical Solution 30
3.5 COMSOL Simulation and Experimental Results 30
3.5.1 Steady State Simulation 30
3.6 Conclusions and contributions 33

4 Stability Analysis of the crystal interface in the context of the HRG process 35

4.1 Introduction 35
4.2 Mathematical model of the HRG process 38
4.3 Non-dimensionalization and base state solution 41
4.4 Linear Stability Analysis of the interface 45
4.4.1 Derivation Outline 45
4.4.2 Dispersion Relation 48
4.4.3 Neutral Stability Results 57
4.5 Conclusions and contributions 60

5 A cellular automata approach for simulation of crystal growth 62

5.1 Introduction and Literature Review 62
5.2 Cellular Automata model and numerical algorithm 64
5.2.1 Numerical Solution Algorithm 71
5.2.2 Results and discussion 72
5.3 Kinetic Controlled Growth 79
5.3.1 Numerical Solution Algorithm 83
5.3.2 Results and discussion 84

5.4 Conclusion and Contribution 84

6 Process design and experimental verification 87

6.1 Silicon HRG Experiment 87

6.2 Crucible Design 88

6.3 Seed attachment Design 94

6.4 Conclusions and Contributions 95

7 Concluding Remarks 96

7.1 Thesis Summary 96

7.2 Future Directions 99

7.2.1 Mathematical modeling of the cooling system and insulation 99

7.2.2 Thickness control, process stabilization, and production optimization 99

7.2.3 Experimental Development 100

A Validity of neglecting velocity terms for the ice-water system 103

B Heat transfer coefficient estimation for ice-water system 104

C Eigenvalue Convergence 105

D Silicon HRG system Experiment 106

E Water-Ice HRG system Experiment 114

F Preliminary Control design 118

Bibliography 128

List of Figures

1.1 Renewable Energy Share of Total Final Energy Consumption, 2015 1
1.2 Solar PV Global Capacity and Annual Additions, 2006-2016 . 2
1.3 Cost Distribution of Typical Silicon PV model 3
1.4 Schematic Drawing of Vertical and Horizontal Ribbon growth technique: solidification interface and heat loss orientation . . 5
1.5 Schematic Drawing of RGS Method 6

2.1 Bleil's HRG design and obtained wafer 10
2.2 Schematic drawing of Kudo's HRG system 10
2.3 Stream function contours near the upper and lower meniscus observed by Dagglou 12
2.4 Two hydrostatically feasible operation conditions to produce a 6 cm long and 400 μm thick wafer observed by Oliveros 13
2.5 BP Solar HRG design and melt trial experiment 13
2.7 Silicon Ribbon produced through the HRG process 16

3.1 Ice Machine Side View 20
3.2 Ice Machine Top View 20
3.3 Ice Wafer Produced using a HRG system 22

3.4 Proof-of-concept experiments demonstrating the problem of meniscus spill over by the ice-water system 23
3.5 Schematic drawing of Ribbon illustrating triangular shape wedge with linear solid liquid interface 24
3.6 Ice Wafer Process Geomoetry and finite-element mesh used in calculation 25
3.7 Temperature Profile and Isotherms of the Proposed Ice Wafer Process 31
3.8 Velocity Profile and Streamlines of the Proposed Ice Wafer Process 31
3.9 Steady State simulation result for the Ice wafer process 32
3.10 Correlation between Pulling Velocity and Thickness of the wafer for the Ice Wafer Process 33

4.1 The Schematic Sketch for the HRG process 38
4.2 Typical velocity, concentration, and temperature fields near the HRG interface 39
4.3 Dimensionless Profiles for W=100, G_l=300 K/cm, $C_\infty = 10ppm$, Pe_l=1.073,0.7153,0.1431 correspond to V_p=150, 100, 20 mm/min, respectively 44
4.4 Representation of Stability Analysis 45
4.5 Dimensionless dispersion relation for W=300, G_l=300 K/cm, V_p=20 mm/min, $C_\infty = 100ppm$ 50
4.6 Growth Rate for Pulling Velocity=120 mm/min, Wedge Factor=500 and $k = 30$ with different C_∞ 52
4.7 Dimensionless dispersion relation for different wedge factor at V_p=20 mm/min, Gl=300 K/cm, C_∞=100 ppm 53
4.8 Dimensionless dispersion relation for different pulling velocity at W=1500, Gl=300 K/cm, C_∞=100 ppm 54

4.9 Dimensionless dispersion relation for different temperature gradient at V_p=150 mm/min, W=1500, C_∞=100 ppm 56
4.10 The influence of the wedge factor(W) and pulling velocity(V_P) on the impurity concentration neutral curve (Gl=200 K/cm) . 60

5.1 Schematic representation of the solid/liquid interface morphology: Influence of solute composition 65
5.2 Nucleation probability density function 70
5.3 Tip Velocity as a function of time for different cooling conditions 72
5.4 Tip concentration as a function of time for different cooling conditions 73
5.5 Distribution of solute in the wafer (mild cooling rate) 73
5.6 Impurity concentration profiles in the melt at different stages of the crystallization 74
5.7 Cell States evolution with high level impurities (7% aluminum) and high cooling rate 75
5.8 Cell States evolution with high level impurities (7% aluminum) and mild cooling rate 76
5.9 Cell States evolution with high level impurities (7% aluminum) and low cooling rate 77
5.10 Simulated evolution of a single dendritic growth of Si-7%Al in a static melt 79
5.11 Steady-state Tip Velocity as a function of mesh size 81
5.12 Kinetic Coefficient β as a function of undercooling rate and misalignment angle 82
5.13 Concentration Profiles for different undercooling rate 85
5.14 Comparison of steady-state tip parameters with different undercooling rate for Silicon melt with 50 ppm aluminum 86

6.1 Melt trial conducted using graphite crucible with partially covered lid 89
6.2 Melt trial conducted using graphite crucible with fully covered lid, flexible door, and machined exit design 90
6.3 Melt trial conducted using graphite crucible and quartz crucible 91
6.4 Updated version Graphite crucible Design 93
6.5 Temperature Plateau during constant heating ($40KW$) indicating melting process 94
6.6 Melt trials for different adhesive samples 95

C.1 Eigenvalue for C_∞=50ppm, V_p=50 mm/min, W=300, G_l=200 K/cm, k=5 105

D.1 Graphite Lid Design 107
D.2 Graphite Crucible Design 108
D.3 Graphite Crucible Door Design 109

E.1 Water-Ice system Crucible Design 115
E.2 Water-Ice system main bath top view 116
E.3 Water-Ice pulling system top view 117
E.4 Water-Ice pulling system side view 117

F.1 Transfer Function Estimation from step change analysis (Pulling Velocity) 120
F.2 Transfer Function Estimation from step change analysis (Cooling Temperature) 120
F.3 RGA analysis at different operating conditions 121
F.4 The proposed control Scheme for the HRG process 123
F.5 The outputs of the model with PI control 124

F.6 The inputs of the model with PI control 125

F.7 The outputs of adaptive control 126

F.8 The inputs of adaptive control 126

F.9 Step change test for adaptive control 127

List of Tables

3.1 Material Properties Comparison for water and silicon 19

3.2 Material Properties and Parameters used in the COMSOL model 31

4.1 Segregation Coefficient of Impurities in silicon 36

4.2 Material Properties and Parameters used in the linear stability model 51

B.1 Material Properties and Parameters used for the estimation . 104

D.1 HRG Heating Procedure 111

Chapter 1

Introduction

1.1 Silicon photovoltaic industry

The growing demand for energy in conjunction with the increasing threat of global warming necessitates cleaner and cheaper energy resources to replace non-renewable fossil fuels [42]. As shown in Figure 1.1, the renewable energy resources provided around 19.3% of global total energy consumption as of 2015 [43].

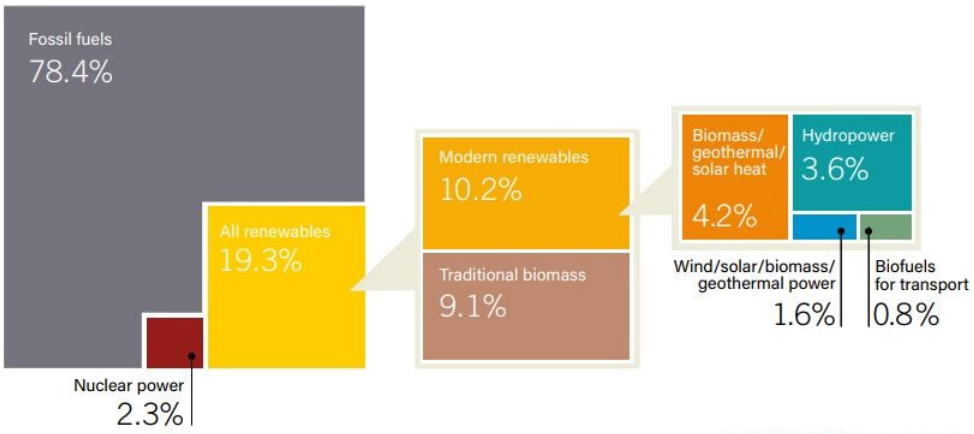

Figure 1.1: Renewable Energy Share of Total Final Energy Consumption, 2015. Graphic taken from the Renewables 2017 Global Status Report [43].

The silicon based photo-voltaic system is one of the most promising re-

newable energy resources, as it converts energy directly from photons in the sunlight into electricity via photoelectric effect. Its application has grown rapidly during the past three decades as reduced production costs due to scalability, investment supported by governments, and improved manufacturing processes. The capacity of solar PV continues to grow. Figure 1.2 shows that the global Solar PV capacity reached 303GW by the end of 2016 and a 33% annual increase.

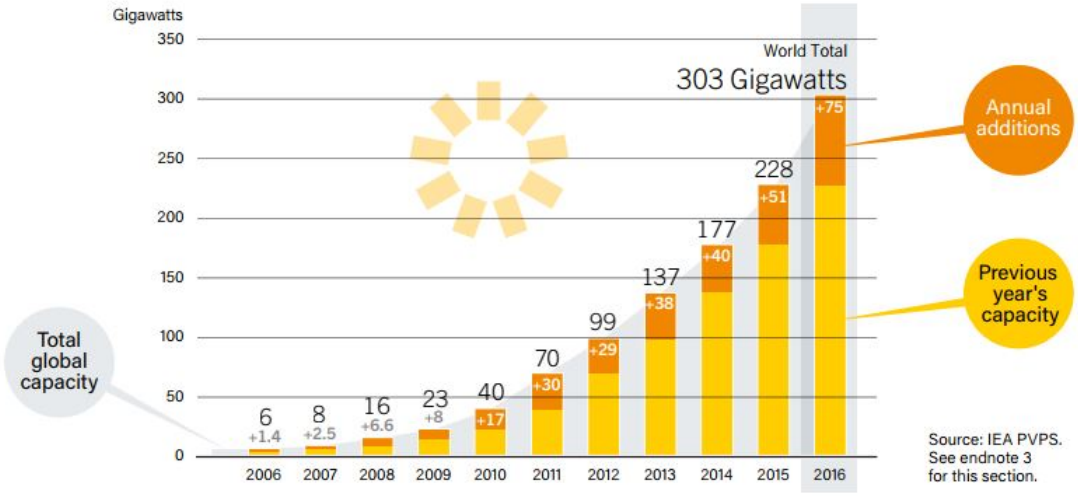

Figure 1.2: Solar PV Global Capacity and Annual Additions, 2006-2016. Graphic taken from the Renewables 2017 Global Status Report [43].

The cost of solar panels has been reduced significantly during the past 40 years, from \$77/watt in 1977 to around \$0.64/watt today. Despite this fact, the solar energy costs are still considered high compared with other renewable energy resources, such as wind energy or biomass. Meanwhile, the cost of PV is also vulnerable towards policy change or measures compared with traditional fossil fuels.

Two essential factors arise for solar energy to be more competitive compare with traditional energy resources: cost and efficiency. As shown in Figure 1.3, ingot and wafer processes account for 28% of silicon PV model cost, and these

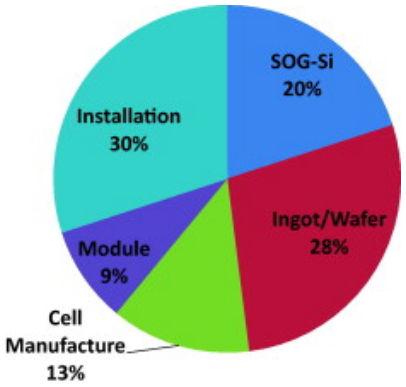

Figure 1.3: Cost Distribution of Typical Silicon PV model. Graphic taken from Ranjan et al. [42].

two steps also play important roles in the quality of solar cell. Traditional silicon growth process begins with ingot technology, such as the Czochralski (CZ) process. In the CZ process, metallurgical grade silicon is melted in a large furnace and then monocrystalline ingot is grown from the melt by slowly pulling out the seed rotationally.

The major limitations of the approach involve: High material losses in the wafer process (up to 55% [40]), expensive abrasive slurries, and micro-defects introduced on the cutting surface due to the sawing process that is required in the entirety of the ingot based processes; This process has low production rates: Typical industrial CZ processes produce a cylindrical single-crystal silicon ingot with a diameter of 200-300 mm and a production rate of 1-2 mm/min.

Thus, development of new technologies that can simplify the ingot and wafer processes to rapidly grow high quality wafer directly from the melt (kerfless wafering) could reduce the cost of solar cell significantly.

1.2 Alternative Direct Kerfless Ribbon Techniques

1.2.1 Vertical Ribbon Growth (VRG) Methods

The dendritic web (WEB) process was firstly reported by Dermatis and Faust [17] in 1963. In the WEB process, a dendrite silicon seed is inserted into a supercooled melt to form a button. Then the seed is raised to allow propagation of two secondary dendrites on each end of the button pointing into the melt. A frame is formed from the button and dendrites to support the formation of a liquid film which then crystallizes to a thin web of a thickness around $100 - 200\ um$. A production speed around 5cm/min can be reached with $6-8m$ in length, $2-4cm$ in width, and efficiency can reach around 15.5% [47]. This process requires detailed thermal field control to ensure the initial web formation and steady dendrites propagation. It has not been successfully industrialized.

The edge-defined film-fed growth (EFG) process was firstly reported by Ciszek [10] in 1972, and it was one of the few ribbon growth technique commercialized. The EFG process utilizes a shaping die (usually made of graphite or coated with silicon carbide) to control the geometry of the ribbon, where silicon is fed and raised via capillary action. A seed crystal is inserted vertically to initiate crystallization from the top of the shaping die. The thickness of the produced ribbon is determined by the width of the die edge, meniscus shape, and rate of heat loss. However, the quality of the produced ribbon is significantly affected by the utilization of the shaping die and the cell efficiencies are usually limited to $14 - 16\%$ [27]. Typical vertical ribbon growth methods result a pulling rate around $1-2$ cm/min. Although the pulling rate of vertical ribbon growth (VRG) methods are higher than traditional ingot technologies,

the overall throughputs are still not competitive due to their limitation on small liquid-solid interface, as shown in Figure 1.4.

1.2.2 Horizontal Ribbon Growth Method

Several ribbon growth technologies with large solid-liquid interface area and heat removal perpendicular to the pulling direction have been developed to accommodate the drawbacks of vertical ribbon growth techniques. As shown in Figure 1.4, the direction of pulling and heat dissipation distinguishes vertical and horizontal ribbon growth processes.

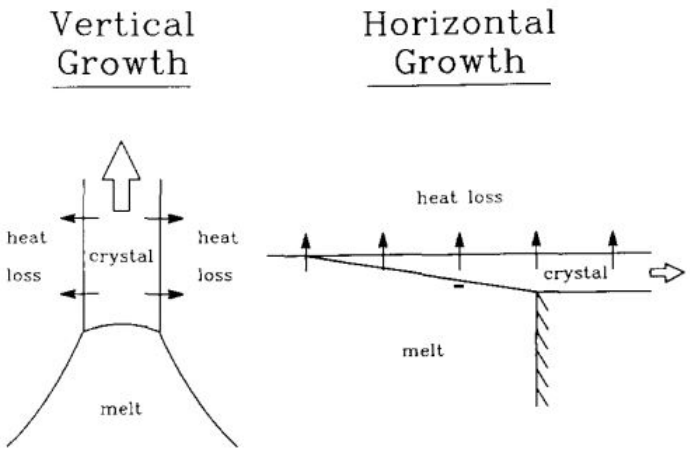

Figure 1.4: Schematic Drawing of Vertical and Horizontal Ribbon growth technique: solidification interface and heat loss orientation. Graphic taken from Thomas and Brown [50].

Direct ribbon growth on substrate (RGS) was developed by Lange and Schwirtlich [30] in 1990. As shown in Figure 1.5, a shaping die is sitting on top of a moving substrate, and is used to melt the silicon as well as to shape the solidified ribbon. The produced ribbon is pulled away from the bottom of the melt with the substrate. The idea is to obtain a wedge shaped silicon ribbon and extend the solid-liquid interface to guarantee a high rate of extraction of latent heat. Silicon ribbon has been obtained via RGS process with production

speed of 65 mm/min, width around 10 cm, and 300μm in thickness. Although the RGS method has attractive thoughtput, the use of a substrate resulted in limitations for the produced wafer in impurities and grain size.

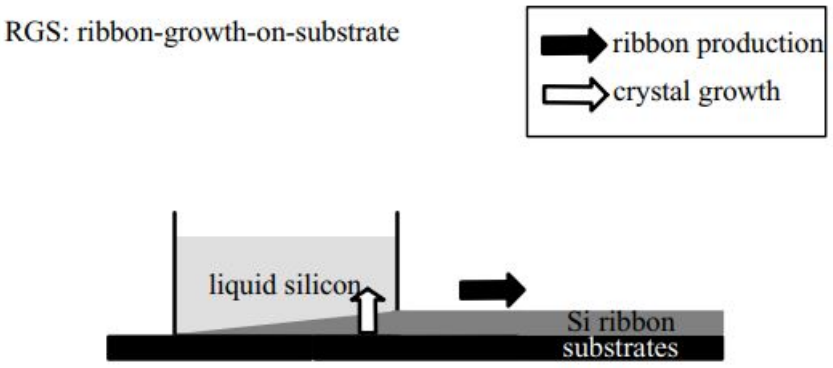

Figure 1.5: Schematic Drawing of RGS Method. Graphic taken from Schonecker et al. [45].

1.3 Outline of the thesis

In chapter 2, we provide a detailed literature review on the development of horizontal ribbon growth process and discuss the current technical difficulties encountered.

In chapter 3, we develop an ice-water system to prove the HRG concept by generating ice wafer continuously from a water bath. A 2-D mathematical model is built to study how process design impact major characteristics of the Horizontal Ribbon Growth (HRG) process. The model describes the interaction of fluid flow, heat transfer, impurities and phase change in the system. The current model shows a relationship between the pulling velocity and the thickness of the ribbon that is qualitatively in agreement with experimental results and theoretical prediction.

In chapter 4, we quantify the effects of different operating conditions on the stability of the crystallization interface in the horizontal ribbon growth

(HRG) process. Specifically, we perform a linear stability analysis of the base state, and we derive the profiles for thermal, solutal and flow fields with regard to small-amplitude normal mode perturbations of the base state. Within the velocity boundary layer induced by the removal of solid ribbon, a linear Couette flow is assumed; at the outer edge of the boundary layer, all perturbations are assumed to dissipate. Critical operating conditions and the unstable modes have been identified. To that end, we demonstrate that fast pulling velocity (greater than 100 mm/min), low wedge factors (the ratio of the length to the thickness of the wafer is less than 500), and insufficient heat removal (temperature gradient G_l is less than 200 K/cm) lead to instabilities. A finite bandwidth of wavenumber for instability occurs for all the unstable modes.

In chapter 5, we address the problem of unstable crystal tip and sharp wedge formation observed in the recent reported experimental studies. We develop a combined Cellular Automaton-Finite difference model to simulate the evolution in crystal growth, liquid/solid interface instabilities, and sharp wedge formation in the HRG process. Specifically, the CA algorithm is incorporated with the thermal and solutal transport model, where both constitutional and curvature undercooling effects is considered. Different methods are applied to take care of the growth velocity and artificial anisotropy terms incorporated in the model. Case studies are performed for different cooling conditions.

In chapter 6, the experimental development of the silicon HRG process is discussed. We present the latest advances regarding the silicon system, melt trials with different crucible designs are presented, and potential process problems are identified regarding coating material, and seed attachment.

Chapter 2

The Horizontal Ribbon Growth Process

2.1 Introduction

In the HRG process, heat is removed through the top surface of a molten silicon pool; meanwhile, a thin silicon solid sheet is produced and extracted continuously, which eliminates the need for additional sawing. In addition, HRG extends the solidification interface since latent heat dissipation is perpendicular to the pulling direction, a characteristic which promotes the production speed by two orders of magnitude compared with the vertical ribbon growth techniques [2]. Since the silicon ribbon is resting on top of its melt, the HRG process also: (1) reduces the thermal and mechanical stresses resulting from material extraction compared with vertical ribbon growth processes, such as EFG process; and (2) reduces the material contamination from substrate and crucible compared with ribbon growth on substrate (RGS) process [46]. As a result, the HRG process has the potential to grow single-crystal wafers at a rate of 6.9mm/s, which results in an overall manufacturing rate of $93m^2$/day

[28]. In this chapter, we summarize the major theoretical and experimental work made in the HRG process development for the past 60 years, as well as the current technical difficulties encountered.

2.2 Literature review of the HRG process

In 1959, Shockley developed and patented the first HRG method [48], where a thin film of silicon is formed on top of molten substrate. Experimental feasibility of the HRG process was demonstrated by Bleil in 1968 [5, 4], who successfully produced ice and germanium ribbons using the HRG process. In his design, a heat sink removes heat from the process and facilitates solidification. The produced ribbon is pulled horizontally over the melt. Figure 2.1 demonstrates Bleil's process schematic. Ice and germanium ribbons are produced using the HRG process. In 1979, Kudo proposed a new HRG design with modifications and improvements [28]. The improvements in these works solved problems related to cooling, crystal growth and pulling [28]. With these improvements, Kudo demonstrated production rate of up to 4.1 mm/s for single-crystal silicon ribbon and up to 8.5mm/s for multi-crystalline ribbon, with a thickness of 200-400 μm, width of 10-30 mm, and ribbon length over 2m. Single crystal silicon ribbons were produced with dislocation densities up to 10^5 cm^{-2} with some sections dislocation free. A solar cell fabricated from the HRG ribbons was reported to have comparable conversion efficiency as CZ crystals. Figure 2.2 shows the schematic of Kudo's HRG process setup, where a gas cooling system is placed near the melt level. In particular, a large length to thickness ratio is used in Kudo's design.

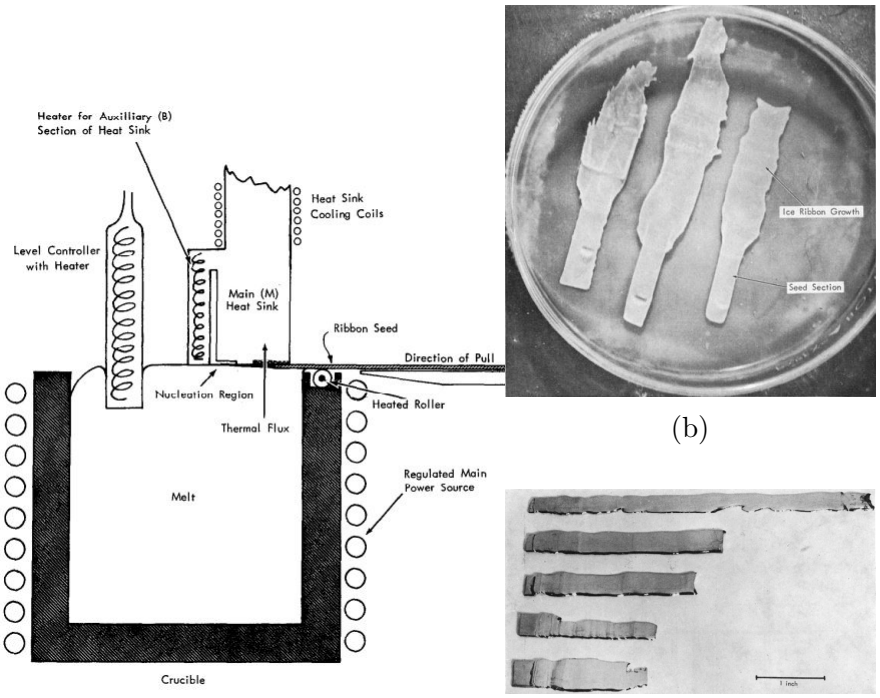

(a) (b) (c)

Figure 2.1: Bleil's HRG design and obtained wafer. (a) refers to the Schematic drawing of Bleil's HRG system (b),(c) refer to the ice and germanium ribbon produced. Graphics taken from Bleil [5]

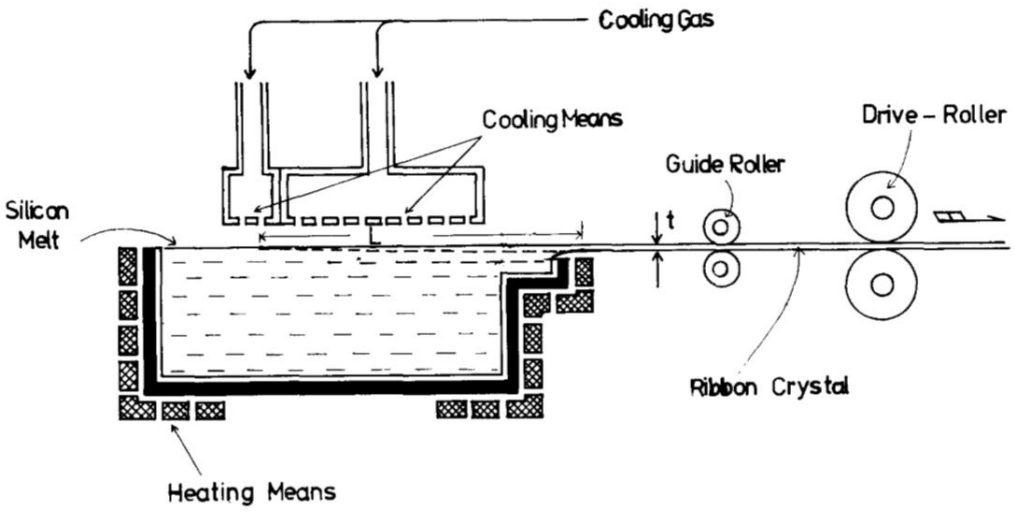

Figure 2.2: Schematic drawing of Kudo's HRG system. Graphic taken from Kudo [28].

The works of Bleil and Kudo brought attention to the problem of controllability of the HRG process, which was previously difficult to operate for

longer periods since it is sensitive to perturbations and variation in operating conditions.

Zoutendyk performed analytical studies to evaluate the effects of different cooling setups [59], where the effect of convection due to the extraction of wafer is evaluated. He proposed active cooling apparatus in addition to the passive radiative cooling to enhance the crystal growth in the HRG process. Zoutendyk also quantified the correlation between pulling velocity and the thickness of the ribbon [58]. This relationship has been verified in experimental studies using ice-water as a model in our research group [36].

More recently, Bleil and Daggolu et al. [14, 15, 16] developed a thermal-capillary model to investigate the interaction between fluid flow and heat transfer in the process. As shown in Figure 2.3, the model captures the vortex flow around the two free surfaces (the melt surface and the meniscus between the crucible and ribbon near the exit) induced by Marangoni effects and buoyancy, which is crucial for further investigation on the development of a stable wafer extraction apparatus. A sensitivity analysis is performed to investigate the problems of melt spill over and freezing originally proposed by Kudo. Due to the nonlinear behavior of HRG process, two wedge factors (the ratio between the thickness and the length of the wafer) are possible for one given pulling velocity. Thus, the process is inherently unstable since it exhibits multiplicity of steady states (see also Appendix F). In addition, Daggolu et al. [16] concluded that convection in the melt has an impact on the redistribution of solute in the system, and leading to inhomogeneous impurity concentration levels in the resulting ribbon.

Starting from 2008, Ydstie and Oliveros et al. [36, 37] worked on an experimental realization of the HRG process by designing a prototype water-ice HRG process. Oliveros and Ydstie developed a set of models to study the stability

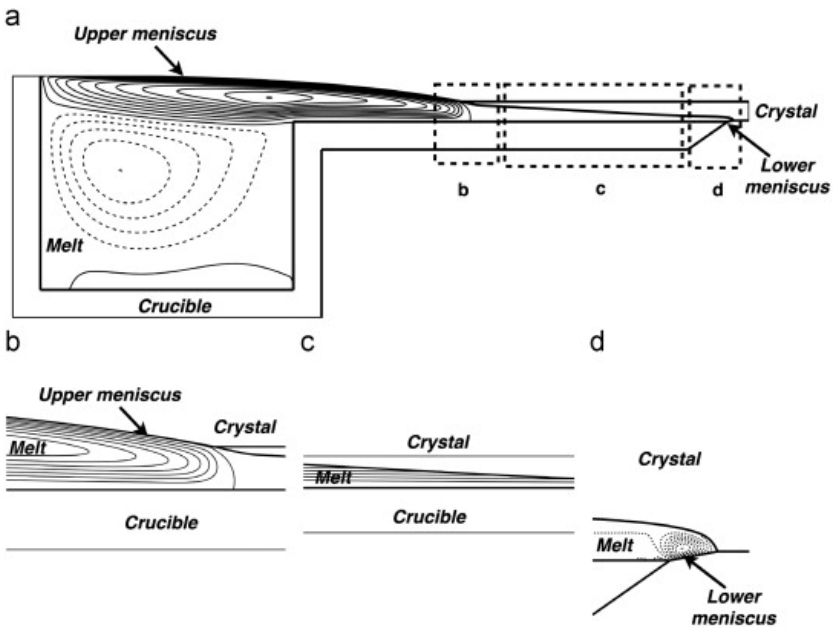

Figure 2.3: Stream function contours near the upper and lower meniscus observed by Dagglou.

of the HRG process and the crystallization dynamics. The effects of impurities on the interface were analyzed by incorporating Mullins-Sekerka analysis [36], which describes the thermal and solutal stable condition for solidification interface. Existence and stability conditions of the meniscus in the HRG process were studied by using variational theory and the first law of thermodynamics [37]. Figure 2.4 shows two cases that demonstrate feasible and prone to spill over meniscus operation conditions, respectively.

In 2009, BP Solar designed another HRG design, shown in Figure 2.5a. This system consists of a fused silica crucible, feed container, induction coil and a chimney [11]. Silicon chips are feed in from the feed container, which is surrounded by the top induction heating coil. Silicon melt flow slowly into the quartz crucible, and a level control apparatus is used to control the flow rate. The chimney is sitting on top of the crucible to adjust the thermal profile of the melting and growth region of the process. This machine is currently being used in CMU for experimental verification of the HRG process and it is

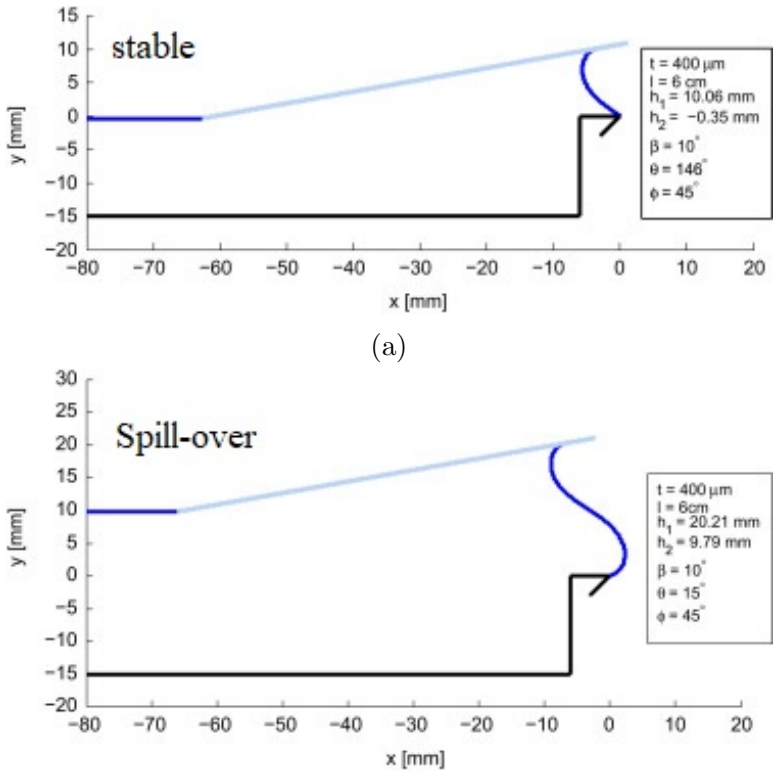

Figure 2.4: Two hydrostatically feasible operation conditions to produce a 6 cm long and 400 μm thick wafer observed by Oliveros et al. [37], (a) refers to stable operating conditions, (b)refers to the operating conditions that is prone to spill over.

described in detail in Chapter 6.

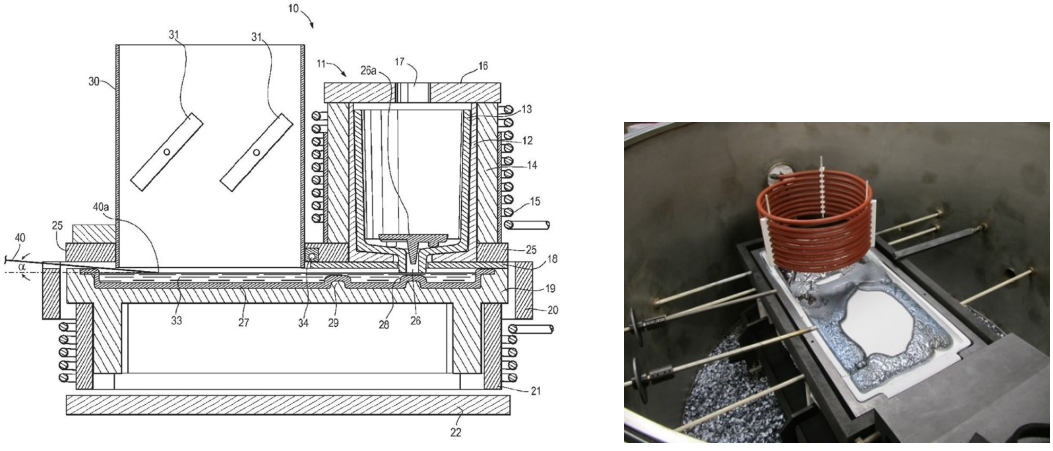

Figure 2.5: BP Solar HRG design and melt trial experiment.

In 2016, Helenbrook et al. [22] developed numerical models to capture the kinetic effects of crystal growth on the crystallization front. The experimental FSM design (Floating Silicon Method) was developed by at Applied Materials (formerly Varian Semiconductor Equipment Associates), where the setup is illustrated in Figure 2.6a. Figure 2.6b shows the produced single crystal silicon wafer (top view). Experimental and numerical results were compared for the leading edge position of the crystal front. The turning point that ensures stability with respect to the pulling velocity for a given heat removal rate for the proposed process was also identified from the numerical analysis, where maximum pull speed can be determined. In addition, a limit cycle theory with generalized rough/facet growth kinetics is proposed to understand the facet lines [26] observed in the experiments. In particular, the aforementioned authors concluded that the leading edge grows in a fashion that switches spontaneously between slow facet growth and fast roughened growth.

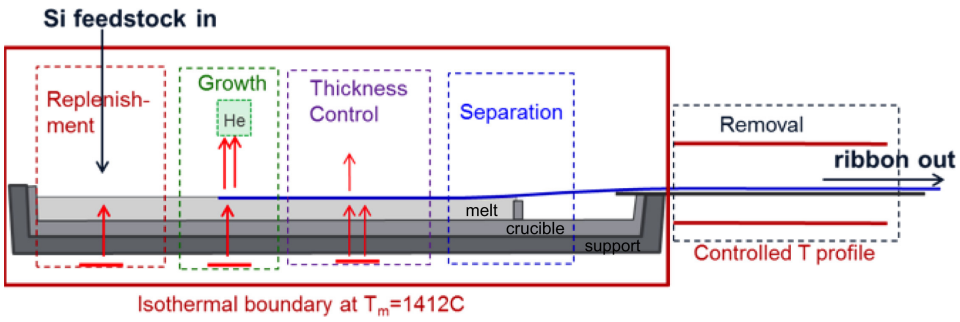

(a) Schematic of the Varian FSM Experimental Configuration.

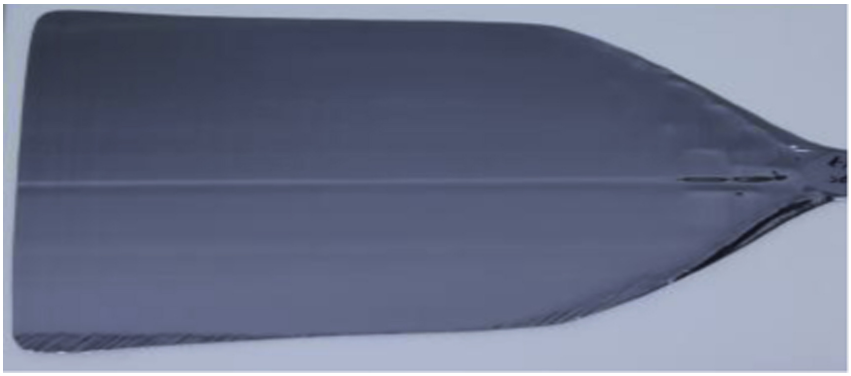

(b) Silicon Wafer produced from HRG process by Varian Semiconductor. Top view

2.3 Open Challenges in the HRG process

Theoretical understanding of the HRG process is limited, and the process itself has not been commercialized yet due to the difficulty of forming a stable mono-crystalline ribbon. Various system instabilities have been found in the pilot size experiments, including dendritic growth and variation of wafer thickness. The recent experimental results from Varian Semiconductor report sudden dendritic growth near the crystal front at relative high pulling velocity as initially observed by Kudo [25]. In 2011, researchers at Varian Semiconductor Equipment reported pulling a single crystal ribbon of 2 cm in width, 10 cm in length with a pulling velocity around 0.5 mm/s [25, 22]. One of the main technical challenges encountered in the reported HRG experiments is the instability at the wafer-melt interface, such as dendritic growth and wavy instability along growing process [28, 25]. The latter refers to wave shaped corrugation shown on non-smooth interface. Figure 2.7 shows the silicon ribbons produced by the HRG process, where (a) refers to the wavy instability along growing process, (b) and (c) show the dendritic growth problem encountered, while (d) shows the single crystal ribbon with a (1,1,1) facet.

The control of the HRG process is challenging since the system dynamics are highly nonlinear and coupled. Steady state gains of a linearized model vary considerably at different operating conditions and also shows the multiplicity reported by Daggolu et al. [15]. The rate of wafer removal, the cooling which ensures the crystal growth, and heating which helps to avoid solidification in undesired sections must be coordinated using feedback control to maintain desired stable thin wafer production. The implementation of advanced process control for the HRG, or for that matter any feedback control, has not been explored yet.

In the following chapters, we develop theoretical and mathematical ap-

(a) Silicon ribbon grown by Kudo shows wavy instability.

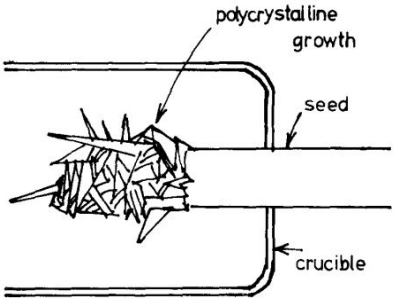

(b) Kudo's schematic illustration of dendritic growth.

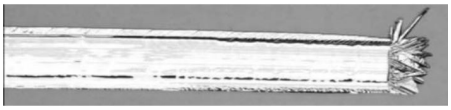

(c) Silicon ribbon grown by Varian Semiconductor shows dendritic growth.

(d) Single crystal ribbon grown by Varian Semiconductor.

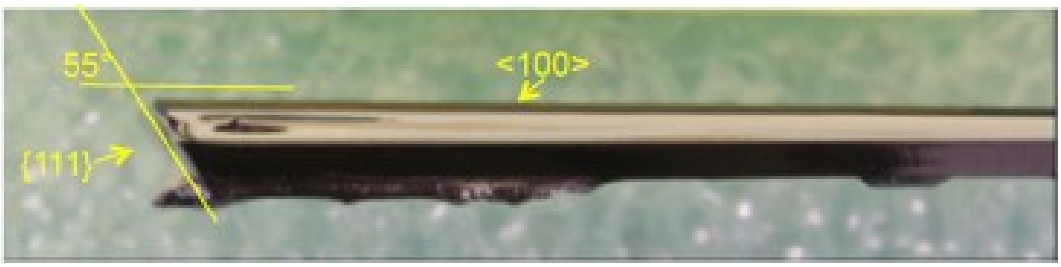

(e) Silicon ribbon grown by Varian shows sharp wedge, non-smooth interface.

Figure 2.7: Silicon Ribbon produced through the HRG process. (a) refers to the silicon ribbon grown by the HRG process from Kudo's experiments; (b),(c) refer to the dendritic growth problem encountered in the process; (d) refers to the single crystal ribbon that has (1,1,1) facet; (e) refers to ribbon obtained with a sharp 55° growth wedge

proaches to study three main challenges: (1) Development of the overall process mathematical model that provides quantitative representation of the heat

transfer, solidification, and flow patterns in the HRG process; (2) Evaluation of the effects of different driving forces in the process and proposing a range of stable operating conditions that can avoid potential corrugated wavy interface instabilities; (3) Development of mathematical model that can capture the formation of sharp wedges and unstable crystal front in the HRG process. From an experimental point of view, we present the latest advances on crucible design, seed attachment, and melting procedure, all of which are critical for the successful implementation of the silicon HRG process.

Chapter 3

Development of the Ice-Water HRG process

3.1 Introduction

In this chapter we propose to use an ice-water system to demonstrate the HRG concept experimentally. This idea was previously explored by Bleil [5, 4] as shown in Figure 2.1. Table. 3.1 shows that water has similar material properties with silicon that the solid phase density is smaller than that of the liquid phase. Thus, in an ice-water HRG prototype system, the ice wafer will float on top of water and can be extracted continuously. The cost for raw material is low and it is flexible for process design, modification, and improvement. Meanwhile, a mathematical model is built to allow quantitative representation of solidification phenomena in the ice-water system. A major difference between ice and silicon is the crystallinity. Ice is an amorphous material, whereas in the silicon HRG process, we aim to produce mono-crystalline silicon.

Table 3.1: Material Properties Comparison for water and silicon. Adapted from [15]

Property	Silicon	Water
Relative Density (liquid/solid)	1.11	1.09
Relative heat capacity	0.93	2.05
Kinematic Viscosity (10^{-3})	0.22	1.7
Relative thermal conductivity	3.23	0.26
Latent heat of fusion ($\frac{KJ}{kg}$)	1790	344

3.2 Ice-water HRG Experiment

Our prototype ice-water HRG system consists of a small main bath milled from a transparent solid block of plexiglass. The main bath is $29cm$ long, $19cm$ wide, and $1.2cm$ deep; and the sidewall has a thickness of $2.5 - 3cm$. The system is capable of producing ice wafers that are about $10cm$ wide. The cooling system is controlled by the flow rate of liquid nitrogen through a heat exchanger placed above the bath. A heating system is installed along the two sides of the bath to prevent freezing to the sides. The heat system is controlled by heating strips and monitored by thermocouples. The sheet pulling system is implemented by a conveyor belt and motor, as shown in Figure 3.1 (Side View) and 3.2 (Top View).

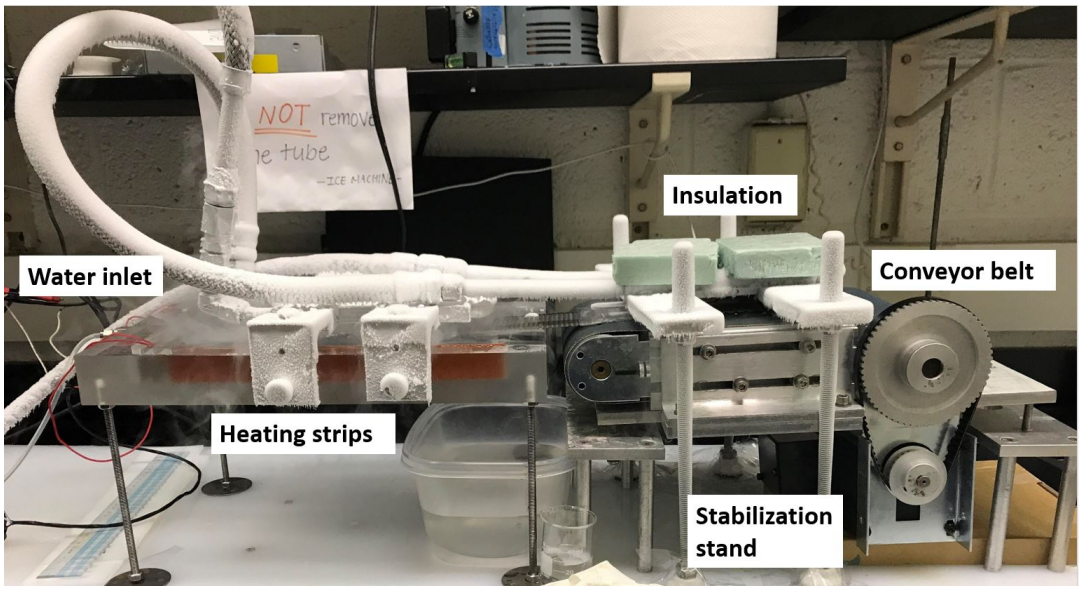

Figure 3.1: Ice Machine Side View.

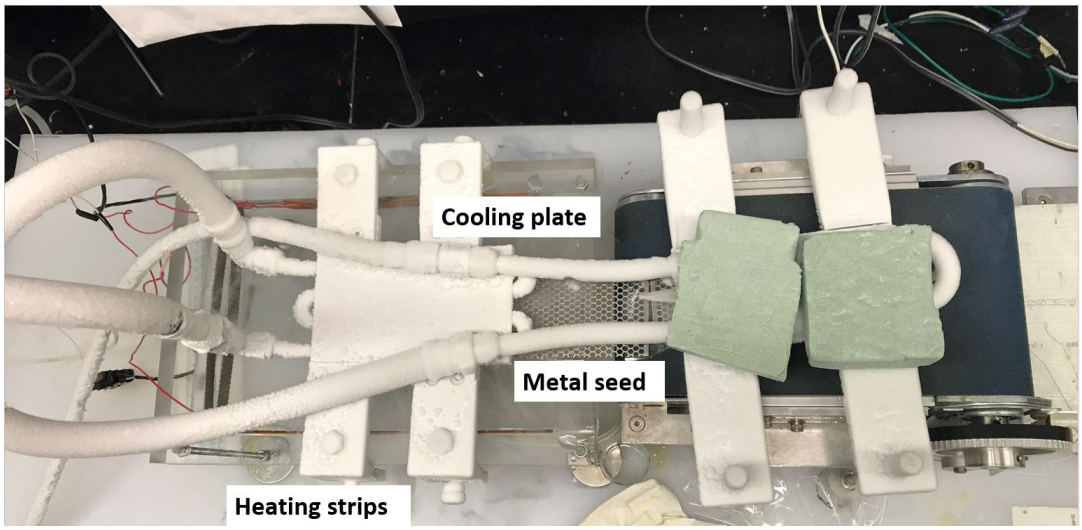

Figure 3.2: Ice Machine Top View.

A typical ice wafer experiment is conducted in the following fashion:

1. Water is pre-chilled by passing it through a pipe submerged in a bucket of ice and water.

2. Water is continuously fed in from water inlet and passes through two metal mesh flow breakers to avoid disturbance introduced from high inlet flow rate.

3. Liquid nitrogen is fed through the cooling plate from flexible tubing. The cooling of the system is controlled by the flow rate of liquid nitrogen as well as the distance between the cooling plate and the top surface of the bath.

4. A flat metal mesh seed (approximately $20cm$ long, $5cm$ wide, and $0.25cm$ thick) is taped to the conveyor belt and used to initiate the crystal growth.

5. The conveyor belt and motor are used to extract the produced ice wafer. Specifically, we adjust the height of conveyor belt to alter the pulling angle ($3°$ is used as this is the closest angle we can achieve to the suggested value of Oliveros et al. [37] to ensure stability of the meniscus between produced wafer and the edge of crucible).

6. As the extraction proceeds and the seed reaches the end of conveyor belt, the metal seed is separated from the produced ice wafer to ensure continuous wafer growth.

7. An additional cooling plate is installed to cover the conveyor belt to maintain the temperature for the produced ice wafer and avoid direct melting.

8. The thickness of wafer is measured at the exit, while corresponding extraction velocity is recored.

We found the extraction process to be easier if a positive pulling angle is applied. The extraction velocity plays an important role for the ice HRG experiment: fast pulling speed results in a thinner wafer but may lead to unstable crystal growth or ribbon breakage; slow pulling speed results in a thicker wafer but excessive ice may start to form near the edge and end of

the bath, which may lead to complete freeze over. In addition, it is difficult to decide the appropriate starting point for the extraction process: from the moment the seed is placed into the melt, the ice wafer starts to grow and expand. Some waiting time is needed for the ice to grow. This time needs to be controlled to ensure stable pulling and avoid breakage. Figure 3.3 shows an ice wafer produced using a HRG system.

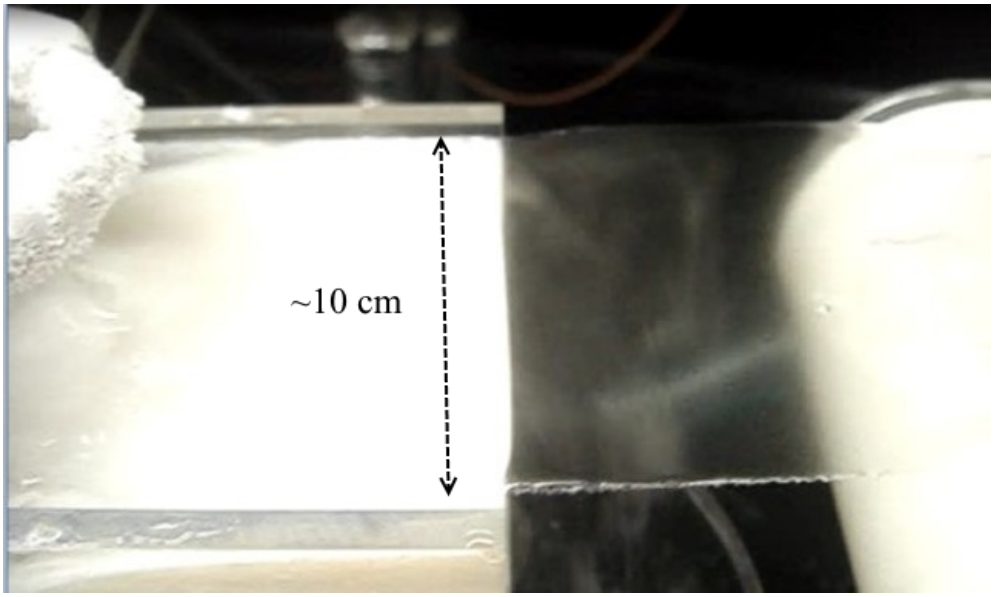

Figure 3.3: Ice Wafer Produced using a HRG system.

The ice-water system is utilized to verify multiple research ideas. Firstly, the correlation between thickness of the wafer and pulling velocity has been an essential factor for the HRG process: thickness is an important characteristic for direct ribbon process since further wafering and polishing should be avoided or minimized (typical industry standard is around $200\mu m$); pulling velocity is essentially the production speed, and directly affect the overall throughput of the HRG process. In particular, ice wafers produced utilizing the current design align in the reliable region for both thickness and width. The meniscus stability condition is another important factor that has to be determined for stable operation. Earlier theoretical analysis has been performed by Oliveros

et al. [37] and the ice-water system was used to perform proof-of-concept experiments, as shown in Figure 3.4. Design factors such as pulling angle and relative level are verified. This also guides us in further extraction apparatus design for the silicon system.

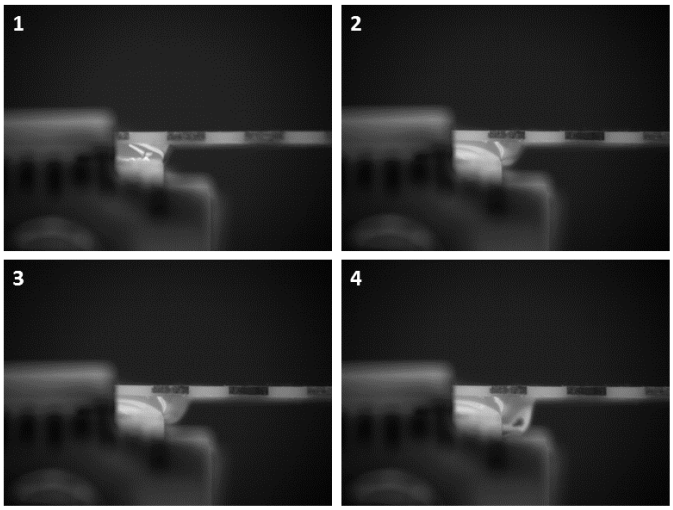

Figure 3.4: Proof-of-concept experiments demonstrating the problem of meniscus spill over by the ice-water system. Graphics taken from [38]

3.3 Solidification in the HRG process

We describe the solidification problem in the HRG process by a two phase system with a sharp interface. The heat equation for the solid region can be written as:

$$\frac{\partial}{\partial x}[k_s \frac{\partial T}{\partial x}] + \frac{\partial}{\partial y}[k_s \frac{\partial T}{\partial y}] - \rho C_p u \frac{\partial T}{\partial x} = \rho C_p \frac{\partial T}{\partial \tau}. \tag{3.1}$$

The velocity term can be neglected at low pulling velocity (lower than 355 mm/min in this case, and the detail validation is included in the appendix section). And the RHS of the heat equation is neglected as we consider steady state analysis. Then we arrive at a Laplace equation. Based on the Zoutendyk Theory, a triangular solid wedge shape is assumed as shown in Figure 3.5 and linear solution of previously defined heat equation results at the following

temperature gradient at the interface:

$$G_x = \left|\frac{\partial T}{\partial x}\right| = \frac{\Delta T(l,0)}{l}, \tag{3.2}$$

$$G_y = \left|\frac{\partial T}{\partial y}\right| = \frac{\Delta T(l,0)}{t}. \tag{3.3}$$

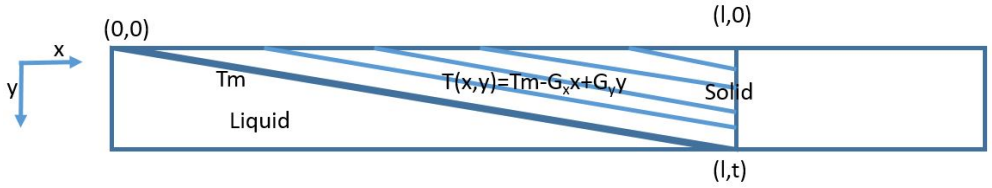

Figure 3.5: Schematic drawing of Ribbon illustrating triangular shape wedge with linear solid liquid interface.

The energy balance at the interface can described as follows:

$$\rho_s L_s v_y(x) + k_l G_l = k_s G_s. \tag{3.4}$$

We assume a linear temperature solution,

$$T(x,y) = T_m - G_x x + G_y y. \tag{3.5}$$

Heat loss through convection at the interface can be written as:

$$k_s G_y = h_{air}(T(l,0) - T_{air}), \tag{3.6}$$

where G_s can be obtained by $G_s = G_y(tan^2\theta{+}1)^{1/2}$ and $T(l,0) = T_m{-}\Delta T(l,0)$. θ is determined by the shape of the wedge. From equation (3.4) we then arrive at:

$$v_y(x) = \frac{\partial y}{\partial \tau} = \frac{k_s G_s - k_l G_l}{\rho_l L_s} = \gamma. \tag{3.7}$$

We can integrate along the y direction: $\int_0^t dy = \gamma \int_0^{l/v_x} d\tau$. The correlation

between pulling velocity and thickness of the wafer can be written as:

$$v_x = \gamma \frac{l}{t} = \frac{(k_s G_s - k_l G_l) l}{\rho_l L_s t}. \tag{3.8}$$

This model will be compared with the ice-water system described below.

3.4 Mathematical model of the HRG process

In order to better understand the interactions of the proposed system, a mathematical model describing heat transfer, phase change, and fluid flow is developed. We assume the interactions of ice-water HRG system can be represented by two dimensions, as depicted by the following Figure 3.6, where the cross section of water bath is $20cm$ long and $2cm$ deep. Convective cooling is used to remove the heat, water is feed in from the inlet continuously and wafer is being extracted from the outlet.

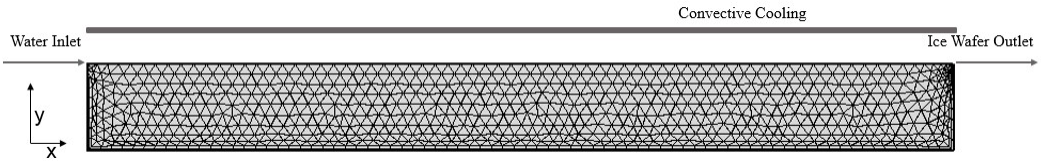

Figure 3.6: Ice Wafer Process Geomoetry and finite-element mesh used in calculation.

3.4.1 Governing Equations

The energy conservation equation is applied for both liquid and solid phases to model the temperature field $T(x, y)$ through the system, where convection terms in the liquid and solid domain account for fluid flow and ribbon motion, respectively. This gives the energy balance:

$$\frac{\partial T}{\partial t} + \mathbf{u} \cdot \nabla T = \alpha_i \nabla^2 T, \quad i = l, s \tag{3.9}$$

Subscript i represents the phase, with l for the liquid and s for the solid. The thermal diffusivity, $\alpha_i = k_i/\rho_i Cp_i$ is calculated for each phase, where k_i represents the thermal conductivity, ρ_i represents the density, and Cp_i represents the heat capacity. t refers to the time, and $\nabla = (\frac{\partial}{\partial\ x})\mathbf{e}_x + (\frac{\partial}{\partial\ y})\mathbf{e}_y$. The continuity equation is given by

$$\nabla \cdot \mathbf{u} = 0, \tag{3.10}$$

The Navier-Stokes Equation for fluid flow is described by

$$\rho\frac{\partial \mathbf{u}}{\partial t} + \rho(\mathbf{u}\cdot\nabla)\mathbf{u} = \nabla\cdot[-p\nabla I + \mu(\nabla\mathbf{u} + (\nabla\mathbf{u})^T)] + \mathbf{S}. \tag{3.11}$$

The velocity field $\mathbf{u}(x, y)$ is calculated by the Navier-Stokes equation and the Continuity equation, to satisfy the momentum and mass balance, respectively. Here, Newtonian, incompressible and laminar fluid flow is assumed. μ is the dynamic viscosity of silicon melt and crystal, $\mathbf{I}$ the identity tensor, $\mathbf{S}$ the source term to be discussed below.

3.4.2 Approximation of Solid Phase

In this study one set of momentum equation is solved by assigning the true value to the viscosity in the fluid and a very large value ($\sim 1000 Pa \cdot s$) to the viscosity in the solid region. In this manner, both liquid and solid phase are calculated within one set of Navier-Stokes equations. This approximation ensures low computational workload [41, 39].

3.4.3 Mushy Zone Theory

Models representing physical systems that involve liquid-solid phase change and convection problems are computationally difficult to solve. Such a problem belongs to the class of moving boundary problems. They are usually modeled by nonlinear systems of partial differential equations describing the momentum, mass and energy balance. The determination of a sharp moving interface is also a challenging task. The phase change of metal and metal-alloys typically happens in a narrow range of temperature with complex crystallization kinetics, and these types of problems are often referred as mushy region problem. The Darcy approach is used to simulate motion in the mushy region [51]. Specifically, the entire domain is treated as porous media, where porosity, α, can be treated as liquid phase composition, and calculated as follows. ΔT is the half width of the mushy region, and set to $0.1K$ in this study.

$$\alpha = \begin{pmatrix} 0 & (T < T_m - \Delta T) \\ \frac{T - T_m + \Delta T}{2\Delta T} & (T_m - \Delta T \leq T \leq T_m + \Delta T) \\ 1 & (T > T_m + \Delta T) \end{pmatrix}. \tag{3.12}$$

$$S_x = -A(u_x - u_0) \quad S_y = -Au_y. \tag{3.13}$$

where A increases from 0 to a very large number ($\sim 10^8$) as the liquid phase composition decreases from 1 to 0. As local solidification proceeds ($\alpha \sim 0$), the source dominates in the momentum equations and the superficial velocity is forced to be constant in the solid domain and equal to the pulling velocity where $u_x = u_0$. In this study, the form of A is taken from the Darcy law [7] so that:

$$A = -C\frac{(1-\alpha)^2}{\alpha^3 + q} \tag{3.14}$$

where C is a very large number. In this study we use $C = 10^5$ and the constant q is set to be 0.001 to avoid the division by zero (sensitivity analysis is performed to ensure the accuracy).

$$S_b = \rho_l[1 + \beta(T_m - T)]\mathbf{g}. \tag{3.15}$$

The term S_b, in the y direction momentum balance equation, is the buoyancy term induced by natural convection. The Boussinesq approximation is used to consider the temperature dependent density. Here, β is the thermal expansion coefficient and T_m is the melting point of ice.

3.4.4 Discontinuity in physical properties

The continuity of a physical property is an important factor in finite element methods. Most of the material properties in the phase change problems are discontinuous, thus, Heaviside function approximation is used to smooth the discontinuities for density, viscosity, and thermal conductivity. In particular, the latent heat of fusion is taken into account by using an additional Gauss distribution function, as represented in the following equation.

$$Cp = Cp_l H(T - T_m) + Cp_s H(T_m - T) + D(T)L, \tag{3.16}$$

where $H(T - T_m)$ and $H(T_m - T)$ represents for Heaviside step function, and $D(T)$ is the Gauss distribution function.

$$D(T) = \frac{1}{\sqrt{2\pi\Delta T^2}} exp[-\frac{(T - T_m)^2}{\Delta T^2}]. \tag{3.17}$$

3.4.5 Flow and thermal boundary conditions

Mass conservation of the system is enforced by the continuity equation together with the boundary conditions that specify the inlet and outlet flow rate conditions. Specifically, the outlet condition is specified by the pulling rate while the inlet condition can be defined by either flow rate or specified pressure ($1atm$). As for the inner crucible walls, we assume zero value for both normal and tangential velocity terms (or $\mathbf{u} = 0$). No-slip condition is used for the bottom of the crucible. For the solidification interface, we applied Mushy Zone theory and smoothed out discontinuous physical parameters as illustrated in the previous sections. Thus, no additional interface boundary condition need to be specified. However, it should be noted that appropriate velocity conditions should be enforced for a typical solidification problem, such as tangential velocity term raised from mass conservation when solidification occurs. For the ice-water system, a cooling plate is used for the experiment and we assume the temperature can be estimated. A convective cooling condition is used for the simulation and can be described as follows:

$$k_s \mathbf{n} \cdot \nabla T \mid_{interface} = h(T \mid_{interface} - T_{ambient}). \tag{3.18}$$

where h represents for the heat transfer coefficient estimated for the cooling condition described in the appendix section, $T_{ambient}$ is the ambient temperature with which the surface transfer heat with. We assume a constant temperature for the inner wall and bottom of the crucible to represent the heating design used in the experiments as we use heating strips and temperature con-

troller to maintain constant temperature.

3.4.6 Numerical Solution

The conservation equations are formulated as system of PDE equations and simulated in COMSOL, which is a finite-element simulation package. In this approach, the temperature, velocity, and pressure are approximated by low order polynomials defined over a mesh of elements. Specifically, velocity and temperature profiles are approximated by linear combinations of Lagrangian based quadratic functions. The pressure field is approximated using a linear functions basis Lagrangian. The governing PDEs are converted to their weak forms. This is especially critical for NS equations when some physical properties are not perfectly smooth in all the domain elements, such as viscosity. A triangular mesh is generated in the entire domain according to the geometry and specific boundary conditions. The complete mesh used in this work consisted of $\sim$ 1000 domain elements, $\sim$ 200 boundary elements, which resulted in $\sim$ 5000 degrees of freedom. One example is shown in Figure 3.6.

3.5 COMSOL Simulation and Experimental Results

3.5.1 Steady State Simulation

A steady state computation was performed using the parameters and physical properties stated in the Table 3.2, and the system temperature and velocity profile are shown in Figure 3.7 and 3.8, respectively.

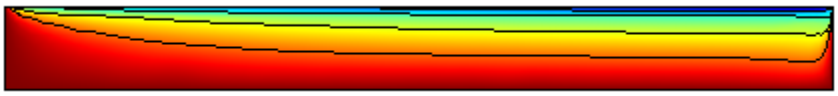

Figure 3.7: Temperature Profile and Isotherms of the Proposed Ice Wafer Process. (Isotherms are plotted with spacing of 0.2K, with an overall temperature difference of 1K)

Figure 3.8: Velocity Profile and Streamlines of the Proposed Ice Wafer Process.

Table 3.2: Material Properties and Parameters used in the model. Adapted from [32]

Parameter	Symbol	Value
Melting temperature	T_m	$273.15K$
Thermal Conductivity of water	K_l	$0.55\frac{W}{mK}$
Thermal Conductivity of ice	K_s	$2.22\frac{W}{mK}$
Density of water	ρ_l	$999\frac{kg}{m^3}$
Density of ice	ρ_s	$916\frac{kg}{m^3}$
Latent heat of fusion	L	$344\frac{KJ}{kg}$
Heat capacity of water	Cp_l	$4179\frac{J}{kg \cdot K}$
Heat capacity of ice	Cp_s	$2050\frac{J}{kg \cdot K}$
Dynamic viscosity of water	μ	$1.78mPa \cdot s$

Simulation Validation

One of the objectives of the HRG process is to achieve faster production rate compared with ingot based crystallization and vertical ribbon growth techniques. Here, the behavior of the water-ice model is examined for changes in the pulling rate and cooling plate temperature while keeping all the other

parameters constant. Higher pulling speed results to less latent heat of dissipation per unit length at the interface, reducing the thickness of the ribbon; while lower cooling plate temperature enhance the heat removal rate, leading to a thicker wafer. The following figures 3.9 show the results of the sensitivity analysis for different pulling rate and cooling condition. The figure 3.10 shows the comparison of COMSOL simulation, Zoutendyk theory based model, and experimental results. The simulation results show that as the pulling speed increases from $50(mm/min)$] to $148(mm/min)$, the ribbon thickness decreases from $1.14mm$ to $0.17mm$. The simulation results are qualitatively in agreement with the experimental results, and are especially close for the higher pulling rates where the ice wafer has the desired thickness of $150 - 200\mu m$.

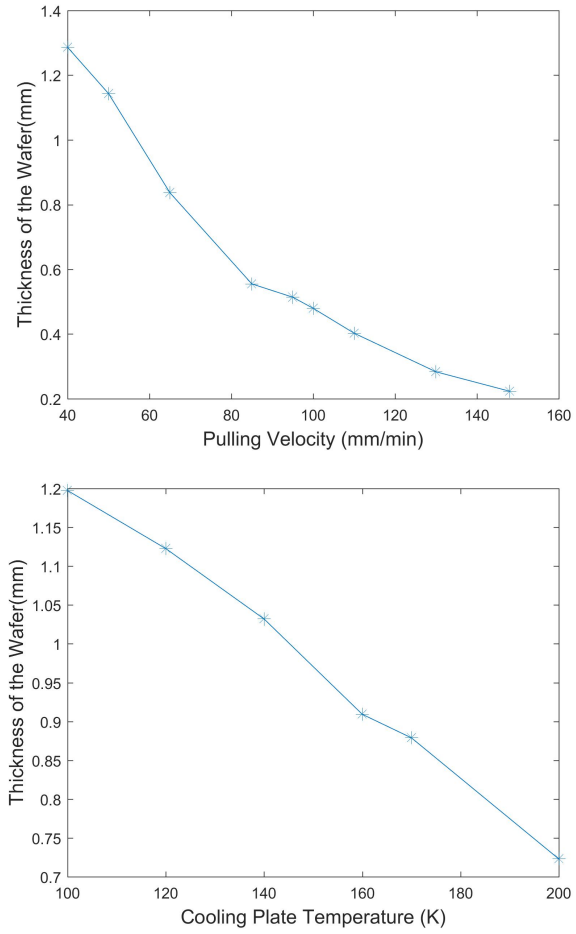

Figure 3.9: Steady State simulation result for the Ice wafer process.

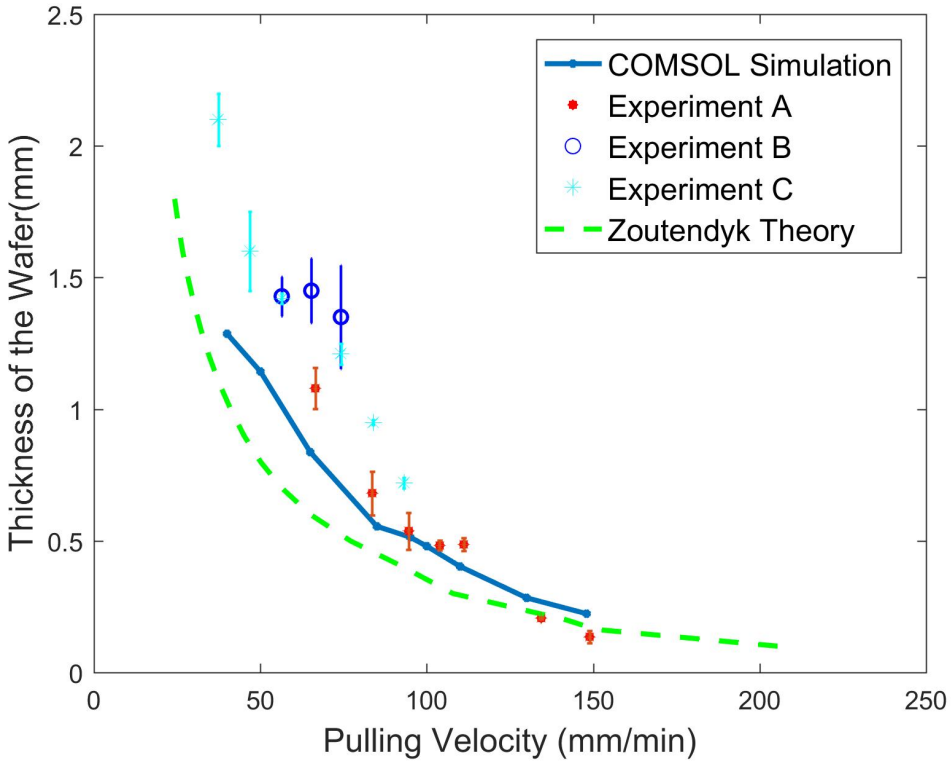

Figure 3.10: Correlation between Pulling Velocity and Thickness of the wafer for the Ice Wafer Process.

3.6 Conclusions and contributions

We presented computational modeling, theoretical analysis, and experimental updates on the development of ice-water system as a prototype of silicon HRG process. A 2D COMSOL model is developed to represent the heat transfer, fluid flow and phase change behavior in the ice-water HRG process. The simulation models reveals that water solidifies on the top of water bath as temperature drops below the melting point. As produced ice wafer is extracted continuously through the outlet, a wedge shaped thin wafer is being generated. Steady state simulation is performed using production speed of $50 - 150 mm/min$, while thickness of resulting wafer is measured. In addition, we performed theoretical analysis based on Zoutendyk theory and the

correlation between thickness and pulling velocity is obtained for the convective cooling case. The experimental progress been made for the HRG process development is discussed. The water-ice HRG system is utilized to produce ice wafer and we have achieved stable, reliable, and reproducible ice wafer experiments using the current design. Experimental results, computational simulation and theoretical results are compared. The successful operation of an ice-water system wafer production system proved the feasibility of the propsed approach and it showcased the potential of utilizing the HRG process for the production of silicon wafers as well. Further studies need to focus on the stability and crystallization properties of silicon as well as experimental verification of the silicon system.

Chapter 4

Stability Analysis of the crystal interface in the context of the HRG process

4.1 Introduction

The lifetime and efficiency of a solar panel relies on the quality of the silicon wafers, which depends crucially on the growth condition of crystal, such as impurity level and the thermal gradient. Although the impurity level in the feedstock of the wafer growth process is quite low (typically less than $0.1ppm$), the growth process itself may introduce additional impurity into the system from the equipment and process [37]. Another problem is that the impurity concentration may increase significantly close to the wafer as impurities are pushed into the liquid during solidification.

In the HRG process, many impurities come into play among them, iron, phosphorus, boron, aluminum, carbon and oxygen. Some typical segregation coefficients are shown in Table 4.1. We have chosen to start the study using

Table 4.1: Segregation Coefficient of Impurities in silicon. Adapted from [8]

Element	Al	Fe	C	P	B	O
k_{seg}	$2.83 \cdot 10^{-3}$	$8 \cdot 10^{-6}$	$6 \cdot 10^{-2}$	0.35	0.786	0.25

Al as a modeled impurity. The segregation coefficient of Al is similar to that of C, which will be abundant in our experiments. The use of Al also provides a foundation for the shift of feedstock material from high purity metallurgical silicon to Kaolin, an Si-Al-O mineral which is abundantly available. Our current HRG experiments uses a graphite crucible to contain the melt. This may introduce carbon into the silicon during the high temperature melting. Oxygen may be introduced through the imperfect vacuum condition and can be potentially problematic.

The thermal gradient in the liquid and solid phase determines the interface stability and thermal stress/defect of the produced wafer, respectively. Theoretical studies have been developed for the instabilities during unidirectional solidification [13, 12].

In 1964, Mullins and Sekerka developed the foundation for the thermal and solutal conditions to ensure the stable crystallization front under an arbitrary small amplitude sinusoidal perturbation to the interface [34]. In this theory, is is assumed that the system is at steady state with constant growth velocity. An analytical solution for the stability conditions at a given perturbation is determined by:

$$\frac{\dot{\delta}}{\delta} = \frac{V\omega\left\{-2T_M\Gamma\omega^2\left[\omega^* - \left(\frac{V}{D_l}\right)p\right] - (G'+G)\left[\omega^* - \left(\frac{V}{D_l}\right)p\right]\right\}}{(G'-G)\left[\omega^* - (V/D)p\right] + 2\omega m G_c} + \frac{2mG_c\left[\omega^* - \left(\frac{V}{D_l}\right)\right]}{(G'-G)\left[\omega^* - (V/D)p\right] + 2\omega m G_c}. \tag{4.1}$$

Here δ is the perturbation, V the constant growth velocity, ω the angular frequency of the perturbation, T_M the melting temperature, Γ the capillary

constant, D_l the diffusion coefficient, $G^{''}$ and G temperature gradients in the solid and liquid phase, G_c the concentration gradient, m the liquidus slope. A stable interface can be guaranteed if $\frac{\dot{\delta}}{\delta}$ is always less than 0 for any given perturbation.

Previous studies have been performed by Oliveros Patiño [38] to investigate the stability of HRG process via both classical M-S criteria and when transient effect is considered.

However, the flow pattern in the melt during the crystallization also plays an important role on the impurity distribution, which alters the micro-structure and macro material property of the grown crystal. This flow pattern can be induced by the rotation of the crucible or crystal, withdrawal of the material, density change during crystallization, etc.

Coriell and Sekerka performed extensive studies in the coupled convective and morphological instabilities [13, 12]. For the HRG process, the continuous extraction of produced wafer generates a shear flow near the crystallization interface, which links the production speed directly with the stability of the proposed process. We want to investigate this problem here.

The work is motivated by the Mullin-Sekerka stability analysis. We perform a linear stability analysis of the crystallization interface of the Horizontal Ribbon Growth (HRG) process. The conditions for the onset of stability are investigated numerically on the basis of convection-diffusion equations for the thermal and solutal fields coupled to the Navier-Stokes equation describing the flow field in the molten pool near the interface. The interface stability conditions of the system under different operating conditions are quantified.

4.2 Mathematical model of the HRG process

In order to perform a stability analysis of the crystallization interface, we first develop the thermal, solutal, and fluid flow model, which captures the phase change behavior. Figure 4.1 shows the conceptual design of the HRG process. Different cooling and heating apparatuses are used to control the shape and production rate of the thin wafer. Additional heaters and coolers are used to avoid the bridging or spill over to the crucible. In a typical experiment, one large graphite supporting crucible is directly sitting on top of the heaters and another smaller crucible which has a length of 20-40 cm is used to hold the silicon melt. Here, we are interested in the crystallization interface of the region where a stable and initially flat interface has been developed. We also assume that the flow and thermal patterns in this region are independent from the material replenishment and extraction, and thus are not affected by the inlet and outflow conditions. Newtonian and incompressible fluid is assumed in this study.

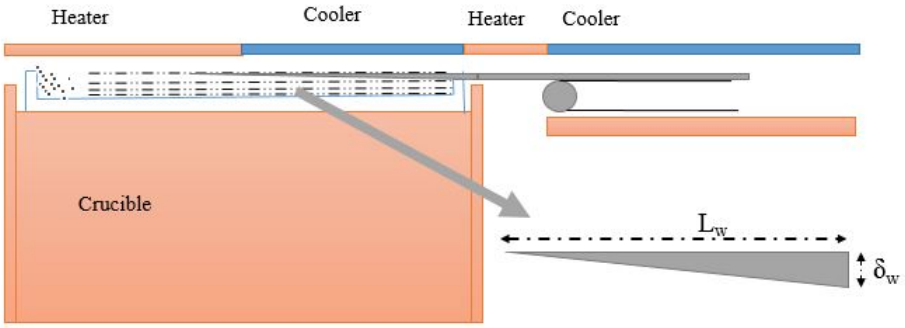

Figure 4.1: The Schematic Sketch for the HRG process.

Unidirectional vertical solidification at a constant velocity $\mathbf{V}$ within a binary silicon-alluminum melt is considered. The density variation of silicon melt is small in the experimental temperature range of interest [6]; thus, we make the assumption that density varies linearly with the concentration of

impurity and the temperature of the melt. In the frame of reference moving with velocity $\mathbf{V} = (0, -V)$ and applying the Boussinesq approximation for the liquid density, one arrives the following set of differential equations governs the fluid velocity $\mathbf{u}$, temperature T, and concentration C of the Aluminum (Al) impurity.

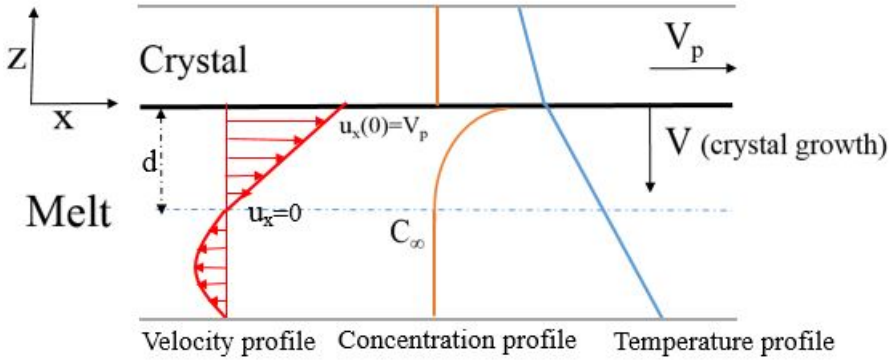

Figure 4.2: Typical velocity, concentration, and temperature fields near the HRG interface.

$$\nabla \cdot \mathbf{u} = 0, \tag{4.2}$$

$$\frac{\partial \mathbf{u}}{\partial t} + \mathbf{u}\cdot\nabla\mathbf{u} - \mathbf{V}\cdot\nabla\mathbf{u} = -(1/\rho_0)\nabla p + \nu\nabla^2\mathbf{u} - \mathbf{g}[1 - a_1(T-\tilde{T}) - a_2(C-\tilde{C})], \tag{4.3}$$

$$\frac{\partial T_l}{\partial t} + \mathbf{u}\cdot\nabla T_l - \mathbf{V}\cdot\nabla T_l = \alpha_l \nabla^2 T_l, \tag{4.4}$$

$$\frac{\partial C}{\partial t} + \mathbf{u}\cdot\nabla C - \mathbf{V}\cdot\nabla C = D\nabla^2 C, \tag{4.5}$$

$$\frac{\partial T_s}{\partial t} - \mathbf{V}\cdot\nabla T_s = \alpha_s \nabla^2 T_s, \tag{4.6}$$

where ν is kinematic viscosity, ρ_0, $\tilde{T}$ and $\tilde{C}$ are, respectively, the mean density, mean temperature of liquid, and mean concentration of impurity. a_1 and a_2 are thermal and solutal expansion coefficients, respectively, α_s and α_l are thermal diffusivity of the solid and liquid phase. D is the diffusion coefficient of the

impurity in the silicon melt. We assume that horizontal temperature gradient in the wafer is negligible, hence the advection term, $V_p dT/dx$, in the solid phase has been eliminated from Eqn. (4.6) and the ensuing stability analysis. The crystal growth velocity is defined as $\mathbf{V} = \mathbf{V}_p/W$, where $\mathbf{V}_p$ is the pulling velocity and $\mathbf{V}_p = (V_p, 0)$. Here, W is the wedge factor and defined as L_w/δ_w based on the theory of Zoutendyk (where subscript w stands for wafer) [58]. Here we assume that the wafer has a triangular shape, where the angle of solidification wedge is small and can be defined by the ratio of solidification velocity and the rate of wafer removal. This provides us an approximation of vertical crystal growth velocity without consideration of the crystallization kinetics thereof. For the impurity in the system, the conservation of mass at the crystallization interface leads to the following boundary condition [12]:

$$\mathbf{V}(k_{seg} - 1)C_{lI} = (\frac{\rho_l}{\rho_s}\nabla C_l)\mathbf{n}, \tag{4.7}$$

where k_{seg} is the segregation coefficient; C_{lI} represents for the impurity concentration in the liquid phase at the interface; $\mathbf{n}$ is the unit normal to the interface pointing towards the direction of crystal. Impurity is being rejected at the interface since $k_{seg} < 1$. Other inter-facial boundary conditions are the kinematic condition adjusted to account for the velocity change accompanying phase change, the Stefan condition representing energy conservation, the constant freezing temperature condition, and the Gibbs-Thomson condition, which are respectively,

$$\mathbf{V} \cdot \mathbf{n}(\rho_l - \rho_s) = (\mathbf{u} \cdot \mathbf{n})\rho_l, \tag{4.8}$$

$$\mathbf{V} \cdot \mathbf{n}L_v = (k_s \nabla T_s - k_l \nabla T_l)\mathbf{n}, \tag{4.9}$$

$$T_{sI} = T_{lI}, \tag{4.10}$$

$$T_{lI} = T_m + mC_{lI} - T_m \Gamma K, \tag{4.11}$$

where L_v is the latent heat of fusion, subscript I denotes for the quantity evaluated at the interface, k_s and k_l are thermal conductivities of solid and liquid. T_m is the melting point of the pure substance, m is the slope of the liquidus line, Γ is the capillary constant, and K is the interface curvature.

4.3 Non-dimensionalization and base state solution

The governing equations and the boundary conditions are normalized to obtain a nondimensional system. As shown in Figure 4.2, laminar flow is induced by the motion of the solid ribbon underneath the crystallization interface. The thickness d of this near surface flow is defined as the characteristic length[1], and the velocity of wafer movement (V_p) is defined as the characteristic velocity in this study. The fluid velocity ranges from $u_x(z = 0) = V_p$ at the crystallization interface to $u_x(z = d) = 0$ at the edge of the near surface flow. A Poiseuille-type back flow is expected due to the mass balance, leading to zero net volumetric flow as expected. However, in this study, we do not consider the back flow due to its limited effect on the linear stability of the interface. The temperature difference of the solid and liquid phase is defined as $G_s d = T_i - T_h$ and $G_l d = T_b - T_i$, respectively. The subscripts i, h, b refer to the interface, top surface, and bottom surface, accordingly; G_s and G_l refer to the unperturbed temperature gradient of solid and liquid phase, respectively. From Eqn. (4.9), the value of G_s can be determined: $G_s = (VL_v + k_l G_l)/k_s$.

[1] we assume d=1cm and the melt level in a typical experiment is less than 3 cm

The concentration difference is defined as $G_c d = C_i - C_\infty$, with C_i being the interface concentration and G_c being the overall concentration gradient. Thus, we can nondimensionalize previously defined system with the following units: velocity in units of V_p, time in V_p/d, length in d, liquid and solid phase temperature in $G_l d$ and $G_s d$, respectively, and C in $G_c d$. Here we assume a two-dimensional base state with a velocity profile:

$$\mathbf{u}_0 = (u_{x0}, -\epsilon V) \tag{4.12}$$

where u_{x0} represents the Couette flow driven by the pulling of the wafer, $u_{x0} = V_p(Z+1)$ [2], and $\epsilon = (\rho_s/\rho_l) - 1$ accounts for the relative velocity for the liquid phase.

The following base-state temperature and concentration fields are found from Eqn. (4.4)-(4.6) along with the boundary condition defined in Eqn. (4.7).

$$T_{l0} = c_1 e^{-V^* Pe_l Z} + T_{lI} - c_1, \tag{4.13}$$

$$C_{l0} = \frac{C_\infty}{k_{seg}} c_2 e^{-V^* Pe_l Sc/Pr Z} + \frac{C_\infty}{k_{seg}}(1 - c_2), \tag{4.14}$$

$$T_{s0} = c_3 e^{-V Pe_l \alpha_l/\alpha_s Z} + T_{sI} - c_3, \tag{4.15}$$

where $V^* = (\rho_s/\rho_l)V$, G_l and G_s are unperturbed temperature gradient of liquid and solid phase at the interface, respectively; C_∞ is the solute concentration far from the interface. c_1, c_2 and c_3 are constants that can be further determined by the interface boundary condition, where $c_1 = \frac{G_l d}{e^{V^* Pe_l} - 1}$, $c_2 = \frac{k_{seg}-1}{e^{V^* Pe_l Sc/Pr} - 1}$ and $c_3 = \frac{G_s d}{1 - e^{-V Pe_l \alpha_l/\alpha_s}}$. $Pe_l = V_p d/\alpha_l$ is the Peclet number, $Pr = \nu/\alpha_l$ is the Prandtl number, $Sc = \nu/D$ is the Schmidt number. In this

[2] $Z = z/d$

study, $Pr = 1.167 \cdot 10^{-2} << 1$, indicating a much larger "thermal" boundary layer compared with the velocity boundary layer; while $Sc = 3.8$, indicating a comparable boundary layer thickness for mass transfer and momentum transfer. In addition, we are interested to study the system for $V_p \in [20, 150]$ mm/min based on the current experimental results reported by Varian Semiconductor [25] . Thus, $Pe_l \in [0.143, 1.0729]$ and $Pe_l Sc/Pr \in [47.6, 357.14]$, where one can see that convection plays an important role in the HRG process for the solute distribution, in contrast, convection can be neglected in heat transfer.

The typical nondimensional temperature and concentration base state profiles are shown in Figure 4.3. Conditions used for simulation are: W=100, G_l=300 K/cm, $C_\infty = 10ppm$, Pe_l=1.073,0.7153,0.1431 correspond to V_p=150, 100, 20 mm/min, respectively. Temperature profile in both solid and liquid phase is approximately linear, indicating the absence of thermal convection (we assume a temperature difference of 300K in the melt) while the concentration profile shows the rejection of impurity at the interface. And the nonlinear profile indicates that convection plays an important role for impurity distribution.

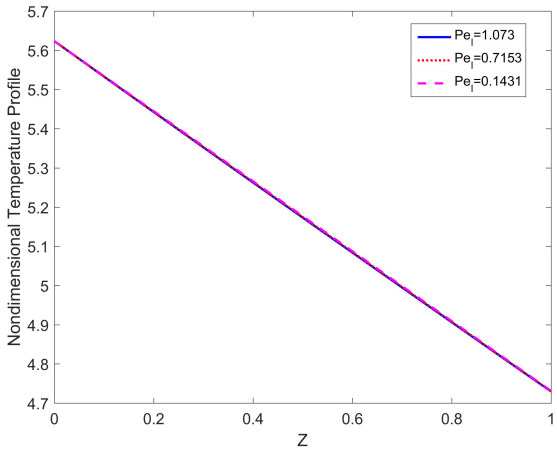

(a) Dimensionless Temperature Profile in the solid phase

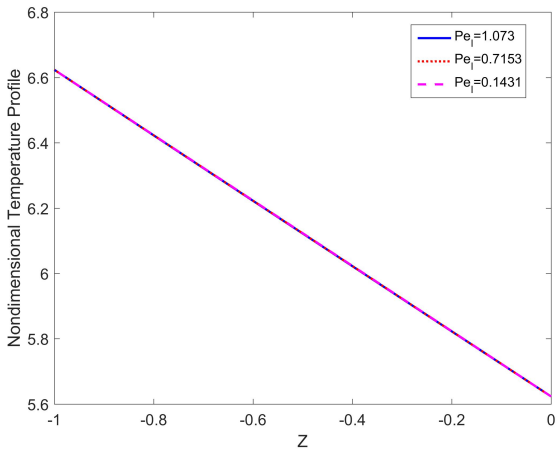

(b) Dimensionless Temperature Profile in the liquid phase

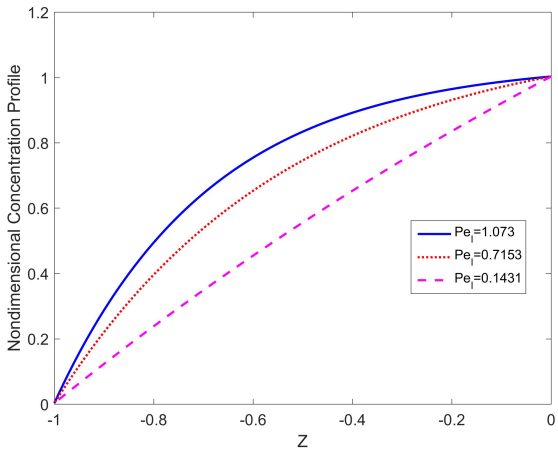

(c) Dimensionless Concentration Profile in the liquid phase

Figure 4.3: Dimensionless Profiles for W=100, G_l=300 K/cm, $C_\infty = 10ppm$, Pe_l=1.073,0.7153,0.1431 correspond to V_p=150, 100, 20 mm/min, respectively.

4.4 Linear Stability Analysis of the interface

To test whether the base-state is stable, we assume a normal mode perturbation (in x direction) to the interface. As a result, the thermal, solutal and flow fields are also perturbed. As time proceeds, the imposed disturbances can either grow or decay depending on the stability of the system as a function of wavenumber k. In this section we present a derivation for the system of differential equations, we develop the dispersion relation at different operating conditions that describes the correlation between wavenumber k and the growth rate, σ and, finally, we perform a neutral stability analysis in order to identify the limits of stable operating conditions.

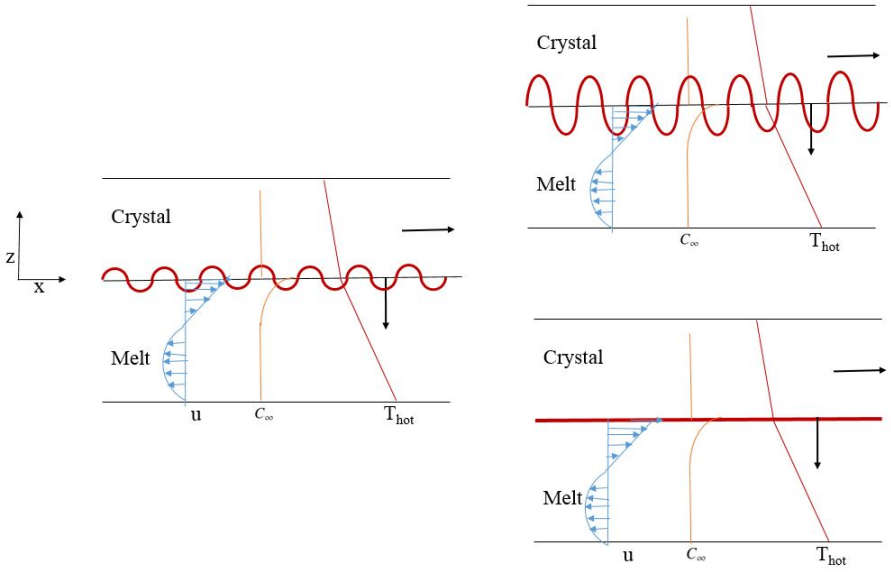

Figure 4.4: Representation of Stability Analysis

4.4.1 Derivation Outline

We write the velocity, temperature,concentration profile and the interface position as normal mode expansions:

$$\mathbf{u}' = \mathbf{u}_0(z) + \hat{\mathbf{u}}(z)\exp(\sigma t + ikx), \tag{4.16}$$

$$T_l' = T_{l0}(z) + \hat{T}_l(z)\exp(\sigma t + ikx), \tag{4.17}$$

$$T_s = \mathbf{T}_{s0}(z) + \hat{T}_s(z)\exp(\sigma t + ikx), \tag{4.18}$$

$$C' = \mathbf{C}_0(z) + \hat{C}(z)\exp(\sigma t + ikx), \tag{4.19}$$

$$z_i = \hat{\delta}\exp(\sigma t + ikx), \tag{4.20}$$

where k is the wave number of the perturbation and σ its growth rate. $\hat{u_z}$, $\hat{T_l}$, $\hat{T_s}$, and $\hat{C}$ are, respectively, the Z-dependent amplitude functions of the perturbed velocity (vertical component), temperature, and concentration.

These expansions are substituted into Eqn. (4.3)-(4.6), as well as the boundary conditions represented in Eqn. (4.7)-(4.11). Thence, we derive the following linearized ordinary different equations for the perturbed phases that govern the linear stability.

$$\begin{aligned}(\mathcal{D}^2 - k^2)[(\mathcal{D}^2 - k^2) + \mathcal{D}V^* Re - iku_{x0}Re]\hat{u_z} + ik\mathcal{D}^2 u_{x0}Re - \frac{Ra}{Pe_l}k^2\hat{T_l} \\ -\frac{Rm}{(Pe_l Sc/Pr)}k^2\hat{C} = (\mathcal{D}^2 - k^2)\sigma Re\hat{u_z},\end{aligned} \tag{4.21}$$

$$[(\mathcal{D}^2 - k^2) + V^* Pe_l\mathcal{D} - iku_{x0}Pe_l]\hat{T_l} - (\mathcal{D}T_{l0})\hat{u}_z Pe_l = \sigma\hat{T_l}Pe_l, \tag{4.22}$$

$$[(\mathcal{D}^2 - k^2) + V(Pe_l\alpha_l/\alpha_s)\mathcal{D}]\hat{T_s} = \sigma\hat{T_s}(Pe_l\alpha_l/\alpha_s), \tag{4.23}$$

$$\begin{aligned}[(\mathcal{D}^2 - k^2) + V^*(Pe_l Sc/Pr)\mathcal{D} - iku_{x0}(Pe_l Sc/Pr)]\hat{C} \\ -(\mathcal{D}C_0)\hat{u}_z(Pe_l Sc/Pr) = \sigma\hat{C}(Pe_l Sc/Pr),\end{aligned} \tag{4.24}$$

in which $\mathcal{D} = \frac{\partial}{\partial Z}$ represents the differential operator. $Re = V_p d/\nu$ is the Reynolds number, $Ra = a_1 g\beta d^4/\alpha_l\nu$ is the Rayleigh number, and $Rm = a_2 g d^4/D\nu$.

The solid phase temperature can be solved analytically to give

$$\hat{T}_s = c_4 \exp(c_5 Z), \tag{4.25}$$

where c_4 and c_5 are constants. Then we can substitute back to Eqn. (4.23) and arrive at:

$$c_5 = -VPe_l\alpha_l/\alpha_s + \sqrt{(VPe_l\alpha_l/\alpha_s)^2 - 4(\sigma Pe_l\alpha_l/\alpha_s - k^2)}. \tag{4.26}$$

The constant c_4 can be trivially determined from the top surface cooling condition, however, it is not needed in the analysis. At the interface, the accompanying boundary conditions for velocity satisfying the definition of initial amplitude of the perturbation and the continuity equation, respectively, are

$$\hat{u}_z = -\epsilon\hat{\delta}\sigma, \tag{4.27}$$

$$\mathcal{D}\hat{u}_z = (\epsilon k^2 + ik\mathcal{D}u_{x0})\hat{\delta}. \tag{4.28}$$

The Stefan condition, mass conservation of the impurity and Gibbs-Thomson relation [55] can be re-written as :

$$\hat{\delta}\sigma\frac{L_v V_p}{k_l G_l} = -\mathcal{D}\hat{T}_l + \frac{k_s}{k_l}\frac{c_5}{d}\hat{T}_l + \hat{\delta}[V^* Pe_l - V(Pe_l\alpha_l/\alpha_s)\frac{k_s G_s}{k_l G_l} + \frac{k_s}{k_l}\frac{c_5}{d}\frac{(G_l - G_s)}{G_l}], \tag{4.29}$$

$$(1-k_{seg})V\hat{C} + \frac{1}{(1+\epsilon)(Pe_l\alpha_l/D)}\mathcal{D}\hat{C} = \hat{\delta}(k_{seg}V - \sigma\frac{1-k_{seg}}{k_{seg}}C_\infty), \tag{4.30}$$

$$\frac{mG_c}{G_l}\hat{C} - \hat{T}_l = \hat{\delta}(1 - \frac{mG_c}{G_l} + T_m\Gamma k^2), \tag{4.31}$$

while at the $Z = -1$ (the rigid planar isothermal boundary)

$$\hat{u}_z = \mathcal{D}\hat{u}_z = \hat{T}_l = \hat{C} = 0. \tag{4.32}$$

Equations (4.21),(4.22) and (4.24) can be written as

$$L\begin{bmatrix}\hat{u}_z\\ \hat{T}\\ \hat{C}\end{bmatrix} = \sigma\begin{bmatrix}H & 0 & 0\\ 0 & Pe_l & 0\\ 0 & 0 & Pe_l\alpha_l/D\end{bmatrix}\begin{bmatrix}\hat{u}_z\\ \hat{T}\\ \hat{C}\end{bmatrix}, \tag{4.33}$$

where $H = Re(\mathcal{D}^2 - k^2)$ and the elements of the differential operator L are given by

$$L_{11} = (\mathcal{D}^2 - k^2)[(\mathcal{D}^2 - k^2) + \mathcal{D}V^*Re - iku_{x0}Re], \tag{4.34}$$

$$L_{12} = -k^2\frac{R_a}{Pe_l}, \tag{4.35}$$

$$L_{13} = -k^2\frac{R_m}{Pe_l\alpha_l/D}, \tag{4.36}$$

$$L_{21} = -\mathcal{D}T_{l0}Pe_l, \tag{4.37}$$

$$L_{22} = (\mathcal{D}^2 - k^2) + Pe_lV^*\mathcal{D} - iku_{x0}Pe_l, \tag{4.38}$$

$$L_{31} = -\mathcal{D}C_{l0}(Pe_l\alpha_l/D), \tag{4.39}$$

$$L_{33} = (\mathcal{D}^2 - k^2) + (Pe_l\alpha_l/D)V^*\mathcal{D} - iku_{x0}(Pe_l\alpha_l/D), \tag{4.40}$$

and $L_{23} = L_{32} = 0$.

4.4.2 Dispersion Relation

The eigenvalue problem Eqn. (4.33) is solved numerically by utilizing a second-order central finite difference scheme to the differential operators $\mathcal{L}$ and $\mathcal{H}$. Then we arrive at the following general eigenvalue problem

$$\begin{bmatrix} \mathcal{L}_{11} & \mathcal{L}_{12} & \mathcal{L}_{13} \\ BC1 & 0 & 0 \\ \mathcal{L}_2 1 & \mathcal{L}_{22} & 0 \\ BC2 & BC2 & BC2 \\ \mathcal{L}_{31} & 0 & \mathcal{L}_{33} \\ 0 & BC3 & BC3 \\ 0 & BC4 & BC4 \\ BC5 & 0 & 0 \\ BC6 & 0 & 0 \\ 0 & BC7 & 0 \\ 0 & 0 & BC8 \end{bmatrix} \begin{bmatrix} \hat{u}_z \\ \hat{T} \\ \hat{C} \end{bmatrix} = \sigma \begin{bmatrix} \mathcal{H} & 0 & 0 \\ 0 & BC1 & BC1 \\ 0 & 1 & 0 \\ 0 & 0 & 0 \\ 0 & 0 & 1 \\ 0 & BC3 & BC3 \\ 0 & BC4 & BC4 \\ 0 & 0 & 0 \\ 0 & 0 & 0 \\ 0 & 0 & 0 \\ 0 & 0 & 0 \end{bmatrix} \begin{bmatrix} \hat{u}_z \\ \hat{T} \\ \hat{C} \end{bmatrix} \tag{4.41}$$

where Eqn. (4.31) is used to represent unknown $\hat{\delta}$ as function of $\hat{u}_z$, $\hat{T}$, and $\hat{C}$. We obtain the eigenvalue and eigenvectors of the system using the DGGEVS solver of the LAPACK package. Results presented are based on Z-discretization of 500 nodes. Eigenvalues are also checked by increasing the number of nodes to ensure the accuracy.[3] The growth rate σ is calculated for the parameters of Table 4.2 at different operating conditions.

[3]see appendix section for the eigenvalue convergence plot

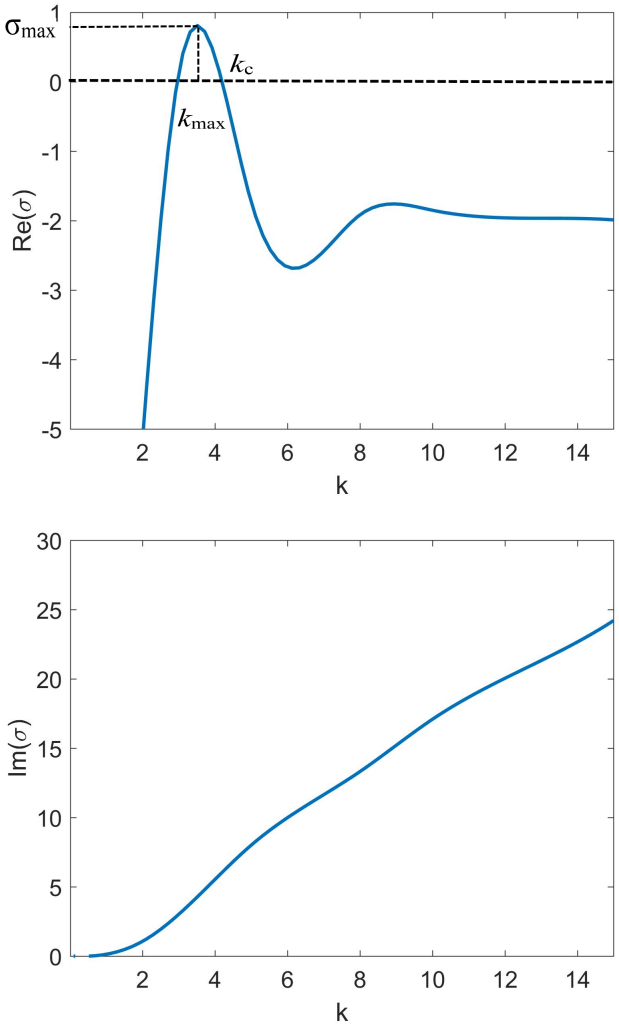

Figure 4.5: Dimensionless dispersion relation for W=300, G_l=300 K/cm, V_p=20 mm/min, $C_\infty = 100ppm$.

A typical dispersion relation where $\sigma = f(k)$ is shown in Figure 4.5 for pulling velocity=20 mm/min, G_l = 300 K/cm and W=300. The unstable modes exist for a range of wavenumber where $Re(\sigma) > 0$. The most unstable mode occurs at k_{max} and corresponds to σ_{max}. Instability will first appear with a wavelength of $2\pi/k_{max}$ and on a time scale of $2\pi/\sigma_{max}$. The critical wave number is represented by k_c above which all modes are stable ($Re(\sigma) < 0$). At the onset of instability, $Re(\sigma) = 0$ and the shape of the interface is defined by $z_i = \hat{\delta} exp(\sigma_i t + ikx)$. For the corresponding convective instability, the speed

of the traveling wave is $Im(\sigma)/k$.

Table 4.2: Material Properties and Parameters used in the model. Adapted from [36]

Parameter	Symbol	Value
Melting temperature	T_m	$1687K$
Thermal Conductivity of liquid silicon	k_l	$58\frac{W}{mK}$
Thermal Conductivity of solid silicon	k_s	$18\frac{W}{mK}$
Density of liquid silicon	ρ_l	$2570\frac{kg}{m^3}$
Density of solid silicon	ρ_s	$2293\frac{kg}{m^3}$
Thermal diffusivity of liquid silicon	α_l	$2.33 \cdot 10^{-5}\frac{m^2}{s}$
Thermal diffusivity of solid silicon	α_s	$7.54 \cdot 10^{-6}\frac{m^2}{s}$
Mass diffusivity of Al-Si	D	$7 \cdot 10^{-8}\frac{m^2}{s}$
Latent heat of fusion	L_v	$1.79 \cdot 10^{6}\frac{J}{kg}$
Segregation coefficient of Al-Si	k_{seg}	$2.83 \cdot 10^{-3}$
Capillary constant	Γ	$8.99 \cdot 10^{-11}$
Slope of the liquidus line	m	$-9.5 \cdot 10^{-5}\frac{K}{ppm}$
Kinematic viscosity of silicon	ν	$2.72 \cdot 10^{-7}\frac{m^2}{s}$
Prandtl number	P_r	$1.167 \cdot 10^{-2}$
Schmidt number	S_c	3.886

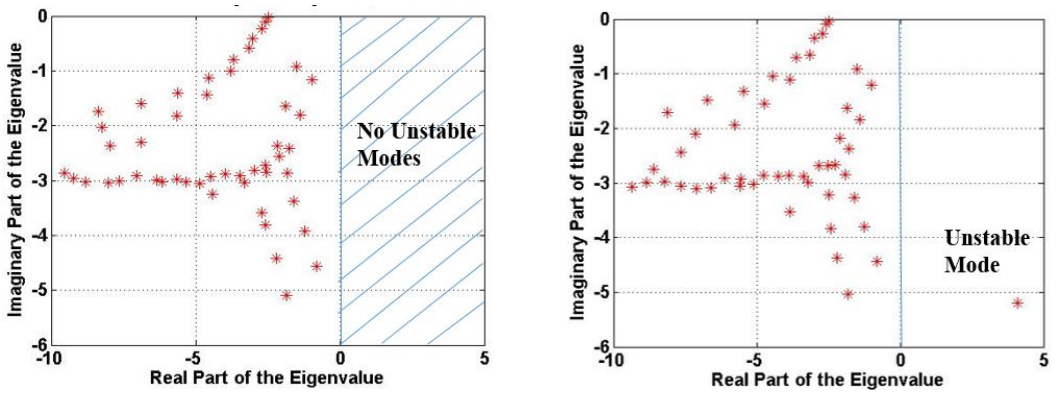

(a) Growth Rate for Pulling Velocity=120mm/min, Wedge Factor=500, $C_\infty = 99ppm$ and $k = 30$.

(b) Growth Rate for Pulling Velocity=120mm/min, Wedge Factor=500, $C_\infty = 120ppm$ and $k = 30$.

Figure 4.6: Growth Rate for Pulling Velocity=120 mm/min, Wedge Factor=500 and $k = 30$ with different C_∞.

As shown in the Figure. 4.6a and 4.6b, we plot the real and imaginary part of the growth rate at one operating condition by fixing the pulling velocity, wedge factor, impurity concentration in the system and wave number k. The stability of the system can be determined by calculating the largest eigenvalue of the previously defined ODE system. As shown in Figure. 4.6a and 4.6b, when increasing the impurity concentration in the system while keeping all the other operating condition constant, the largest eigenvalue increases from -0.80676 to 4.08361 and the system becomes unstable.

In order to understand the causes of "wavy instability" occurred in the experiments [28, 25], the stability analysis is performed with pulling velocities of 20-150 mm/min and wedge factor W of 300-3000. The temperature gradient in the melt is set to be 200-350 K/cm.

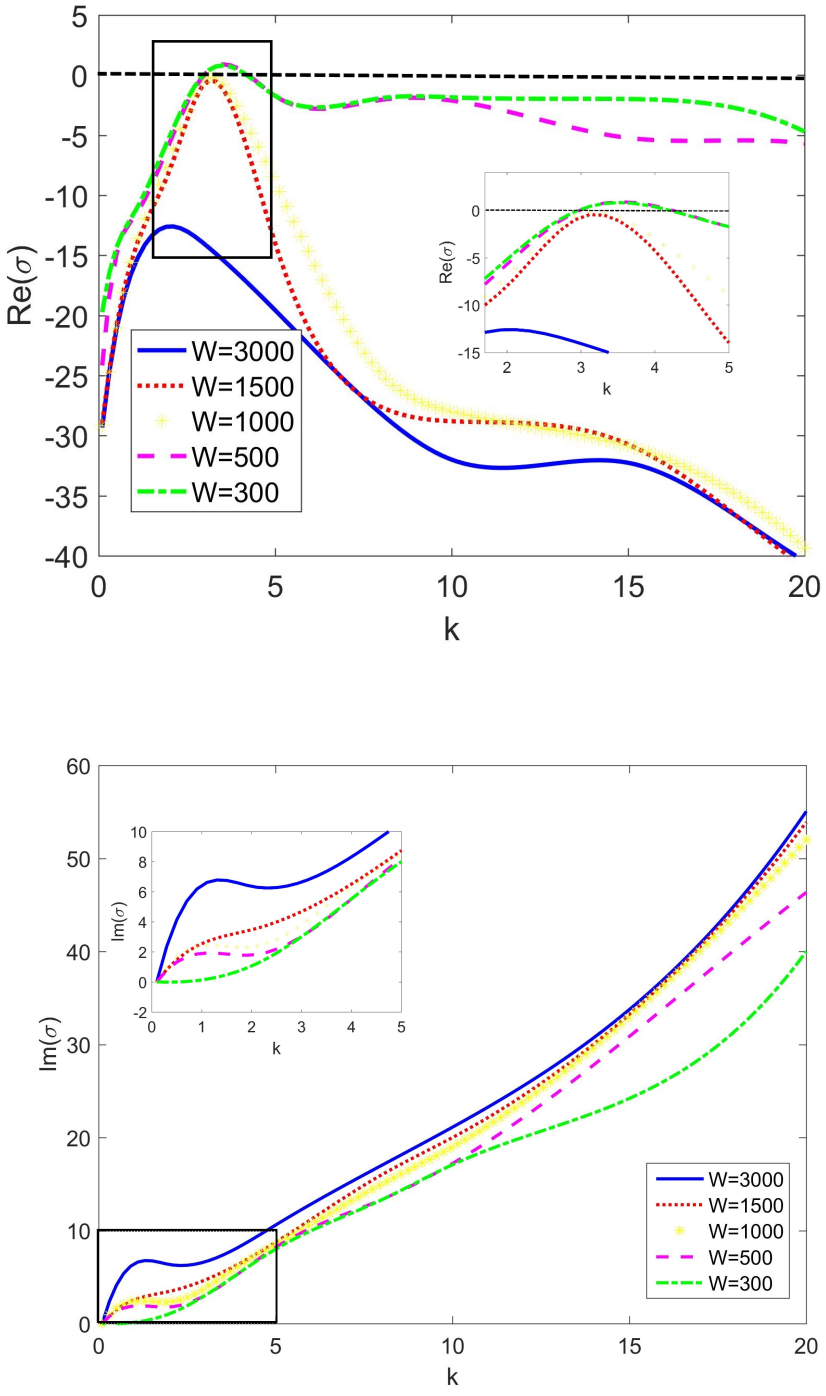

Figure 4.7: Dimensionless dispersion relation for different wedge factor at V_p=20 mm/min, Gl=300 K/cm, C_∞=100 ppm. Insets denote system behavior when instability occurs

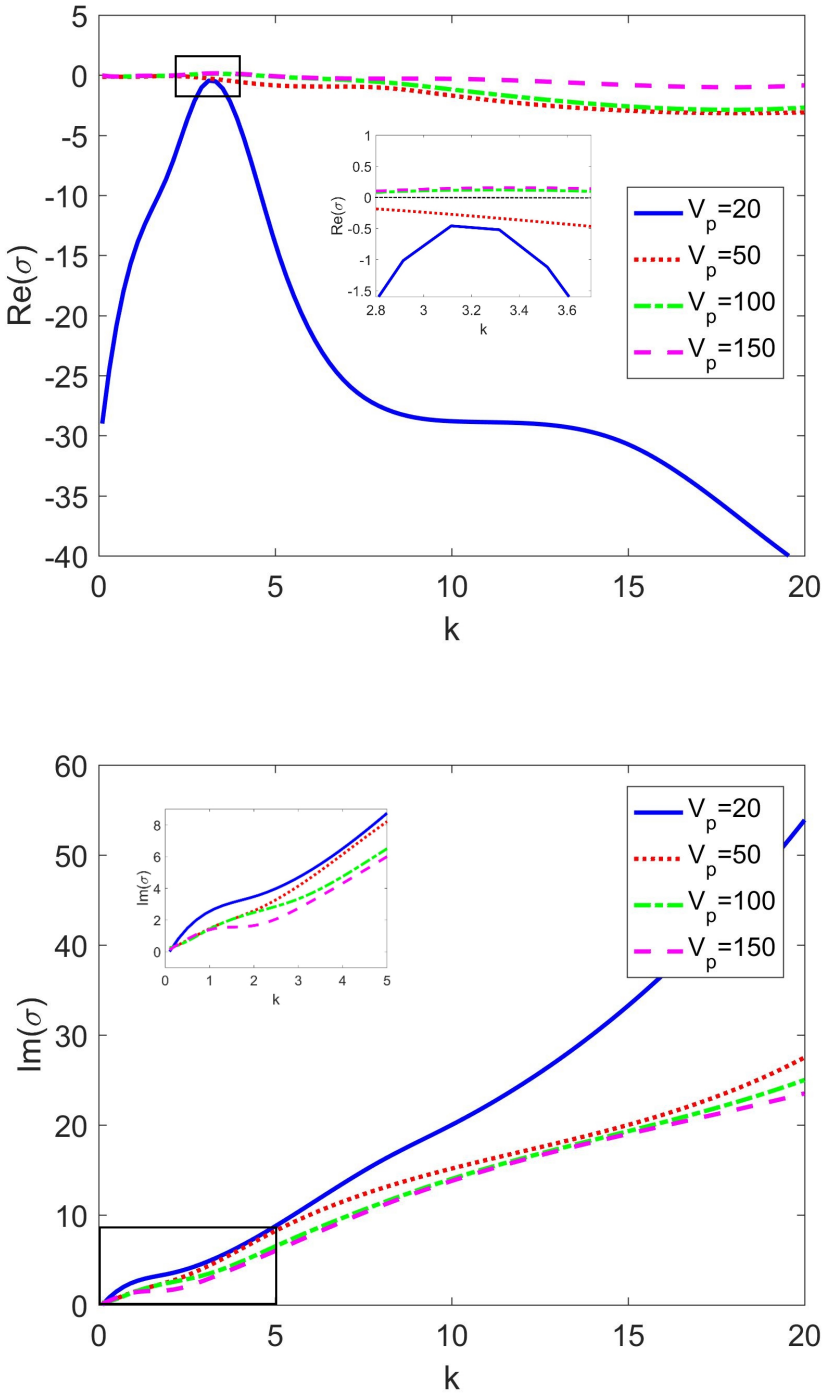

Figure 4.8: Dimensionless dispersion relation for different pulling velocity at W=1500, Gl=300 K/cm, C_∞=100 ppm. Insets denote system behavior when instability occurs

Figure 4.7 illustrates variations with the wave number of real and imaginary parts of the growth rate, $Re(\sigma)$ and $Im(\sigma)$, respectively, for different wedge factors while keeping all other operating conditions the same. At one given pulling velocity, larger wedge factor leads to slower vertical crystallization velocity, and more stable growth for the system. The most unstable mode occurs at small k_{max}. One can see that when the wedge factor is decreased, the system is more unstable. The $Im(\sigma)$ is decreasing and k_{max} is increasing, which results in faster wave speed and smaller wavelength.

Experiments have shown that the system turns unstable when trying to increase the pulling velocity while keeping all other conditions fixed [25]. As shown in Figure 4.8, one can observe that the variation of pulling velocity has a significant influence on the stability of the system. With a pulling velocity less than 50 mm/min, the crystallization interface stays stable with a relative high impurity concentration (100ppm).

We assume that the vertical crystallization velocity can be estimated directly by defining the shape of the crystal wedge together with the solid removal rate. Thus, the thickness of the resulting wafer can be estimated and controlled by manipulating the heat removal rate independently. Our ultimate goal is to optimize the HRG process to achieve a stable wafer production. Accordingly, we tested the stability condition for different heat removal rate given all other operating conditions the same. Typical temperature gradient for the silicon crystallization process is around 200K/cm and here we tested different cooling scenarios ranging from 200-350 K/cm. As shown in Figure 4.9, the stability of the system is improved when increasing the temperature gradient from 200 to 250 K/cm.

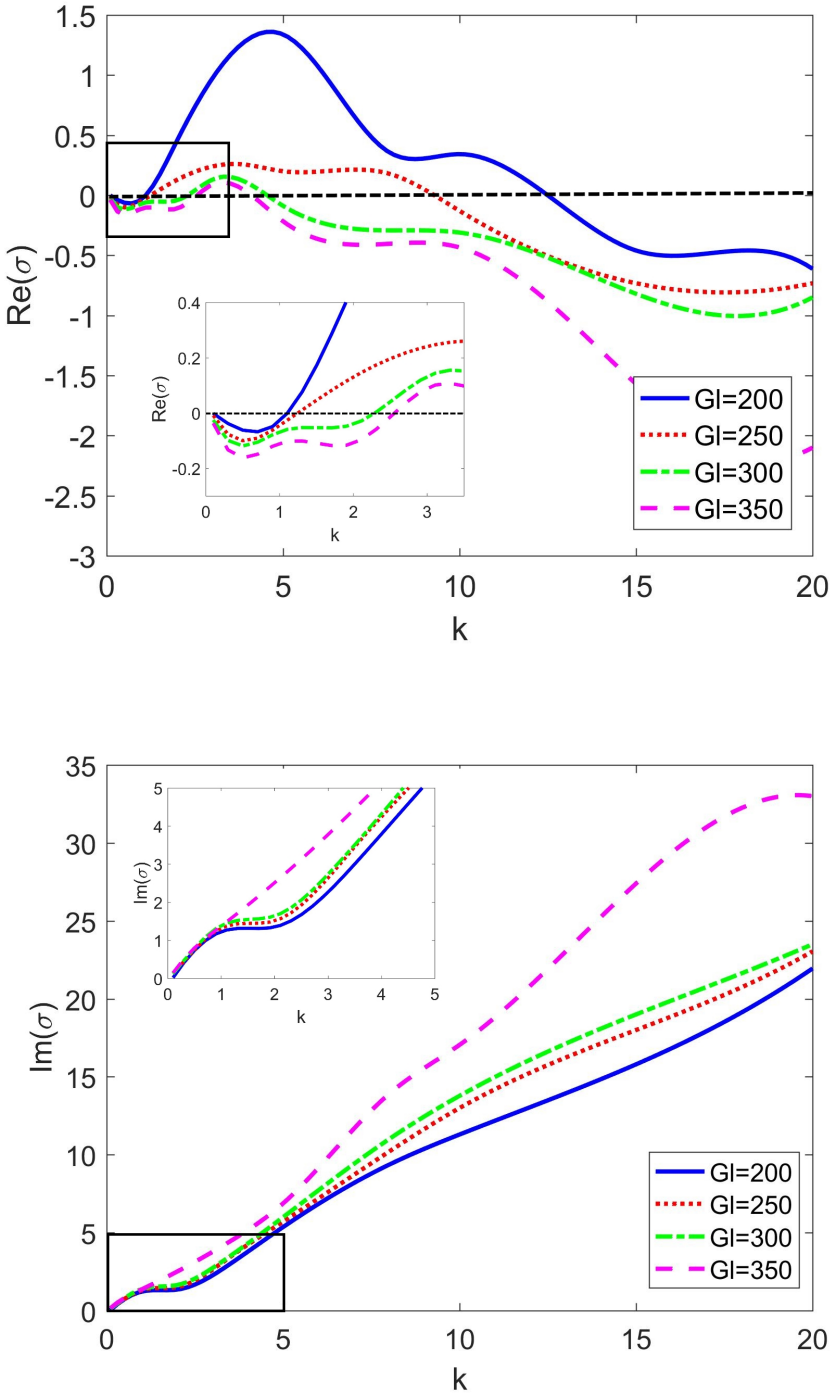

Figure 4.9: Dimensionless dispersion relation for different temperature gradient at V_p=150 mm/min, W=1500, C_∞=100 ppm.

4.4.3 Neutral Stability Results

In order to determine the onset instability as a function of impurity, pulling velocity and wedge factor, we solved the ODE system Eqn. (4.33) using MATLAB. The BVP was converted to an IVP problem and a direct numerical integration method, similar to the work for solving the Benard problem [31] and Soret-driven instability [9] is used. We transform the system of four second-order differential equations into a system of eight first-order differential equations. We then construct a general solution as a linear combination of eight linearly independent solutions of this eighth-order problem. The detailed derivation is presented as follows.

The BVP problem presented in Eqn. (4.33) can be written as a system of eight first-order differential equations, where

$$\begin{aligned} \hat{u}_z = u_1, \mathcal{D}\hat{u}_z = u_2, \\ \mathcal{D}^2\hat{u}_z = u_3, \mathcal{D}^3\hat{u}_z = u_4, \\ \hat{T}_l = u_5, \mathcal{D}T_l = u_6, \\ \hat{C} = u_7, \mathcal{D}C = u_8. \end{aligned} \tag{4.42}$$

And we can define the solution of the system of this ODE as

$$u_i = \sum_{j=1}^{8} C_j u_i^{(j)}(Z). \tag{4.43}$$

A typical way to construct these linearly independent solutions is by assuming $u_i^{(j)}(-1) = \delta_{ij}$ as initial values at $Z = -1$. As a result, the boundary condition

for $Z = -1$ become

$$\begin{aligned} u_1(-1) &= C_1 u_1^{(1)}(-1) = 0 \Rightarrow C_1 = 0, \\ u_2(-1) &= C_2 u_2^{(2)}(-1) = 0 \Rightarrow C_2 = 0, \\ u_5(-1) &= C_5 u_5^{(5)}(-1) = 0 \Rightarrow C_5 = 0, \\ u_7(-1) &= C_7 u_7^{(7)}(-1) = 0 \Rightarrow C_7 = 0. \end{aligned} \tag{4.44}$$

On the other boundary $Z = 0$, Eqn. (4.27)-(4.30) can be written as:

$$\begin{aligned} &\sum_{j=1}^{8} C_j u_1^j(0) + \epsilon\sigma \frac{\frac{mG_c}{G_l}}{1 - \frac{mG_c}{G_l} + T_m \Gamma k^2} \sum_{j=1}^{8} C_j u_7^j(0) \\ &\quad + \epsilon\sigma \frac{-1}{1 - \frac{mG_c}{G_l} + T_m \Gamma k^2} \sum_{j=1}^{8} C_j u_5^j(0) = 0, \\ &\sum_{j=1}^{8} C_j u_2^j(0) - (\epsilon k^2 + ik\mathcal{D}u_{x0}) \frac{\frac{mG_c}{G_l}}{1 - \frac{mG_c}{G_l} + T_m \Gamma k^2} \sum_{j=1}^{8} C_j u_7^j(0) \\ &\quad + (\epsilon k^2 + ik\mathcal{D}u_{x0}) \frac{-1}{1 - \frac{mG_c}{G_l} + T_m \Gamma k^2} \sum_{j=1}^{8} C_j u_5^j(0) = 0, \\ &\frac{\sigma L_v V_p}{k_l G_l} \Big(\frac{\frac{mG_c}{G_l}}{1 - \frac{mG_c}{G_l} + T_m \Gamma k^2} \sum_{j=1}^{8} C_j u_7^j(0) + \frac{-1}{1 - \frac{mG_c}{G_l} + T_m \Gamma k^2} \sum_{j=1}^{8} C_j u_5^j(0) \Big) \\ &\quad + \sum_{j=1}^{8} C_j u_6^j(0) - \frac{k_s c_4}{k_l d} \sum_{j=1}^{8} C_j u_5^j(0) + (V^* Pe_l - V Pe_l \alpha_l / \alpha_s \frac{k_s G_s}{k_l G_l} + \frac{k_s}{k_l} c_4 \frac{G_l - G_s}{G_l}) \\ &\quad \Big(- \frac{\frac{mG_c}{G_l}}{1 - \frac{mG_c}{G_l} + T_m \Gamma k^2} \sum_{j=1}^{8} C_j u_7^j(0) + \frac{1}{1 - \frac{mG_c}{G_l} + T_m \Gamma k^2} \sum_{j=1}^{8} C_j u_5^j(0) \Big) = 0, \\ &(1 - k_{seg}) V \sum_{j=1}^{8} C_j u_7^j(0) + \frac{1}{(1+\epsilon) Pe_l Sc/Pr} \sum_{j=1}^{8} C_j u_8^j(0) + \Big(\frac{\frac{mG_c}{G_l}}{1 - \frac{mG_c}{G_l} + T_m \Gamma k^2} \\ &\quad \sum_{j=1}^{8} C_j u_7^j(0) + \frac{-1}{1 - \frac{mG_c}{G_l} + T_m \Gamma k^2} \sum_{j=1}^{8} C_j u_5^j(0) \Big) \Big(k_{seg} V - \sigma \frac{1 - k_{seg}}{k_{seg}} C_\infty \Big) = 0. \end{aligned} \tag{4.45}$$

We can convert the BVP to an IVP with one more constraint to ensure the existence of nontrivial solutions for C_j such that the coefficient determinant

of the algebraic system must vanish. The parameter values that make the determinant vanish correspond to the critical values at the onset of instability. In this way we can identify the corresponding combinations of operating conditions that guarantee stable operation. For $j = 3, 4, 6, 8$, the previously defined ODE's are solved as IVP at $Z = -1$ with 4 different initial values for each u^j in order to obtain their values at $Z = 0$. The determinant condition of this 4×4 matrices yields a quadratic relation for the $C_\infty - \sigma$. And the initial dispersion relation provides a good initial guess to the solution. Due to the complexity of the calculation, we solved the problem numerically by setting the $\sigma_{real} = 0$ and scan on the $C_\infty - \sigma$ plane for given fixed k and other system parameters to locate the region of approximate solution. A more restricted region for $C_\infty - \sigma$ and careful iterative criteria are necessary in the region near the bifurcation point where oscillatory and non-oscillatory modes branch off.

To ensure stability, the largest real part of the growth rate has to be less or equal to zero for any given k and we represent this critical impurity concentration as C^*_∞ by searching for the minimum $C_\infty(k)$ for a given pulling velocity and wedge factor. The computational results are summarized in figure 4.10, given a fixed temperature gradient $G_l = 200$ K/cm. From the neutral stability curve, one can easily identify corresponding stable operation condition. Higher temperature gradient will shift the neutral stability curve upwards, given all other conditions the same. It should be noted that although appearance of the instability can be predicted by the current study, the morphological evolution of unstable modes is not predicted.

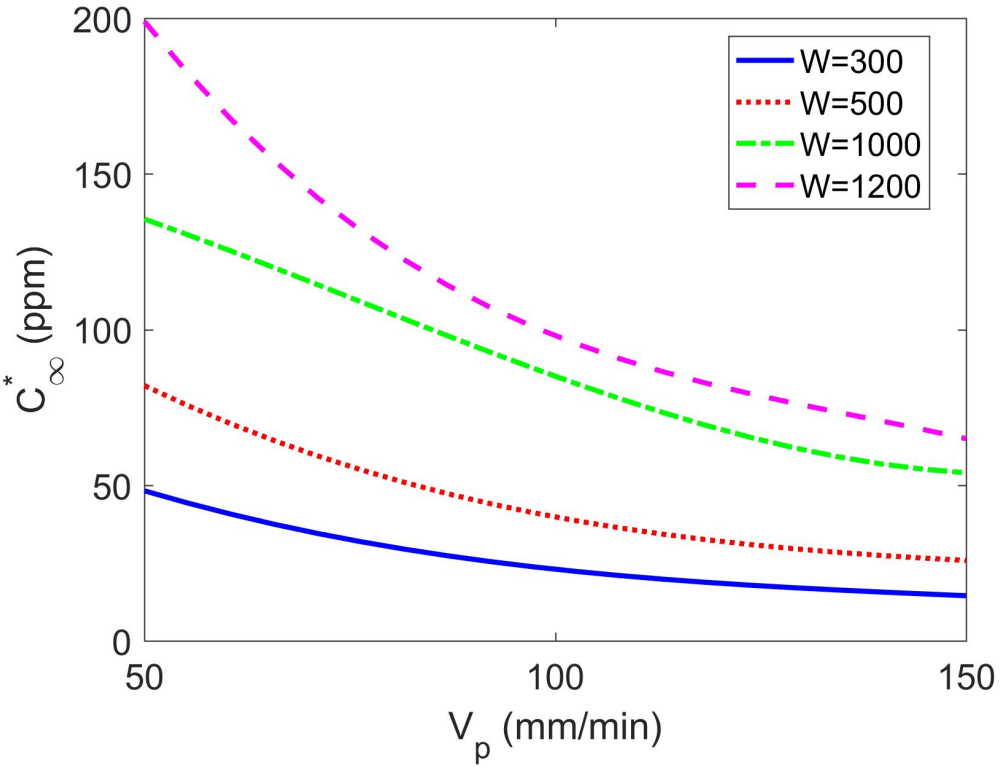

Figure 4.10: The influence of the wedge factor(W) and pulling velocity(V_P) on the impurity concentration neutral curve (Gl=200 K/cm).

4.5 Conclusions and contributions

We presented a theoretical analysis based on the principles of linear stability analysis to study the crystallization interface formed within the HRG process. To achieve this, we developed a two-dimensional model of the system, which allows us to analyze the importance of different operating parameters on the overall stability of the former. In order to properly capture the phase change behavior, we derived the profiles for thermal, solutal and flow fields under the imposed small-amplitude sinusoidal perturbations, in a non-dimensional form. The calculation of the dispersion relation for various pulling speeds, temperature gradient and wedge factors allowed us to identify stable regions regarding the wavenumber in question. Moreover, the neutral stability relationship that

we extracted provides valuable insights on future experimental development and draws an upper bound for possible unstable modes. Specifically, the two factors that our analysis identified to be essential to the stability of the system are the steep temperature gradient in the melt, and the low vertical crystallization velocity. These conditions can be achieved by ensuring sufficient heat removal and high wedge factors. We validated our findings, and we found them to be consistent with the prior experimental results shown by Varian Semiconductor Inc. In addition, we demonstrated that the HRG process showed the potential achieve higher production speed that would allow for its commercial exploitation for the mass production of silicon wafers. The findings in this chapter can serve as a guide for future experimental verification of the HRG process, improvement on process design, control, and optimization.

Chapter 5

A cellular automata approach for simulation of crystal growth

5.1 Introduction and Literature Review

Interface instabilities have been observed in experimental studies of the HRG process. These include:

1. Dendritic growth is observed when the pulling velocity is increased.
2. The sharp wedge formation when an active cooling source is used, which results in undesired high thickness and unstable growth.
3. The unstable/non-smooth crystallization interface.

Although the non-smooth interface can be compensated by further heat treatment (re-melting process via detailed control design) or polishing, the optimum solution is to reduce or restrict the level of non-smoothness during the initial growth process. Thus, detailed understanding of phenomena associated with the formation of sharp wedge becomes crucial for the successful development and control of the HRG process.

To that end, various numerical methods have been developed to study the dendritic growth during solidification, such as level set methods [20], front tracking methods [23], phase field models [24, 54], and cellular automata [35, 33, 19, 18, 56, 57].

The Cellular Automaton (CA) based mathematical models have the advantage that it can balance the trade-off between computational workload and quantitative representation of solidification microstructures. The CA models have been developed to study grain growth at meso-scale levels [33, 19, 18], and for dendritic growth at micro-scale levels [56, 57, 35]. They can be coupled with finite element methods to solve the energy conservation equation at the scale of crystal growth, and provides a bridge between micro and macro level phenomena during the crystal growth.

Two major challenges raised for the CA based mathematical models:

1. Determine the growth velocity of the liquid/solid interface via conservation law or kinetics.

2. Eliminate artificial anisotropy term caused by the square mesh

Nastac [35] developed stochastic model incorporating time dependent calculation for temperature and solute distribution in the solid and liquid phases. In this study, the growth velocity is obtained by its x and y cartesian components, while artificial anisotropy of the CA mesh is not accounted for. Wang et al. [52] developed a combined cellular automaton-finite difference model to study solute diffusion controlled solidification phenomena. In this study, the growth velocity of liquid/solid interface is determined by the equilibrium condition at the interface. The model includes both constitutional and curvature undercooling. Dendrites with different orientations are obtained. Zhu and Hong [56] developed a modified CA model that incorporates either analytical

theories (such as Kurz-Giovanola-Trivedi model [29]) or kinetic coefficient for calculation of velocity for liquid/solid interface.

5.2 Cellular Automata model and numerical algorithm

Figure 5.1 shows a schematic representation of the effect of solute composition on the morphology of liquid/solid interface for graphitic iron [1, 49], where instabilities at different scale levels can be observed. The present work is motivated by the experimental observation from Varian Semiconductor, shown in Figure 2.7, where a sharp $< 1, 1, 1 >$ facet is formed with high thickness and non-smooth/unstable interface. We developed a mathematical model that combines CA with Finite difference method to investigate the evolution of crystallization, dendritic growth, and sharp wedge formation in the HRG process. The CA algorithm is incorporated with the transport model for calculating thermal and mass transfer for diffusion. We consider the static case and convection is not included for the current study. Constitutional and curvature undercooling effects are considered for the equilibrium interface temperature. Two different scenarios are considered: diffusion controlled growth and kinetics controlled growth. We started with the simple counting cell methods for curvature calculation and performed case studies displaying growth evolution under different cooling conditions. We propose a further improvement utilizing an updated mesh anisotropy method. A kinetics controlled model is also developed to understand the HRG process.

The crystallization of silicon with impurity is governed by the evolution of temperature $T(x, y)$ and concentration $C(x, y)$ fields that satisfies boundary conditions of the moving liquid/solid interface as well as process cooling and

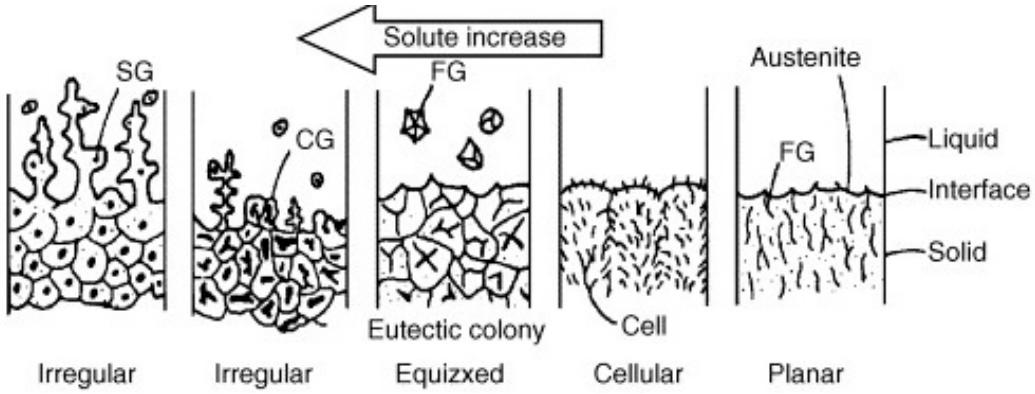

Figure 5.1: Schematic representation of the solid/liquid interface morphology: Influence of solute composition. Graphic taken from [1, 49].

heating conditions. The two dimensional computation domain is divided into uniform square shape cells. Each cell is defined by the following characteristics: temperature, concentration, solid fraction, cell state (solid, interface or liquid).

To start the process: an initial seed is assigned, and uniform temperature and solute composition is assumed for the entire domain. Heat is removed from the top surface and as time proceed, temperature starts to decrease and solidification starts. As solidification proceeds, latent heat is released, and solute is rejected, which results in a local gradient in both thermal and solutal field near the liquid/solid interface. The equilibrium condition is affected by the new thermal and solutal fields.

The CA operates at discrete time steps and the cell variables are updated based on local rules defined by physical model and derivations. The governing equations for thermal and solutal fields, interface conditions, anisotropy, and kinetics are described in detail below.

- Thermal Field

The governing equation for transient heat conduction is defined as:

$$\frac{\partial T}{\partial t} = \nabla \cdot (\alpha \nabla T) + \frac{\triangle H}{C_p} \frac{\partial f_s}{\partial t}. \tag{5.1}$$

where T is the temperature, t is the time, α is the thermal diffusion coefficient, $\triangle H$ is the latent heat of solidification, f_s is the solid fraction and C_p is specific heat. We consider constant flux conditions for the top and bottom boundary, while no heat flux is assumed for the left and right boundary. The heat conservation equation is discretized by second order centered finite difference scheme.

- Solute distribution

We assume the solute distribution is controlled by diffusion in the liquid and solid phases. As solidification proceed, impurities are rejected by the solidified cells and pushed towards the neighboring cells. The diffusion mechanism of solute in the domain is represented by:

$$\frac{\partial C_i}{\partial t} = \nabla \cdot (D_i \nabla C_i) + (1 - k_{seg}) C_i \frac{\partial f_s}{\partial t}. \tag{5.2}$$

where the subscript i denotes for liquid or solid phase and C_i is the concentration of impurity. D_i is the solute diffusion coefficient, k_{seg} is the segregation coefficient. We also assume local equilibrium at solid-liquid interface so that:

$$C_s^* = k_{seg} C_l^*. \tag{5.3}$$

where the superscript $^{[*]}$ denotes for value at the interface.

We solve the following equivalent solute diffusion equations to simplify the discontinuous transition at the interface when solidification occurs. We define an equivalent solute concentration C_e and the equivalent diffusion coefficient D_e as follows:

- For the liquid state:

$$C_e = C_l, D_e = D_l, \tag{5.4}$$

- For the interface:

$$C_e = C_l, D_e = D_l, \tag{5.5}$$

- For the solid state:

$$C_e = C_s/k_{seg}, D_e = D_s. \tag{5.6}$$

And Eqn. (5.2) can be re-written as:

$$\frac{\partial C_e}{\partial t} = \nabla \cdot (D_e \nabla C_e) + (1 - k_{seg}) C_e \frac{\partial f_s}{\partial t}. \tag{5.7}$$

Thus, the solute distribution of the entire domain can be obtained by solving the equivalent governing equation Eqn. (5.7), and the concentration of specific phases can be calculated from C_e accordingly.

- Interface Condition

The interface equilibrium temperature is defined as:

$$T^* = T_l^{eq} + (C_l^* - C_0)m - \Gamma K f(\phi, \theta). \tag{5.8}$$

where T_l^{eq} is the equilibrium temperature with impurity concentration C_0, m_l is the liquidus slope, Γ is the Gibbs-Thomson coefficient, K is the curvature of interface, $f(\phi, \theta)$ represents for the anisotropic term. ϕ and θ represent for growth angle and preferred growth direction, respectively. Thus, we obtain T^* from the heat conservation equation 5.1 and we can calculate corresponding equilibrium interface concentration C_l^* accordingly.

The local cell solid fraction f_s is defined as follows:

$$\Delta f_s = \frac{C_l^* - C_l}{C_l^*(1 - k_{seg})}. \tag{5.9}$$

where the local solute concentration C_l is obtained from the solute distribution governing equation. When a crystal seed is surrounded by supercooled liquid, the local equilibrium concentration exceed the actual local liquid concentration. In order to reach the equilibrium condition, solidification starts and f_s starts to increase. Specifically, a positive numerator represents increasing local solid fraction. To ensure numerical stability, we apply the constraint $\Delta f_s(t_n) = \min(\Delta f_s(t_1) - f_s(t_{n-1}))$ so that the interface will not move out of the current cell within one time step. f_s can now be updated every time step by $f_s(t_{n+1}) = f_s(t_n) + \Delta f_s(t_n)$. When $f_s = 1$, the interface cell change its state to solid, while when $f_s = 0$, this interface cell changes its state to liquid.

For interface cells with non-zero f_s, both liquid and solid composition are calculated every time step, where the corresponding solid composition for the cell is defined as:

$$C_s = \frac{\sum_{i=1}^{i=n} \Delta f_s(t_i) k_{seg} C_l(t_i)}{f_s(t_i)}. \tag{5.10}$$

The curvature of the interface is defined using a counting cell technique that approximate the average geometric curvature, as represented by Eqn. (5.11).

$$K = \frac{1}{d}[1 - 2\frac{f_s + \sum_{n=1}^{N} f_s(n)}{N+1}]. \tag{5.11}$$

where d here is the length of each cell, N is the total number of neighboring cells. We consider the Von Neumann neighborhood here (so that $N = 4$). This equation is taken from Nastac [35], and it was originally proposed by Sasikumar and Sreenivasan [44]. This representation quantifies the state of neighboring cells, but the distance effect is not considered.

The anisotropy of the interface is calculated so that:

$$f(\varphi, \theta) = 1 - \delta \cos[4(\varphi - \theta)]. \tag{5.12}$$

where the anisotropy coefficient is set such that $\delta = 0.04$ for this study and θ is the preferred growth angle. The growth angle φ is defined as:

$$\varphi = \arccos \frac{\frac{\partial f_s}{\partial x}}{[(\frac{\partial f_s}{\partial x})^2 + (\frac{\partial f_s}{\partial y})^2]^{1/2}}. \tag{5.13}$$

We apply two update conditions for the interface and solid phase cells with non-zero solid fraction f_s:

$$\delta T = \Delta f_s \frac{\Delta H}{C_p}, \tag{5.14}$$

$$\delta C = \Delta f_s (1 - k_{seg}) C_l. \tag{5.15}$$

where ΔH represents for the latent heat of fusion and δC is the solute accumulated for interface cells or rejected for the solid cells. For cells with $f_s = 1$, the solute is rejected to the neighboring liquid or interface cells evenly to ensure mass conservation. In this model, the local growth velocity is defined as:

$$V = \Delta f_s \frac{d}{\Delta t} \tag{5.16}$$

The time step used for each iteration is given by:

$$dt = \frac{1}{5} \min(\frac{d}{V_{max}}, \frac{d^2}{D_l}, \frac{d^2}{D_s}), (\Delta f_s < 10^{-3}) \tag{5.17}$$

$$= \frac{1}{10} \min(\frac{d}{V_{max}}, \frac{d^2}{D_l}, \frac{d^2}{D_s}), (\Delta f_s \geqslant 10^{-3}) \tag{5.18}$$

where d is the mesh size (in this study, d is uniform and constant in both x and y directions) and V_{max} is the maximum local growth velocity that can be obtained by scanning all interface growth velocities for the entire domain.

We assume heterogeneous nucleation for randomly chosen nucleation sites, which activate at a critical undercooling rate. We adopted a continuous nucleation model based on Gaussian distribution where the density of nucleation

$n(\Delta T)$is expressed by:

$$n(\Delta T) = \int_0^{\Delta T} \frac{dn}{d(\Delta T')} d(\Delta T'), \tag{5.19}$$

where $\frac{dn}{d(\Delta T')}$ represents the increase in nucleation density dn when the local undercooling rate $d(\Delta T')$ is increased, and $\frac{dn}{d(\Delta T')}$ is defined by the following equation under Gaussian normal distribution:

$$\frac{dn}{d(\Delta T)} = \frac{n_{max}}{\sqrt{2\pi}\Delta T_\sigma} exp[-\frac{1}{2}(\frac{\Delta T - \Delta T_{mean}}{\Delta T_\sigma})^2]. \tag{5.20}$$

where n_{max} is the maximum nucleation density, ΔT_σ is the standard deviation (assumed to be $0.1K$ in this work) for the undercooling rate, and ΔT_{mean} is the mean undercooling rate. The critical nucleation probability can be determined from the following Figure 5.2.

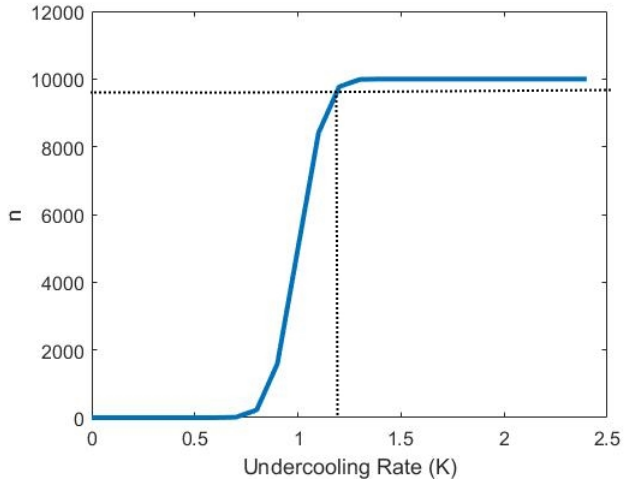

Figure 5.2: Nucleation probability density function for $n = 10^4$,$DeltaT_\sigma = 0.1K$, and $\Delta T_{mean} = 1K$.

5.2.1 Numerical Solution Algorithm

The solution of the defined governing equations as well as CA rules are calculated iteratively as follows:

1. Initialize the system for the domain size, cell size, initial temperature field, initial concentration field, and seed information

2. Scan the local growth velocity for the entire domain and identify V_{max}, calculate time step Δt via Eqn. (5.16)

3. Solve the discretized solute diffusion system and identify the C_e field with Eqn. (5.7)

4. Solve the discretized thermal field and identify the temperature field with Eqn. (5.1)

5. Calculate the interface curvature and anisotropy term with Eqn. (5.11) and (5.12)

6. Calculate the equilibrium interface concentration C_l^* from the interface temperature with Eqn. (5.8)

7. Determine the increase of local solid fraction Δf_s with Eqn. (5.9)

8. Calculate the growth velocity V with Eqn. (5.16)

9. Apply the update conditions for interface and solid cells with Eqn. (5.14) and (5.15): (1) For interface cells, release the latent heat and update corresponding temperature field; accumulate the rejected solute within Δt and update corresponding concentration field; (2) For solid cells, the rejected solute within Δt is pushed towards neighboring interface or liquid cells equally to ensure mass balance, update the corresponding solute concentration field

10. Calculate solid composition for interface cells with Eqn. (5.10)

11. Update current solid fraction f_s

12. Capture the neighbors and define the new interface cells

13. Repeat from step 2

5.2.2 Results and discussion

At the beginning of the simulation, a single row of seed is placed on the top-right half of the domain and to be used as initial nucleation sites. The melt is imposed with a constant heat flux removed from the top boundary.

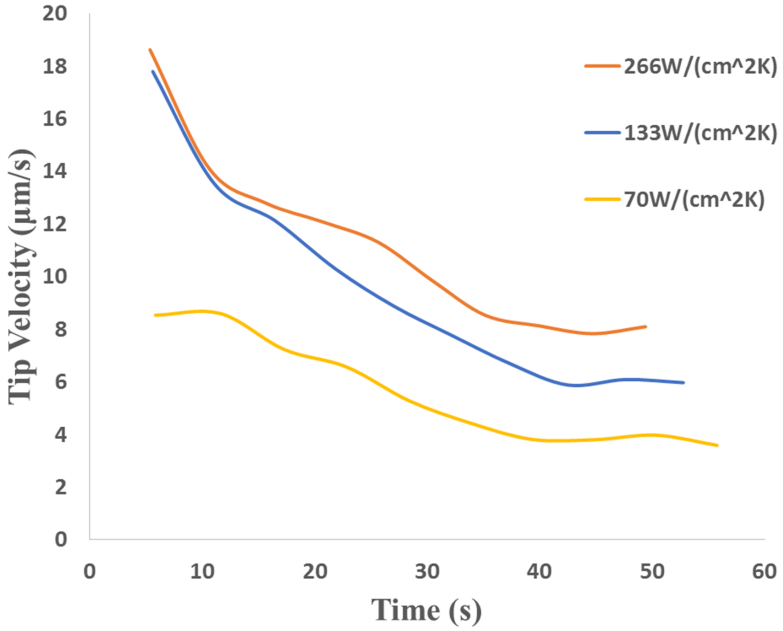

Figure 5.3: Tip Velocity as a function of time for different cooling conditions.

Figure 5.3 shows the simulated tip velocity profile as time proceeds, and the interface moves from zero to around 300 μm. An initial rapid growth is observed for all heat removal rates, and the tip velocities then fall into a relatively steady region; while faster heat removal rate always result in higher tip velocities.

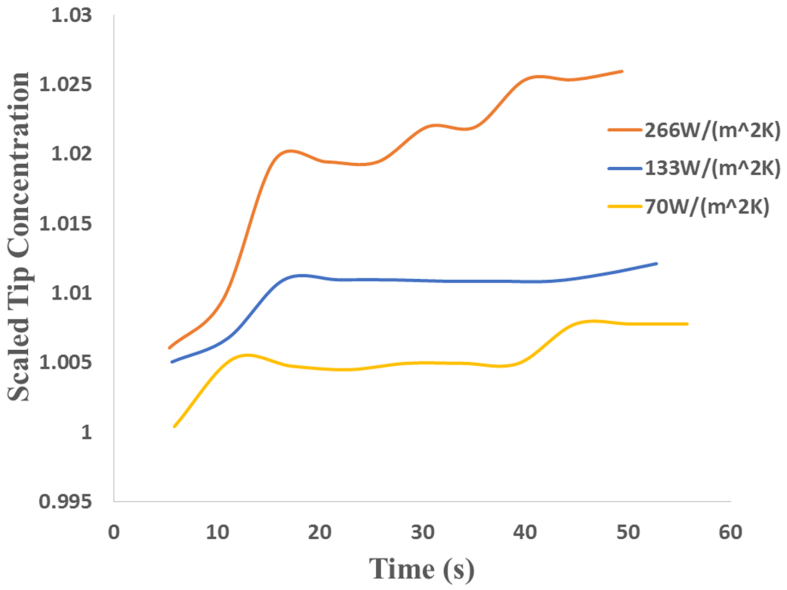

Figure 5.4: Tip concentration as a function of time for different cooling conditions.

Fast interfacial velocities have a strong impact on the segregation of impurities in the melt and distribution in the resulting wafers. As shown in Figure 5.4, higher impurity level can be observed at high interfacial velocity.

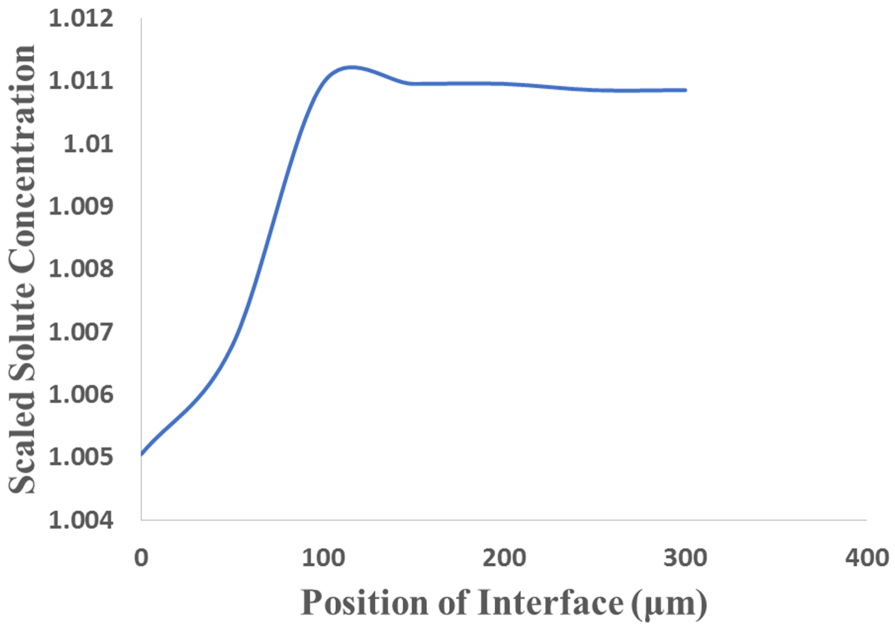

Figure 5.5: Distribution of solute in the wafer (mild cooling rate).

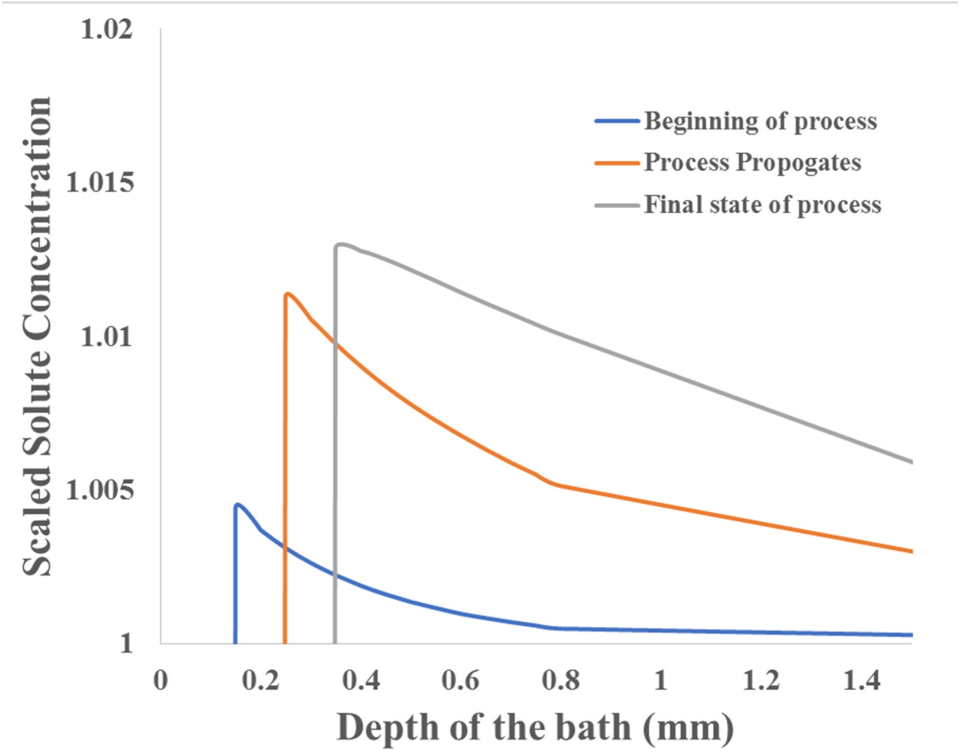

Figure 5.6: Impurity concentration profiles in the melt at different stages of the crystallization.

Figure 5.5 shows the solute distribution across the wafer. We can learn that the initial rapid growth tend to quickly trap the impurities at the top portion of the wafer, and then nearly constant composition in the lower portion of the crystal can be observed. Consequently, as indicated by Figure 5.6, an increase in the impurity concentration can be observed in the melt at the initial stage, where the vertical lines represent for the interface. And the boundary layer becomes broader as time proceeds, which indicates the diffusion of solute in front of the interface.

As shown in Fig. 5.8, 5.7 and 5.9, we can observe the formation of a wafer with sharp wedge (approximately 55°) and unstable interface, as seen in Varian's experiments in Figure 2.7. Sensitivity analysis is performed for different cooling rates. When a more aggressive cooling condition is applied, the interface is prone to dendritic growth. We also note that the average

local curvature approximation used leads to a mesh dependent dendrites in the current analysis.

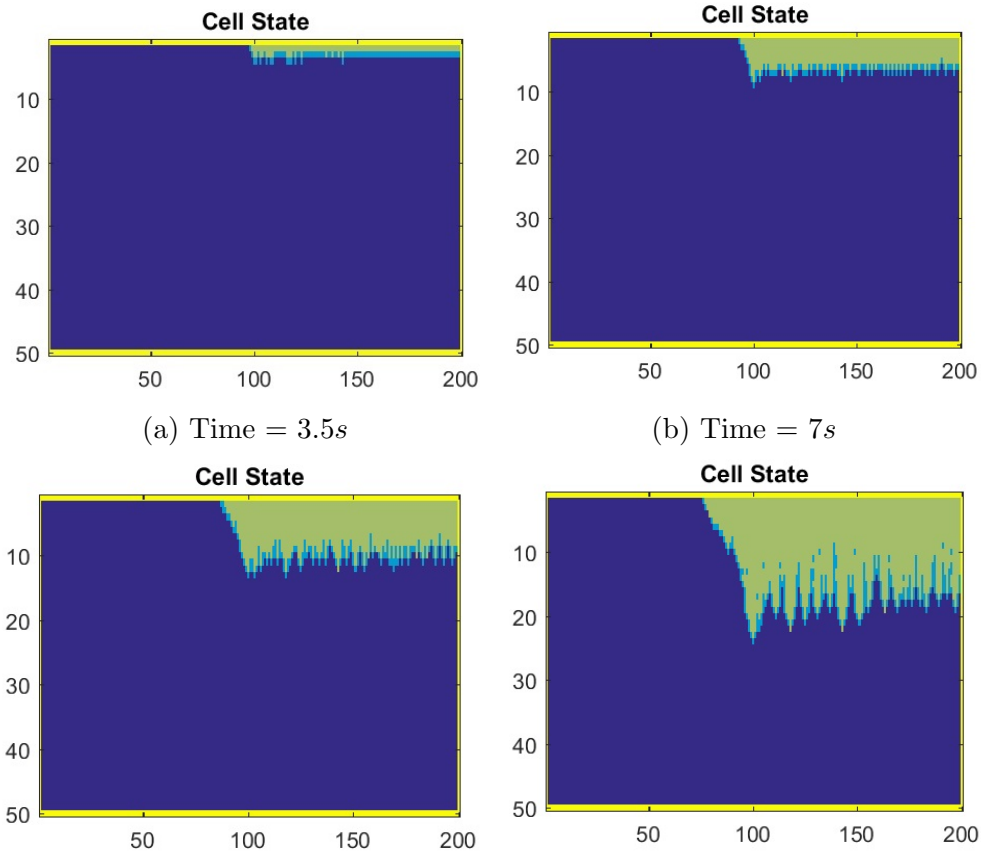

(a) Time = $3.5s$ (b) Time = $7s$

(c) Time = $10.5s$ (d) Time = $17.5s$

Figure 5.7: Cell States evolution with high level impurities (7% aluminum), mesh size $50\mu m$, high cooling rate, and single row seed.

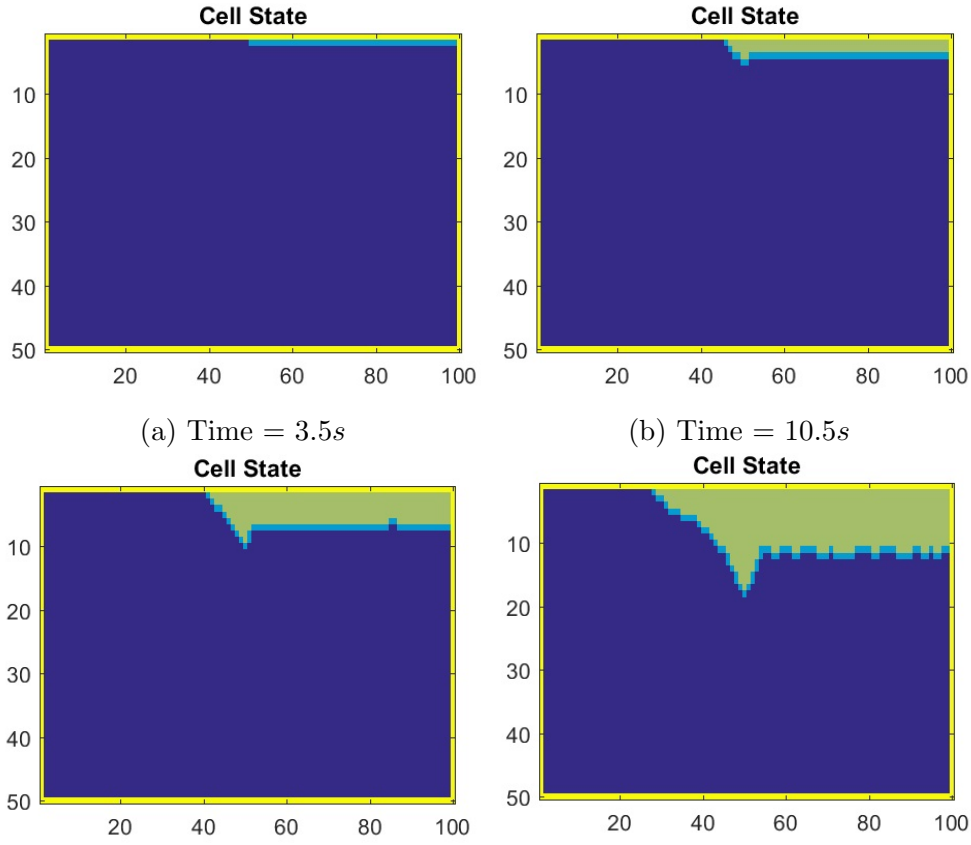

(a) Time = $3.5s$

(b) Time = $10.5s$

(c) Time = $21s$

(d) Time = $42s$

Figure 5.8: Cell States evolution with high level impurities (7% aluminum), mesh size $50\mu m$, mild cooling rate, and single row seed.

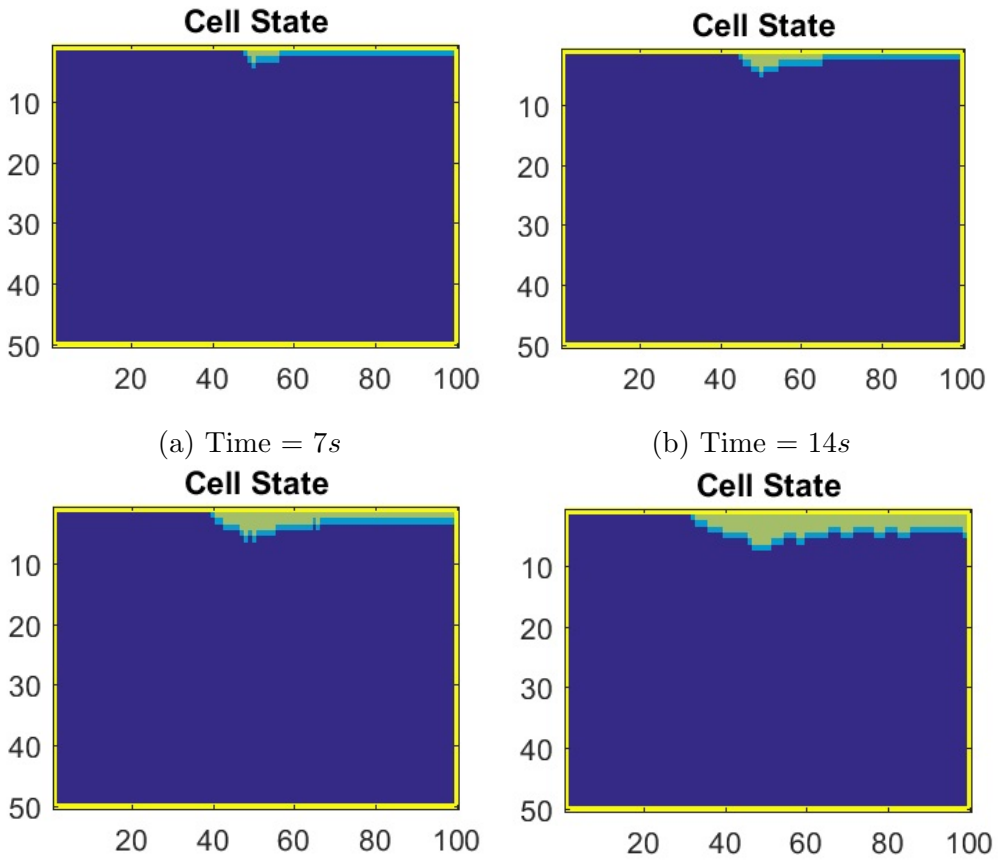

(a) Time = $7s$

(b) Time = $14s$

(c) Time = $28s$

(d) Time = $49s$

Figure 5.9: Cell States evolution with high level impurities (7% aluminum), mesh size $50\mu m$, low cooling rate, and single row seed.

To demonstrate the capability of the model, we performed the simulation of a single dendritic growth for the static condition. A square mesh with $5\mu m$ is used with a $50 * 100$ cells domain size. The preferential growth orientation is set to be 0° with respect to the horizontal direction. Figure 5.10 shows the simulated evolution of the dendritic morphology of a Si-7%Al with constant undercooling rates of $2K$ and $5K$. We can see that under a static diffusion case, the dendrite shape is symmetric. And the dendrite arm at $5K$ undercooling is thicker than that of the $2K$ undercooling.

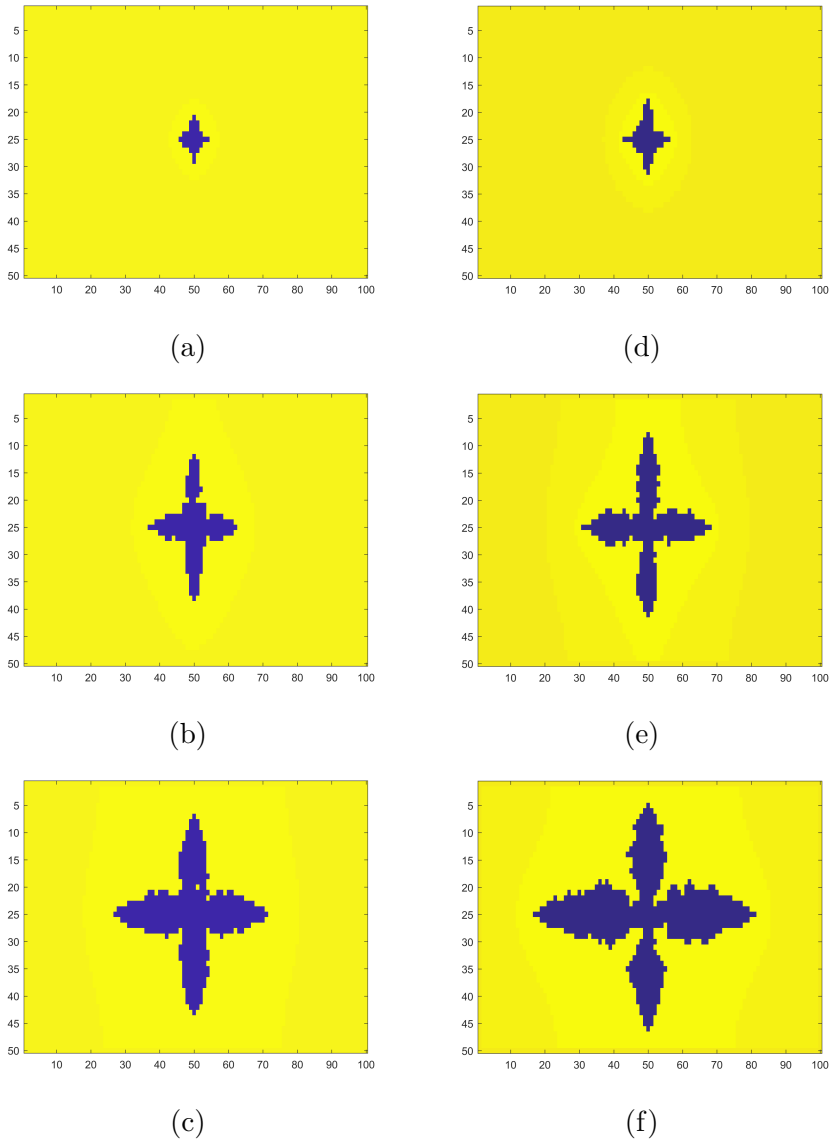

Figure 5.10: Simulated evolution of a single dendritic growth of Si-7%Al in a static melt. (a)-(c)$\Delta T_T = 2K$, after $1.667s$, $2.62s$, and $5.3s$, respectively; (d)-(f)$\Delta T_T = 5K$, after $1.667s$, 2.62, and $5.3s$, respectively

5.3 Kinetic Controlled Growth

Helenbrook et al. [22] conducted the first numerical analysis considering the kinetics effects for the HRG process and we are applying the same model in this analysis. We consider the case that the interface propagates according

to the kinetic solidification model developed by Weinstein and Brandon [53]. Three mechanisms including 2D nucleation, step propagation, and roughened growth are considered. The normal growth velocity V is defined as a function of undercooling rate ΔT and kinetic coefficient β. Undercooling ΔT is obtained by the following function Eqn. (5.22).

$$V = \beta \Delta T(t_n), \tag{5.21}$$

$$\Delta T = \Delta T_T + \Delta T_C + \Delta T_R \tag{5.22}$$

where ΔT_T,ΔT_C, and ΔT_R are thermal undercooling, solutal undercooling, and curvature effects, respectively. We assume that the thermal undercooling ΔT_T is constant, while solutal and curvature effects depend on the local impurity composition C_l, curvature K, and anisotropy f. In order to take care of the artificial anisotropy term introduced by the square CA mesh, the following Eqn. (5.23) for calculation of interface curvature can be adopted [3]. The equation is solved using second order centered finite difference scheme.

$$K = [(\frac{\partial f_s}{\partial x})^2 + (\frac{\partial f_s}{\partial y})^2]^{-3/2}[2\frac{\partial f_s}{\partial x}\frac{\partial f_s}{\partial y}\frac{\partial^2 f_s}{\partial x \partial y} - (\frac{\partial f_s}{\partial x})^2\frac{\partial^2 f_s}{\partial y^2} - (\frac{\partial f_s}{\partial y})^2\frac{\partial^2 f_s}{\partial x^2}]. \tag{5.23}$$

The accuracy of this method is demonstrated by Figure 5.11, where a sensitivity analysis is performed to show the steady-state tip velocity as a function of mesh size for the system with 50ppm aluminum and undercooling of 5K. When the mesh size is reduced, the steady state velocity converges.

The local growth angle φ can be determined using the same method presented by the previously defined eqn. (5.13). Anisotropy can be determined by eqn. (5.12). Eqn. (5.24) - (5.26) defines the kinetic coefficient β, and are

obtained from [53].

$$\beta = min(\beta_{rough}, max(\beta_{2DN}, \beta_{step})), \tag{5.24}$$

where β_{rough} defines the roughened growth and set to be $1.26m/sK$.

$$\beta_{2DN} = \frac{1}{B} exp(\frac{A}{\Delta T}). \tag{5.25}$$

$$\beta_{step} = \beta_{st}|sin(\theta_0)|, \tag{5.26}$$

where β_{2DN} describes the 2D nucleation effect, $A = 140K$, and $B = 1.5 \cdot 10^{10} m/(sK)$. $\beta_{st} = 0.63m/sK$ and θ_0 is a misalignment angle.

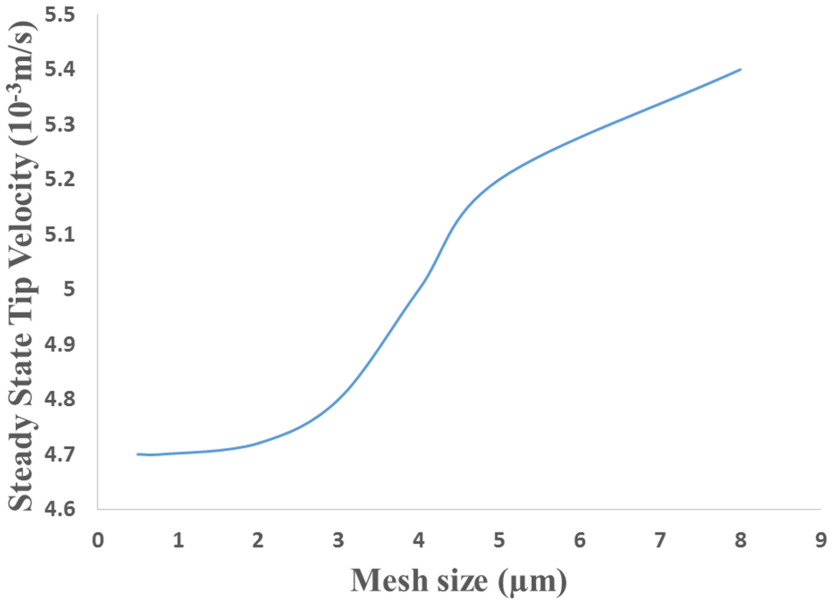

Figure 5.11: Steady-state Tip Velocity as a function of mesh size.

Figure 5.12 shows the kinetic coefficient β as a function of undercooling rate and misalighment angle. At the sharp wedge location, [21] shows an undercooling rate of $2-4$K in front of the formed facet, while the misalignment angle is small in this region.

The increase of solid fraction at each time step is given by the following

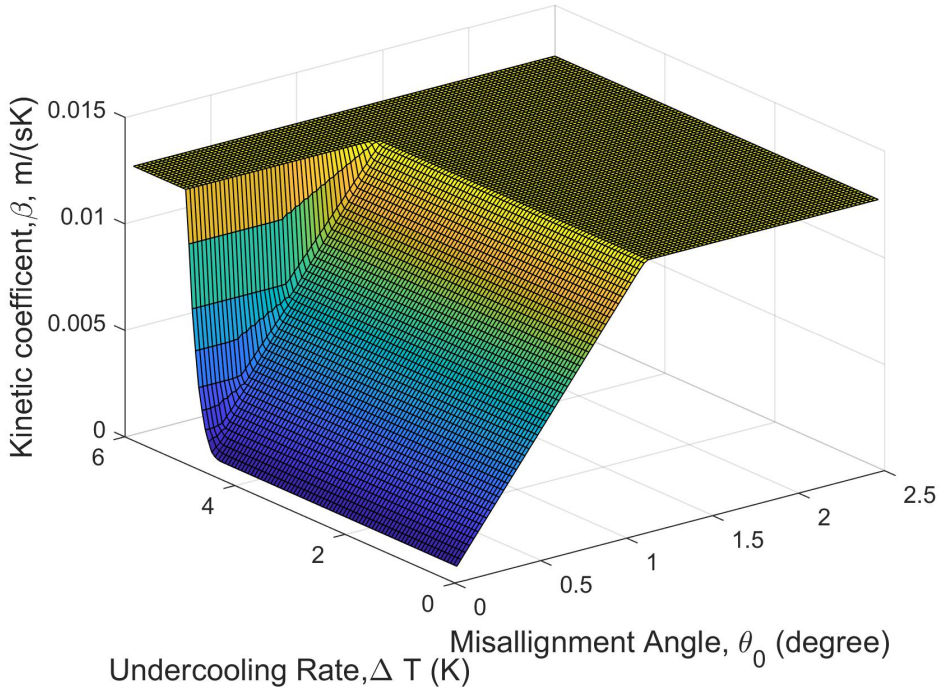

Figure 5.12: Kinetic Coefficient β as a function of undercooling rate and misalignment angle.

equation:

$$\Delta f_s = G\frac{V}{d}dt, \tag{5.27}$$

where G is a geometrical factor that captures the states and distance effects of the neighboring cells. G is defined in the following equations:

$$G = 0.4(\sum_{n=1}^{4} s_n^{1st} + \frac{1}{\sqrt{2}}\sum_{n=1}^{4} s_n^{2nd}). \tag{5.28}$$

Eqn. 5.27 and 5.28 are adapted from [57]. s_n can be determined by the state of the neighboring cell (0 for non-solid cells and 1 for solid cells), where the superscript indicate the distance of the neighbor cell. The local solid fraction can be updated every time step until it reaches 1, then the cell is transformed

from interface to solid. The time step used for each iteration is given by:

$$dt = \min(\frac{1}{5}\frac{1}{max(\Delta f_s)}, \frac{1}{5}\frac{d^2}{D_l}). \tag{5.29}$$

5.3.1 Numerical Solution Algorithm

For the case that kinetics is considered, the numerical solution is obtained in a similar fashion compared with the previous defined algorithm. The major difference is we adopt a different way to decide the interface growth velocity, and a constant thermal undercooling rate is assumed to simplify the calculation. Detailed algorithm is as follows.

1. Initialize the system for the domain size, cell size, initial temperature field, initial concentration field, and seed information
2. Scan the entire domain and identify $max(\Delta f_s)$, determine the time step dt with Eqn. (5.29)
3. Solve the discretized solute diffusion system and identify the C_e field with Eqn. (5.7)
4. Calculate the interface curvature and anisotropy term with Eqn. (5.23) and (5.12)
5. Obtain the local undercooling rate with Eqn. (5.22)
6. Estimate the kinetic coefficients and calculate the growth velocity V
7. Determine the increase of local solid fraction Δf_s with Eqn. (5.27)
8. Apply the update conditions for interface and solid cells with Eqn. (5.14) and (5.15)
9. Calculate solid composition for interface cells with Eqn. (5.10)

10. Update current solid fraction f_s

11. Capture the neighbors and define the new interface cells

12. Repeat from step 2

5.3.2 Results and discussion

We also take a closer look at the sharp wedge location, where we consider an initial melt composition of $50ppm$, and a constant thermal undercooling rate. A detailed thermal profile is not calculated in this case. At the beginning of the simulation, a single row of seed is placed in the domain to initiate the crystallization. We performed a sensitivity analysis for different undercooling rates.

Figure 5.13 shows the concentration profile in the solid and melt region, where the solid composition for $\Delta T_T = 5K$ is slightly higher than for $\Delta T_T = 2K$. At the interface, both cases show a sudden increase and decay exponentially until it reaches the initial melt composition ($50ppm$). The composition decays in a steeper fashion for high undercooling case, as higher undercooling rate results in higher growth rate, thus solute rejected in front of the interface has less time to diffuse away.

Figure 5.14a and 5.14b shows the steady-state tip parameters with different undercooling rates.

5.4 Conclusion and Contribution

We presented a computational modeling algorithm combining cellular automaton with finite difference model to simulate the progression in crystal growth within the HRG process. In the present model, thermal and solutal macro-

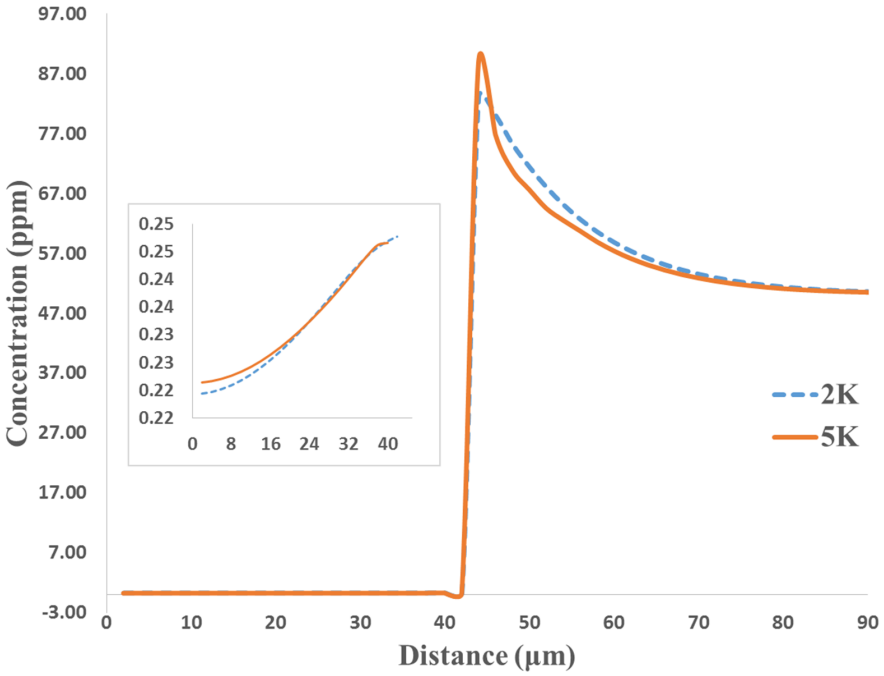

Figure 5.13: Concentration Profiles for different undercooling rate. Insets denote the concentration profile in the solid region.

scopic field models are considered for numerically calculating the heat transfer and mass transfer governed by diffusion, while convection is neglected. The model includes both solutal and curvature contributions for undercooling. Two different cases are considered: For diffusion controlled growth, we focus on the larger scale level to investigate the overall sharp wedge formation. A sensitivity analysis is conducted under different cooling conditions, and an unstable interface front is identified. The solute distribution evolution shows that for the current system a relative homogeneous impurity level can be observed in the bottom portion of the wafer. For kinetic driven growth, the system is simulated under constant thermal undercooling rate. The findings in this chapter can serve as a starting point investigating further kinetic interactions at smaller scale level of the HRG process, and hence to obtain their micro scale phenomena with macro-scale coupled parameters. We also note that convection is not included in the current model while the facet growth can be

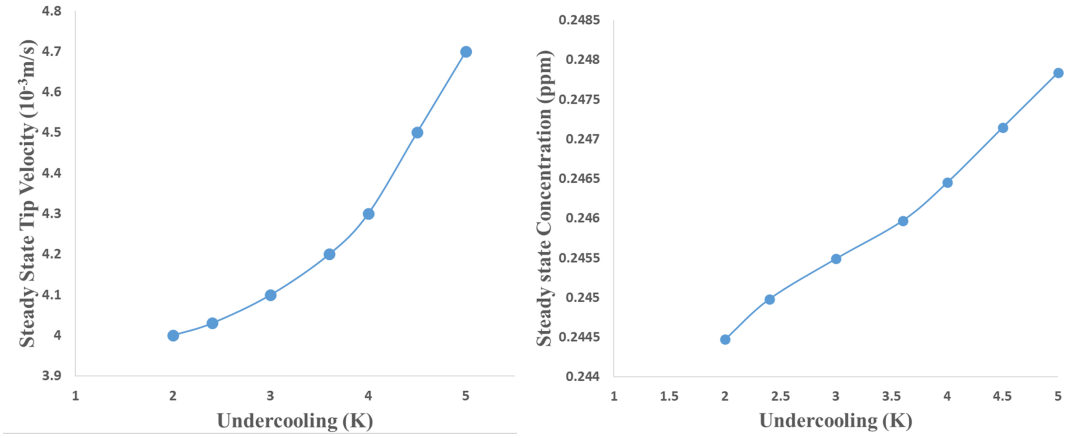

(a) (b)

Figure 5.14: Comparison of steady-state tip parameters with different undercooling rate for Silicon melt with 50 ppm aluminum. (a)refers to steady-state tip velocity; (b) refers to steady-state tip composition.

significantly affected by local convection.

Chapter 6

Process design and experimental verification

6.1 Silicon HRG Experiment

The silicon HRG machine in the Rothfus Lab in Doherty Hall is designed to validate our theoretical findings and ultimately to achieve stable production for mono-crystalline silicon wafer. This is a major task, and several outputs of the system and its operation are presently not developed to a point where a wafer can be produced. The subgoals in this work are broken down into the following sub-objectives:

1. Crucible design.
2. Extraction and seeding apparatus design.
3. Insulation design.
4. Continuous wafer production.
5. Process stability and optimization.

We performed several melt trials to finalize the standard operation procedure (SOP) that includes pre-experiment preparation, melting process, and cooling down process. A stable, reliable, and reproducible melting process has been achieved using the current design. The current SOP and typical process operating errors are summarized in the appendix section for future experimental design reference. Nevertheless, substantial progress has been achieved.

6.2 Crucible Design

In order to achieve the first and second sub-objectives, we performed several melt trials using different crucible designs. Based on the experimental results and performance, a number of operational problems have been identified, and modifications and improvements have been made to fulfill process requirements. As shown in Figure 6.1, a graphite crucible with a partially covered lid was used for the melt trial. We can conclude that there is significant amount of radiative heat loss through the top surface, thus, any uncovered section will not melt successfully. The design shown in Figure 6.2 has a fully covered lid with a rotational door cover to reduce the heat loss during the melting process. A triangular shape edge is used to support the seeding and allow contact between the seed and silicon meniscus. The height of exit is estimated based on weight-volume ratio before and after the melt trial. Adjustments need to be made if different type of raw material is used in the future. Successful melt trials have been achieved with this crucible design. However, several potential problems have been identified and need to be resolved. First of all, the induction coil being used as heating source for the feed occupies too much space. This limits the crucible size as available space is restricted. Furthermore, two positions (front and back) are required for the cover lid to fulfill the flexibility

feature of the system: (1) the lid has to fully cover the melt surface at front position (2) additional support is needed to sustain the cover at back position within available space.

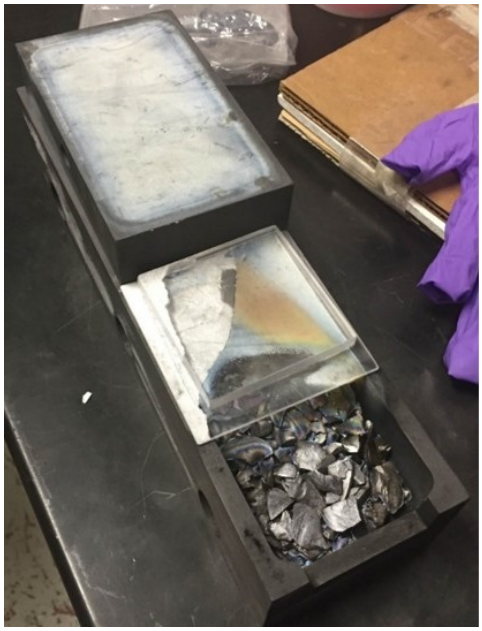

(a)

(b)

Figure 6.1: Melt trial conducted using graphite crucible with partially covered lid.

(a)

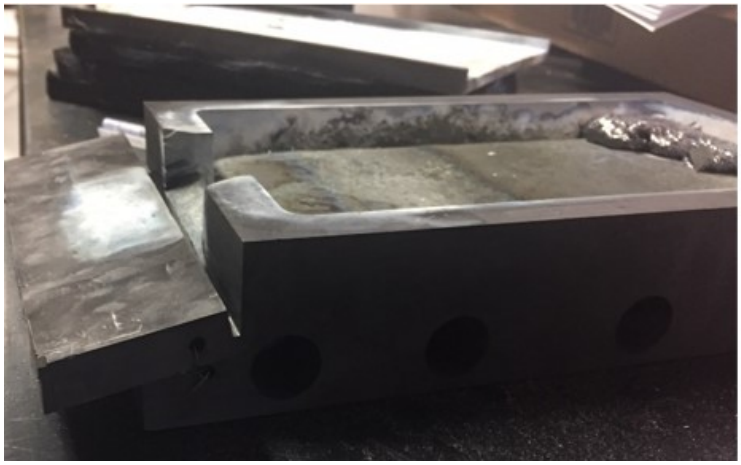

(b)

Figure 6.2: Melt trial conducted using graphite crucible with fully covered lid, flexible door, and machined exit design.

We performed melt trials using crucible made of graphite and quartz to get an estimate on the potential impurity levels in the process. As shown in the Fig. 6.3, the impurity level for the graphite crucible is high. Several types

of impurities are introduced or produced during the melting process, such as silicon carbide and silicon oxide; while the impurity level for the quartz crucible is considerably lower. We conclude that the current graphite crucible needs to be coated with other material, such as CVD deposited SiC, or be replaced by other material for the future experiments. We also noticed considerably high amount of impurity introduced by the current insulation design, which is based on graphite felt.

(a)

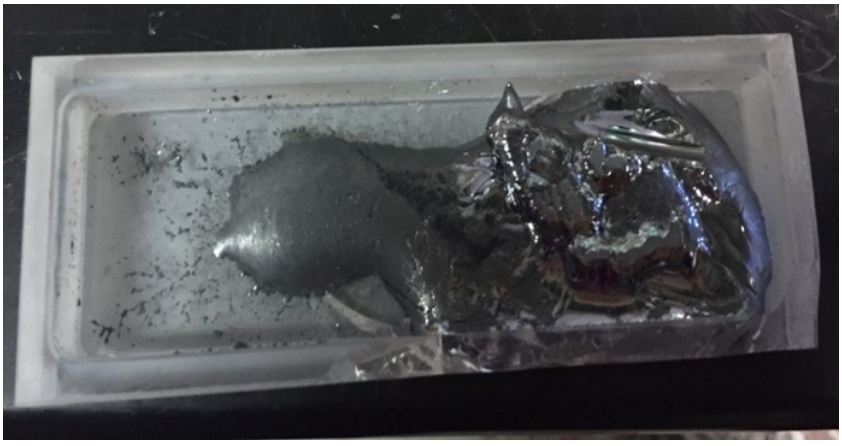

(b)

Figure 6.3: Melt trial conducted using (a) graphite crucible and (b) quartz crucible.

Based on our melt trails, we constructed the new crucible design, as shown in Fig. 6.4.

The new crucible is constructed by three separate parts: a door, lid, and the main crucible. A rotational door prevents heat loss during the melt process (shown in Fig. 6.4b) while allowing access during the seeding and extraction processes (shown in Fig. 6.4d). An arc shaped hollow bottom allows free rotation of the door supported by a molybdenum wire. The collection tray gathers any spill (shown in Fig. 6.4b). The height of the rotational door is greater than the length of the collection tray so that the door sits on top of the collection tray during the seeding/extraction processes, and in this way works as an intermediate support.

The current design utilizes only half length of crucible to contain silicon melt, while the back half is working as support for the lid when it is moved back to allow the top of the melt to cool (illustrated in Fig. 6.4a, 6.4e, and 6.4g). Temperature measurements are obtained via multiple thermocouples installed in the system. Figure 6.5 shows the temperature plateau at around $1425°C$ from the lower left thermocouple. This temperature represents the crucible temperature close to the exit. The melting temperature of silicon is $1414°C$ so the temperature off-set is $9°C$. This temperature plateau indicates the melting process of silicon, which can be used as a key identification criteria when limited temperature information is available for a melting process. One can also estimate the efficiency of heating process from this information: the energy needed for melting 800 g silicon is calculated as $1790 \cdot 10^3 \frac{\mathrm{J}}{\mathrm{kg}} \cdot 0.8\mathrm{kg} = 1.432 \cdot 10^6\mathrm{J}$; total energy consumed in 2 min is calculated as $40 \cdot 10^3 \frac{\mathrm{J}}{\mathrm{s}} \cdot 120\mathrm{s} = 4.8 \cdot 10^6\mathrm{J}$. The overall efficiency is around 30%.

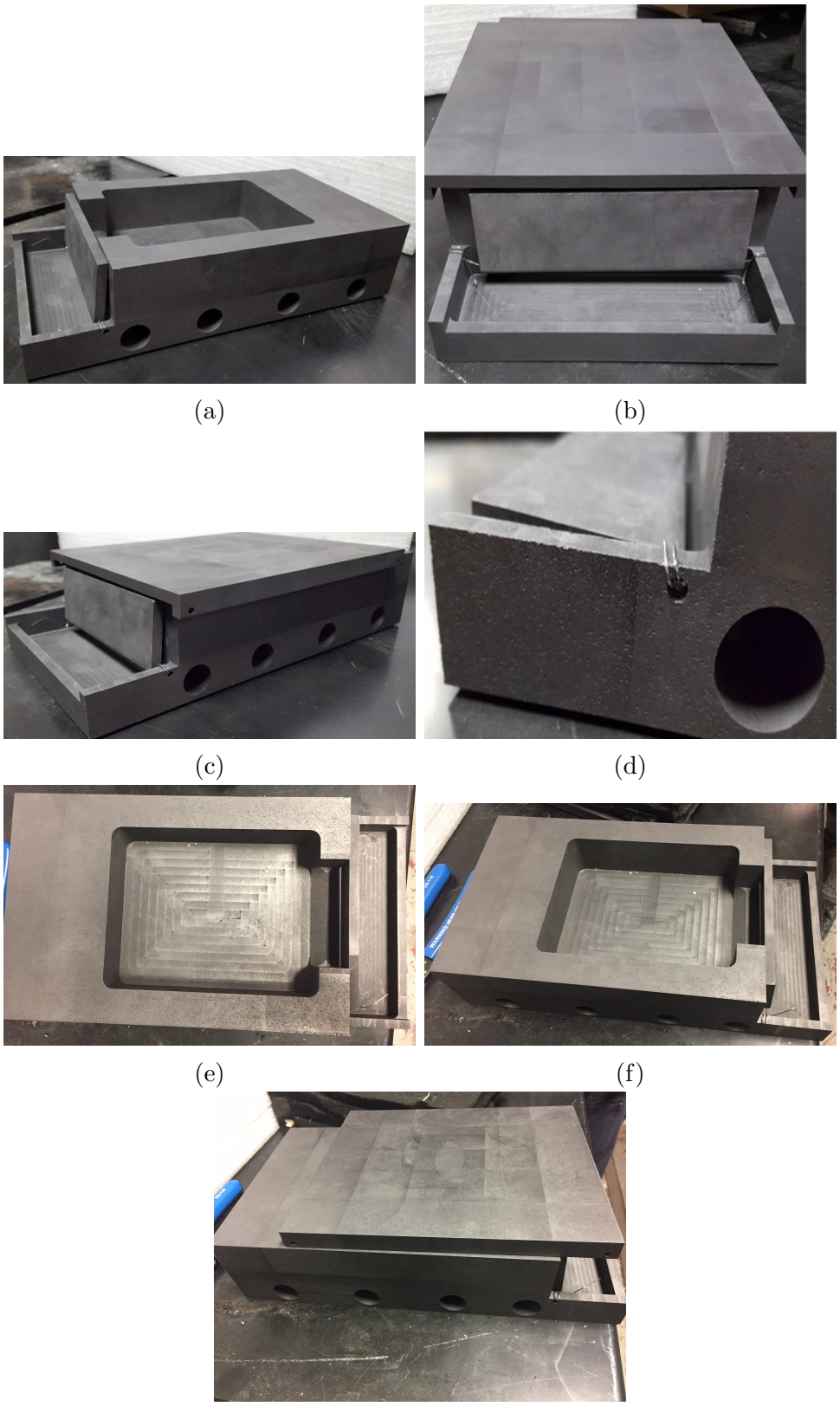

(a) (b) (c) (d) (e) (f) (g)

Figure 6.4: Updated version Graphite crucible Design.

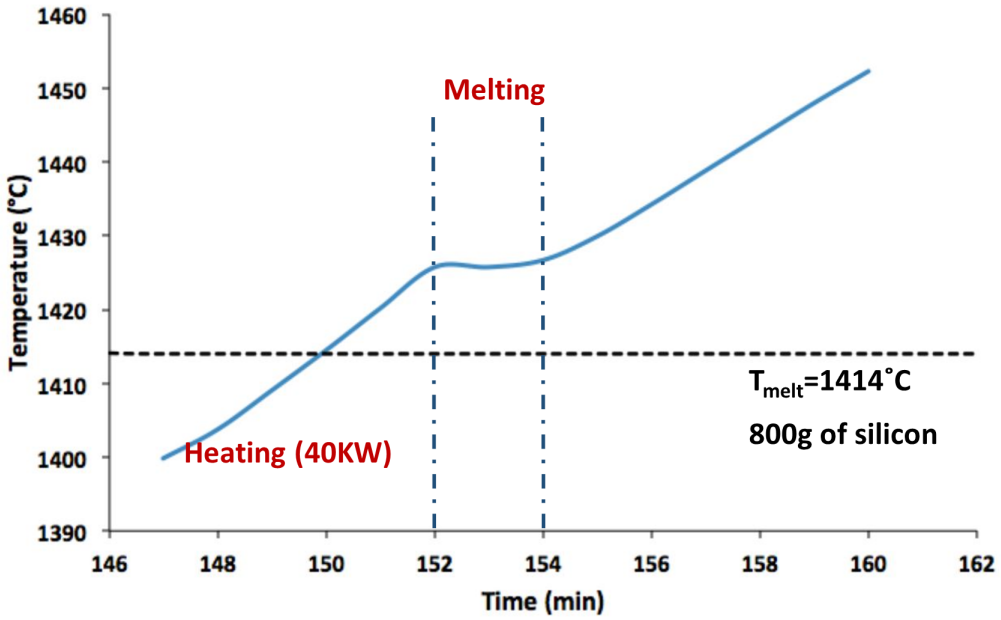

Figure 6.5: Temperature Plateau during constant heating ($40KW$) indicating melting process.

6.3 Seed attachment Design

In order to initiate the crystal growth, a seed must be inserted to the crucible and make contact with the melt. The seed we are using is a square shape thin mono-crystalline silicon wafer. The seed wafer is attached either chemically (with sauereisen and geocohesive high temperature ceramic glue) or mechanically to a short graphite strip to achieve enough length and strength for insertion and pulling.

We performed multiple melt trials testing two different adhesives that can theoretically withstand high temperature up to $1650°C$. The following Figures 6.6a and 6.6b illustrate the melt trial results for Gemcohesive and Sauereisen attached seed samples. The Gemcohesive attached seed separated from the graphite strip after the melt trial. The Sauereisen attached seed also shows weak attachment to the strip. Thus, in order to ensure strong attachment to

support the pulling, the author proposes to mechanically attach or seal the wafer seed to a metal strip. This was attempted in a few trials and it proved satisfactory.

(a) (b)

Figure 6.6: Melt trials for different adhesive samples. (a)Gemcohesive adhesive sample; (b)Sauereisen adhesive sample

6.4 Conclusions and Contributions

In this chapter, we discussed the experimental progress regarding the silicon HRG process development. We developed a reliable melting procedure to guarantee successful melting with limited temperature measurements information and limited observation port. Furthermore, we developed a new graphite crucible that fulfills current process requirement and avoid potential problems observed in previous designs. Although all preliminary experiments were conducted using graphite crucible, the author recommends testing other coating materials such as CVD deposited SiC to reduce the impurity levels before the pull trial. Preliminary seed attachment designs have been tested in high temperature melt trials. It has been found that a mechanical clip provides a good solution.

Chapter 7

Concluding Remarks

7.1 Thesis Summary

The objective for the research presented in this thesis is to advance the development of an advanced continuous ribbon growth approach for continuous production of mono-crystalline silicon sheets. The main application we have in mind is in the area of photovoltaics. But, such sheets can also find application in micro-electronics, flat panel display, microfluidics, and large scale switches. It is also possible that such a process can be used to produce sheets based on oxides, such as Al_2O_3 to produce sapphire sheets for phone, flat panel display, opotoelectronics and optical windows in harsh environments.

Continuous direct wafer process has the advantage of simplifying the supply chain of wafer process compared with traditional ingot based technologies. The idea behind HRG process was first outdated in 1950's by William Schockley. Since then significant amount of research analysis was conducted until 1970's. Research on HRG was almost completely suspended until renewed interest into solar energy took place around 2005. Varian Semiconductor obtained many patents and successfully produced silicon ribbons via a HRG type process.

Despite the theoretical and experimental research conducted in the past 50 years, there are still several challenges need to be throughly investigated before we can achieve reproducible, reliable, stable production in a cost competitive fashion via the HRG process. In this thesis, we assessed three main technical challenges of the HRG process via mathematical modeling approaches: Overall process modeling and preliminary control studies, corrugated wavy instability at the crystallization interface, and the problem of unstable sharp wedge formation at the leading edge of the crystal sheet. We also developed two HRG prototypes to assist us with experimental verification.

The overall process modeling objective is achieved by mathematical modeling the HRG process using a coupled 2-D heat transfer, phase change, and fluid flow system with an ice-water system for process verification. We applied mushy zone theory and Heaviside step change functions to simplify the numerical difficulties caused by the moving boundary and discontinuous nature of solidification. The model is implemented through COMSOL and solved using the finite element method. A steady state model was used to obtain correlation between pulling velocity and thickness of the produced wafer. The model was compared with experimental results. A good correspondence was found at high pulling rates. A dynamic model was developed for control studies. It was found that the HRG process is highly nonlinear and multiple steady states exist.

To address the second problem, we performed a linear stability analysis to investigate the effects of different driving forces in the system. The governing equations for the mass, energy, and momentum balances were developed. Base solutions were obtained with two sets of boundary conditions satisfying the crystallization condition at the liquid/solid interface and thermal boundary conditions that describe different process conditions. The nonlinear system

was then linearized and the profiles for thermal, solutal and flow fields with regard to small-amplitude normal mode perturbations of the base state were derived. We tested the effects of different operating conditions on the stability of the system. A direct integration method is used to derive a neutral stability curve which can quantify a range of stable operating conditions. It was found that ensuring sufficient heat removal and high wedge factors are beneficial for stabilization of the system.

To address the third problem, we developed a mathematical model to couple a cellular automaton for solidification and crystallization with the finite difference method to describe the temperature and concentration fields. The CA algorithm is based on local transition rules utilizing time-dependent cell parameters obtained from numerical solutions of the energy and species conservation equations obtained via finite difference methods. We considered both diffusion driven solidification and kinetics limited growth. Case studies for different conditions and transition rules are performed. It was found that a relative homogeneous impurity level can be achieved in the bottom portion of the wafer. The sharp wedge and unstable facet growth are identified in our simulation.

With regard to the experiments, we utilized the two experimental HRG setups to verify our theoretical findings and test the feasibility of the proposed process. These included operation of an ice-water system and a high temperature $60KW$ induction furnace system. We achieved stable and reliable ice wafer production using the current design described in Chapter 3. The correlation between pulling velocity and thickness of the wafer is verified. The updates of process development regarding the silicon system is presented. Specifically, we developed a reliable melting procedure and discussed potential process difficulties that need to be resolved.

7.2 Future Directions

7.2.1 Mathematical modeling of the cooling system and insulation

Detailed local mathematical models have been developed earlier by Daggolu et al. [14] that describes multiple local interactions and thermal profile of the HRG process. To continue with process design and better utilize the silicon HRG equipment we have at CMU, a mathematical model that quantifies the thermal profile between the furnace and crucible is needed. Such a model can guide us in process design. The cooling apparatus being implemented in the HRG processes developed by Kudo and Kellerman use an active gas cooling jet combined with passive radiative cooling. The cooling rate is usually adjusted by gas flow rate and direction. To enhance the overall control of temperature profile, two susceptors can be installed on the top of the crucible. The placement, distance, and orientation of such design should be investigated via a detailed thermal profile modeling. In addition, the insulation and extraction design should be verified with detailed heat loss analysis, especially for the growth section.

7.2.2 Thickness control, process stabilization, and production optimization

One of the challenges currently encountered is to control the thickness of produced wafer. This can be achieved by applying control development in two process sections, as illustrated in Figure 7.1a. The figure shows four independent process sections are used in the HRG process. The thickness control is achieved in the growth and thickness control sections. Specifically, control

strategies can be applied to align with detailed modeling of the crystal growth dynamics, including heat transfer, crystal growth, solute distribution, and kinetic conditions. Additional thickness control can be applied to (1) reduce the thickness; (2) even out any non-smooth or non-homogeneous interface, as shown in Fig. 7.1e. The thickness control problem can be addressed as a 2D Stefan control problem.

Current experimental results also poses further challenges between the production speed and stability of the system. In particular, at high wafer extraction speed, the crystal front becomes unstable and dendrite start to form. This problem can be addressed by continuing the investigation on our micro-level modeling to look at the kinetics of the crystal front. The model proposed in this thesis is mainly deterministic based theory. However, due to limited experimental results and knowledges on available kinetics for the HRG process, further stochastic theories should be investigated.

The stability of the system under different operating conditions should be tested utilizing CA coupled techniques, or Monte Carlo type Methods. In addition to the physical understanding of the system, unknown disturbances can be compensated by the development of advanced control strategies.

7.2.3 Experimental Development

The water-ice HRG system shows that it is possible to produce a thin ice wafer with dimension similar to those required in PV application. Stable, reliable, and repeatable production at high speed has been achieved.

We developed a standard melting procedure for the silicon HRG to achieve reliable melting from silicon chips supplied by Hemlock Semiconductor at Midland, MI. The next step would be to develop an extraction apparatus to facilitate the automatic seeding and wafer extraction. This can be achieved by

the following sub-objectives:

1. Seeding and extraction angle control
2. Intermediate support
3. Temperature maintenance
4. Machinery and parts development

The first issue has been addressed in the water-ice HRG system where different pulling angles were tested in the experiments to ensure the meniscus stability. The angle control is achieved by adjusting the relative height of pulling system with respect to the melt level.

The second problem becomes important for the silicon system since the scale level significantly increased, where the gap between the crucible and puller needs to be taken care of. This intermediate support can also be used to adjust the seeding and pulling angle.

In the extraction section, temperature maintenance and dynamic control is needed as high thermal stress is crucial for the quality of produced wafer. It should be noted that control may be non-trivial since the brief study in Appendix F shows that the HRG system may have multiple steady states.

Other minor design problems also remain to be addressed such as detailed susceptor design for heat flow adjustment, material replenishment design to ensure continuous production, puller design that can avoid contamination for produced wafers. The latter is especially important since the main instability are due to impurities. The entire automated system design together with supporting control system wiring is needed. Detailed thermal profile modeling is needed for the machinery and parts development.

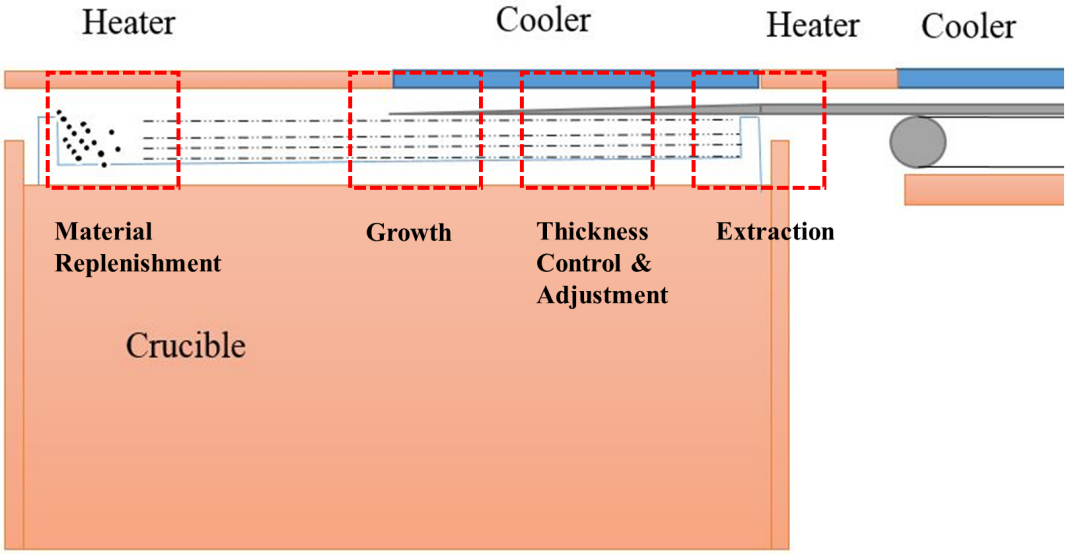

(a) Schematic of the HRG Experimental Configuration.

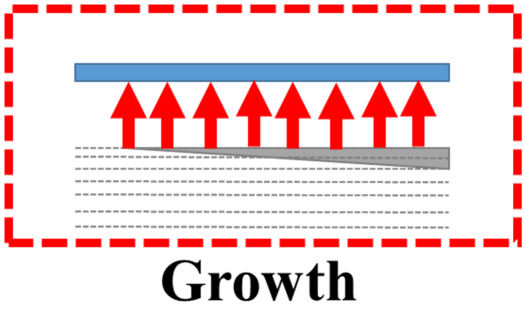

(b) Growth section.

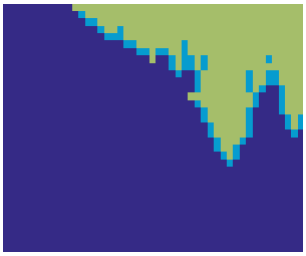

(c) Simulated silicon wafer shows sharp wedge and high thickness.

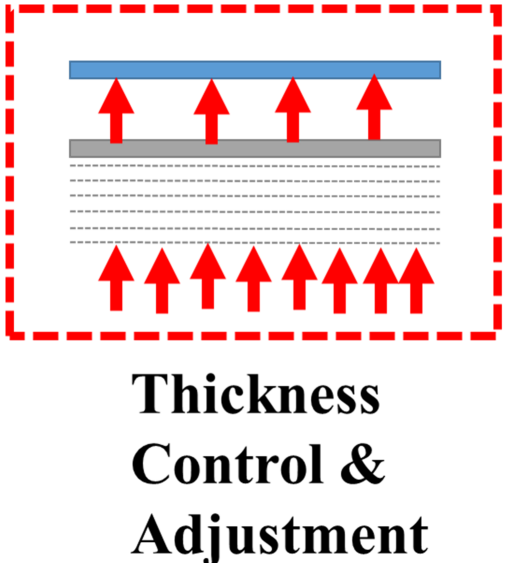

(d) HRG Thickness Control & Adjustment Section.

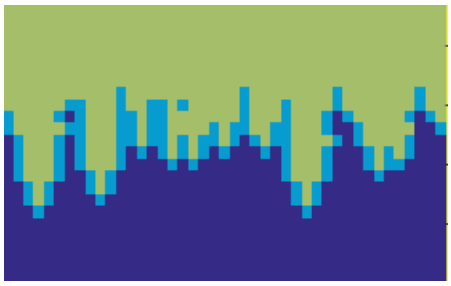

(e) Simulated silicon wafer shows high thickness and Non-smooth Interface.

Appendix A

Validity of neglecting velocity terms for the ice-water system

Previously defined equation 3.1 can be written as:

$$k_s(\frac{\partial^2 T}{\partial x^2} + \frac{\partial^2 T}{\partial y^2}) = \rho C_p u \frac{\partial T}{\partial x}. \tag{A.1}$$

Integrating over the total length and thickness of the solid region, we arrive at the validity condition:

$$k_s(G_x + G_y) \gg \rho C_p u \Delta T(l, 0), \tag{A.2}$$

where $\Delta T(l, 0) = G_x l = G_y t$. So that the horizontal velocity term in the solid region can be neglected if the conducted heat is much greater than the change in the sensible heat. And we can arrive at the following condition:

$$u \ll \frac{k_s}{\rho C_p t} \tag{A.3}$$

For ice wafer with a thickness of $200\mu m$, u should be less than 357mm/min.

Appendix B

Heat transfer coefficient estimation for ice-water system

We assume the temperature of ice-water surface to be 270K and the cooling air temperature is 200K. G_r number can be calculated by $G_r = \frac{L^3\rho^3 g\beta\Delta T}{\mu^2}$. Other parameters used for the estimation is summarized in the following table:

Table B.1: Material Properties and Parameters used for the estimation

Parameter	Value
ρ_{air}(density of air)	$1.76\frac{kg}{m^3}$
g (gravitational constant)	$9.806 m/s^2$
β (thermal expansion coefficient)	$0.00425 K^{-1}$
μ (viscosity of air)	$1.622 \cdot 10^{-5} kg/m \cdot s$
Gr	$2.76 \cdot 10^8$
Pr(for air at around $-100°C$)	0.73

Thus, the heat transfer coefficient can be estimated by $h_{air} = 1.52\Delta T^{1/3} = 6.3 W/m^2 \cdot K$

Appendix C

Eigenvalue Convergence

The convergence of eigenvalue problem solved as a function of number of nodes used for C_∞=50ppm, V_p=50 mm/min, W=300, G_l=200 K/cm, k=5 is shown in the following figure.

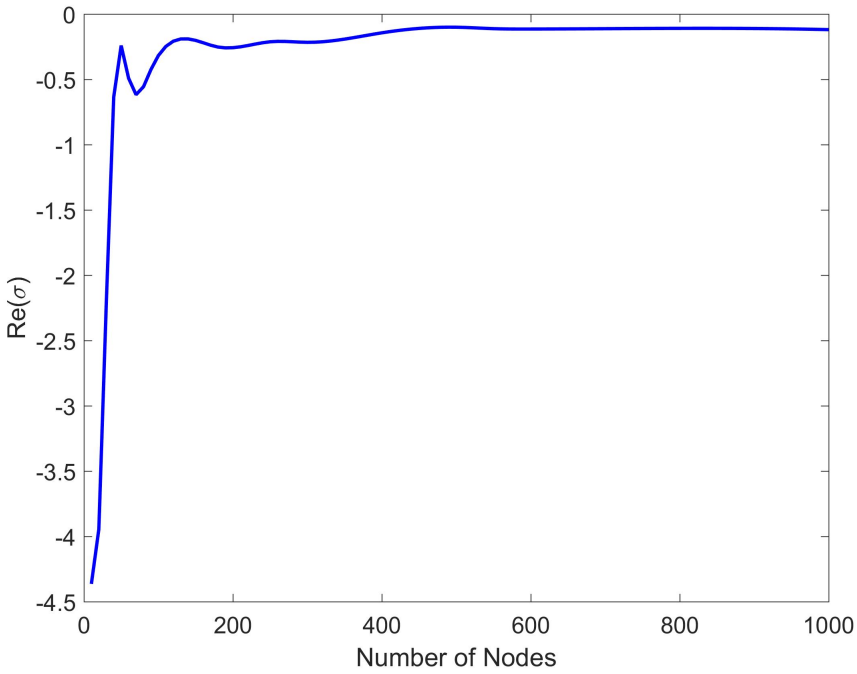

Figure C.1: Eigenvalue for C_∞=50ppm, V_p=50 mm/min, W=300, G_l=200 K/cm, k=5

Appendix D

Silicon HRG system Experiment

Current Crucible Design

Figure D.1: Graphite Lid Design

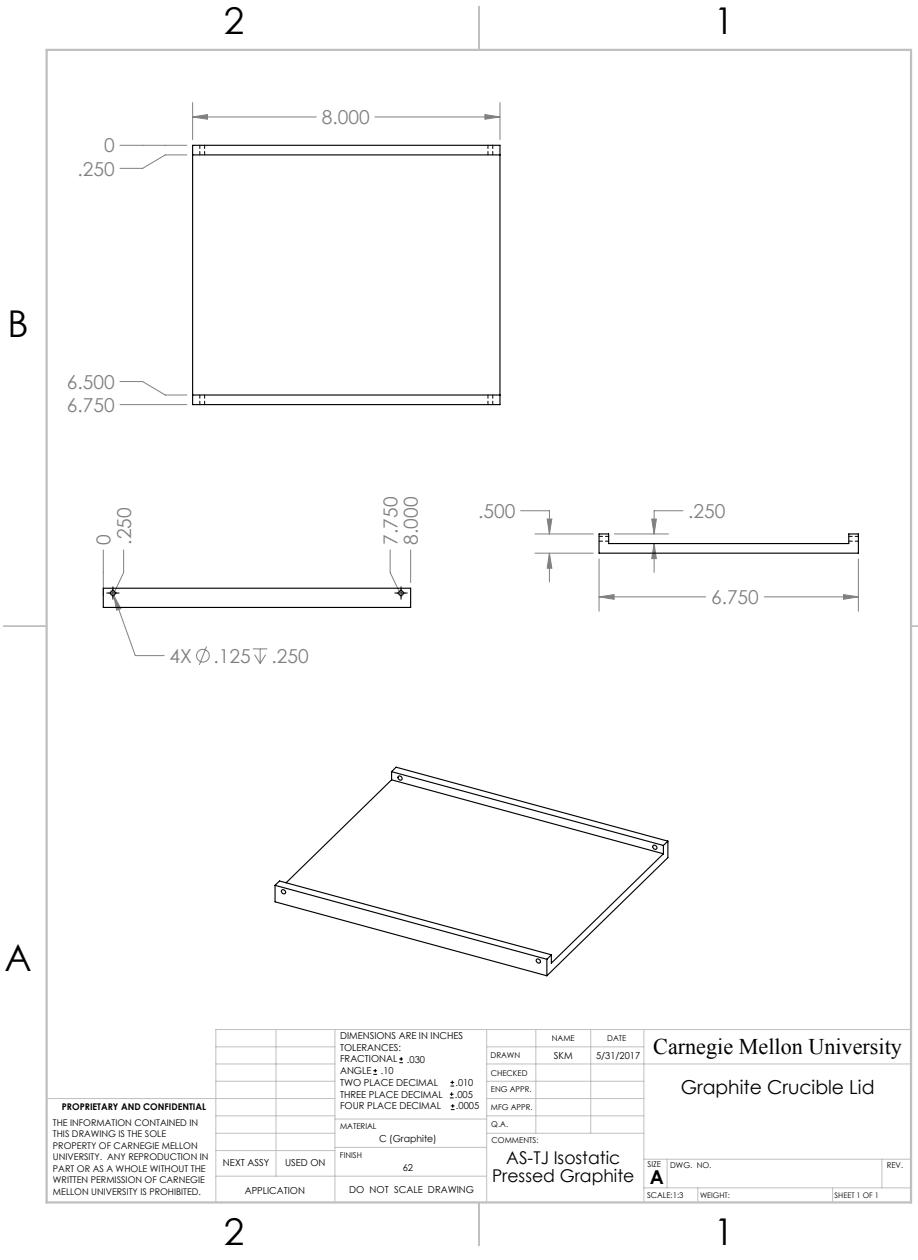

Figure D.2: Graphite Crucible Design

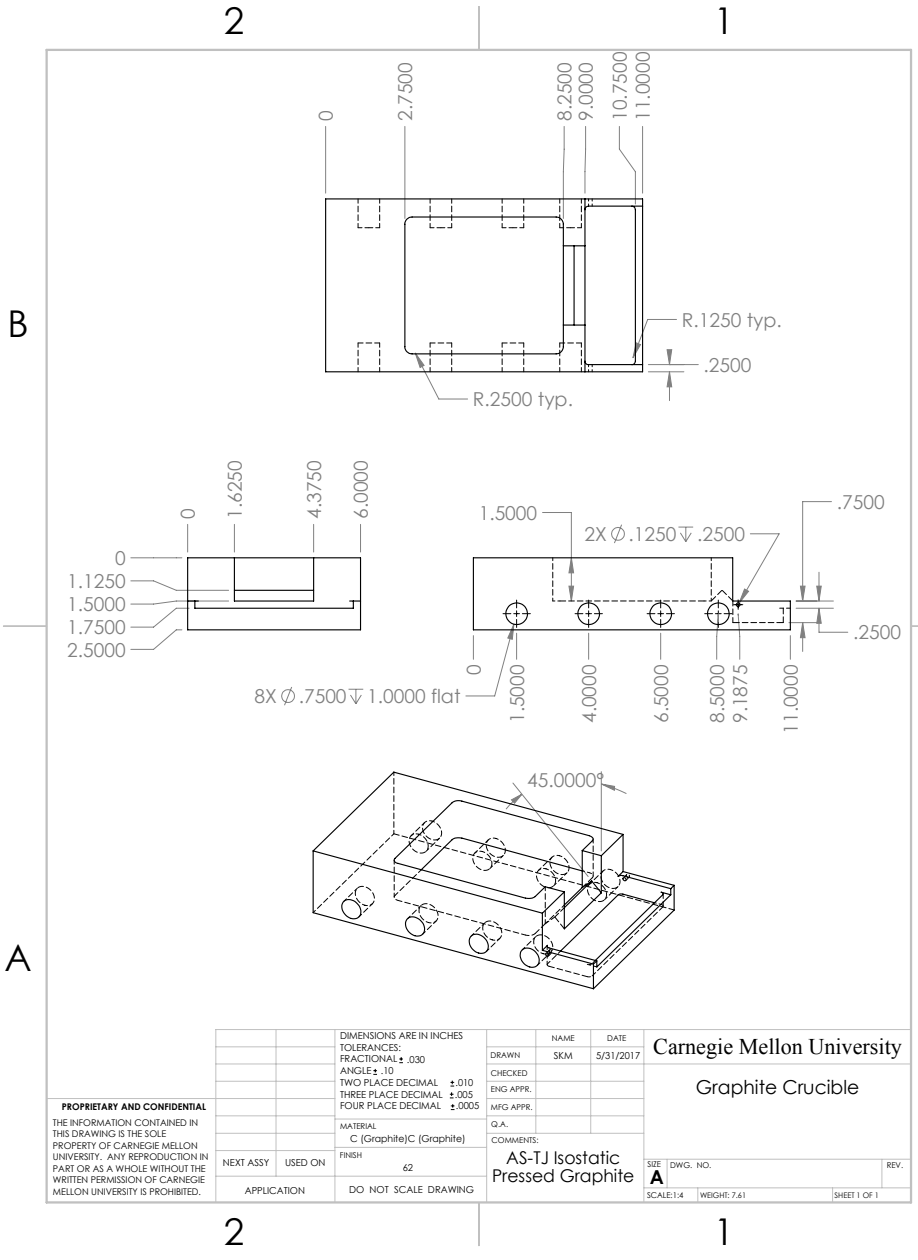

Figure D.3: Graphite Crucible Door Design

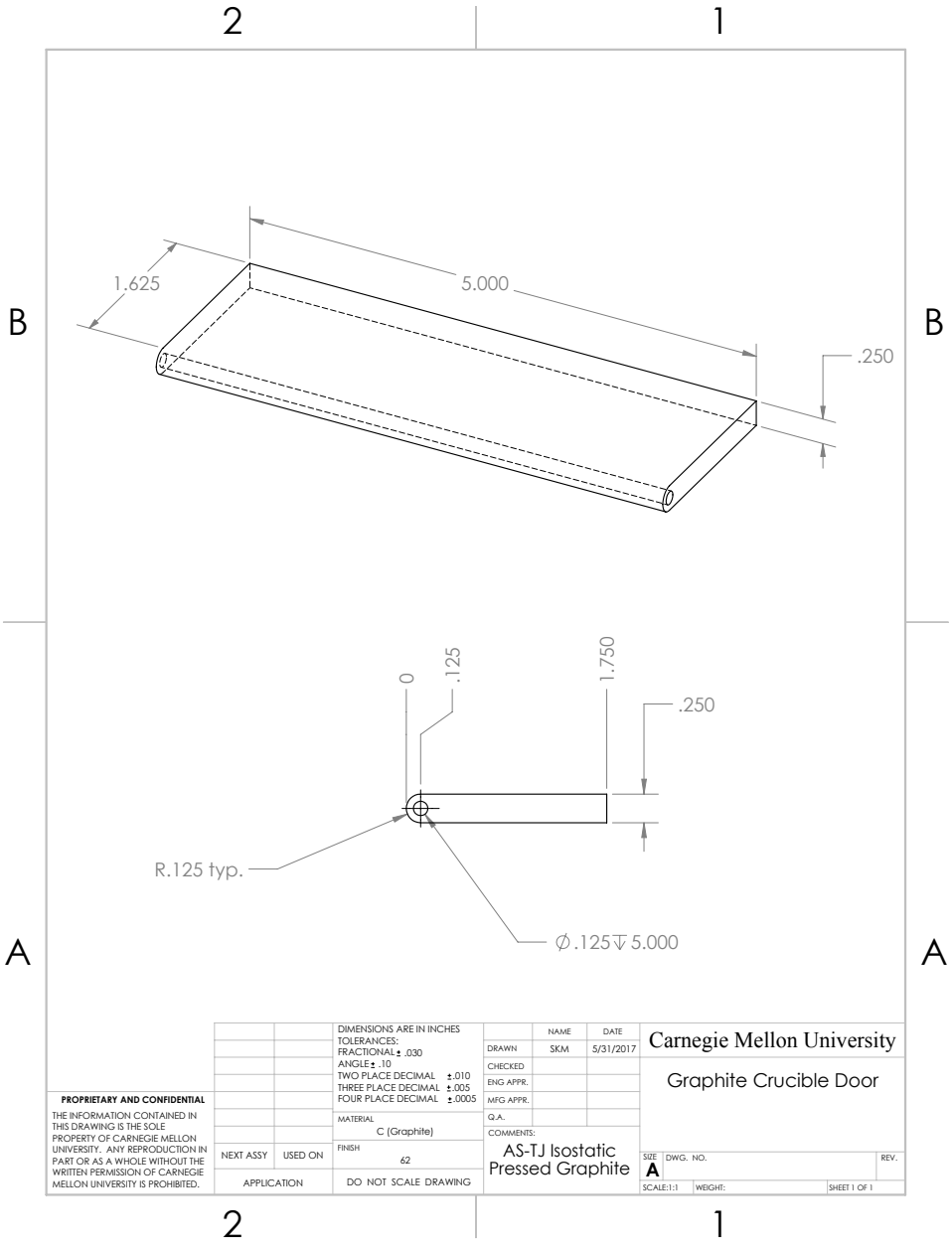

Standard Operating Procedure for Melting and Pulling trials

Switch on the Power: Switch on the Power for (1)Panel 4A (2)Control Disconnect (3)Control System (4)UPS (5)PLC control switch

Vacuum and backfill procedure

1. Switch off the backfill air valve and backfill argon valve.
2. Switch on the compressed air and check for the gauge pressure (> 40).
3. Switch on the vacuum pump and set the vacuum valve on.
4. Monitor the pressure drop until it reaches around -970 mbar.
5. Switch off the vacuum valve and set the vacuum pump off.
6. Open the backfill argon valve on the machine.
7. Open the backfill argon gas valves on the cylinder and adjust the pressure.
8. Monitor the pressure increase until it reaches positive pressure. The back vent will adjust the process pressure automatically.
9. Switch off the backfill argon flow when the system has reached steady state.

Pre-Experiment Procedure

1. Switch on the process argon flow, (Ar flow rate should be set at around 400).

2. Start temperature recording.

3. Switch on the cooling water valve (The main cooling water valve should be opened by 50% at the beginning).

4. Switch on the electrical cabinet, flip the invert switch, then switch on the power for the heater.

5. All alarm should be reseted (Increase the cooling water flow rate if error occurs).

Heating Procedure

Table D.1: HRG Heating Procedure

Process Temperature/Time	Ramp Rates (Lower Chamber)
Room Temperature (15 minutes)	Power Mode: 5%
15 minutes	Power Mode: 10%
15 minutes	Power Mode: 15%
Up to $300°C$	Power Mode: 20%
Up to $500°C$	Power Mode: 30%
Up to $800°C$	Power Mode: 40%
Up to $1200°C$	Power Mode: 50%
Up to $1400°C$	Power Mode: 60%
Up to $1500°C$	Power Mode: 75%
Process Temperature $\sim 1500°C$ until Crucible Temperature reaches $\sim 1500°C$	Power Mode: 75% or Switch to Temperature Mode if system alarm occurs
Pulling Condition	Power Mode: 50%

Cooling Procedure

- Gradually decrease the lower chamber power from 50% to 0% by reducing the power for 5% every 10 minutes.
- Keep the cooling water rate at its maximum at all time.
- Keep the cooling water and process power on for at least one more hour after the process temperature drops below $250°C$.

Typical Problems and Errors

1. Insufficient cooling water: Increase the overall water flow; Check the corresponding error message in the control system and adjust the water flow in corresponding section (typically try to keep the cooling water flow in the shell and induction coil section high); If the problem persist, check the mass flow meter for the cooling water outlet and control signal.
2. Heating modes: Use power mode at the beginning of the heating procedure and switch to temperature mode when getting close to the melting point. Power mode heating provides less intensive heating that can avoid potential power outage, while temperature mode heating will use the highest possible power to reach the target temperature.
3. Heating power error: reset all alarms to eliminate false alarms; If the error message persist: switch off all power and reset it to 0%; reset all alarms then adjust the power back to the original value.
4. Pressure increase: During the heating process, the process pressure may slightly increase to around 90 mbar. This pressure needs to be closely monitored at all time during the heating process. One cause for the

pressure increase could be the blocked back gas vent by the cooling water pipes.

5. Inert Gas protection: Check the pressure of two argon gas cylinders for backfill flow and process flow to make sure there is sufficient protection gas for one full experiment (including heating process and cooling down); One additional vacuum procedure should be performed if a full experiment is planned; Argon process flow rate should be increased to ensure a positive process pressure before trying to open the exit door and start a pulling test.

Post-Experiment Procedure

1. Switch off the cooling water pipe.
2. Switch off the argon flow from the control panel and the gas cylinder valves.
3. Switch off the control software, computer, control box switch, UPS, and power switches.

Appendix E

Water-Ice HRG system Experiment

Current Crucible Design

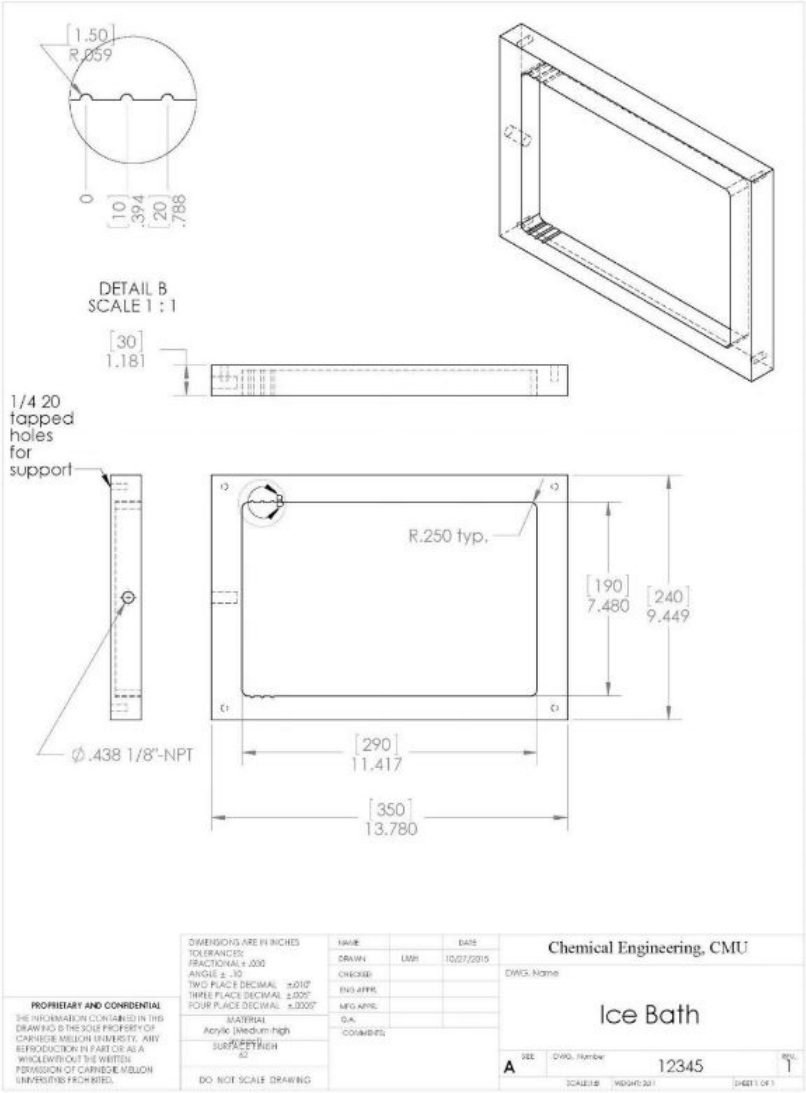

Figure E.1: Water-Ice system Crucible Design.

Supplementary photos for the Water-Ice HRG system

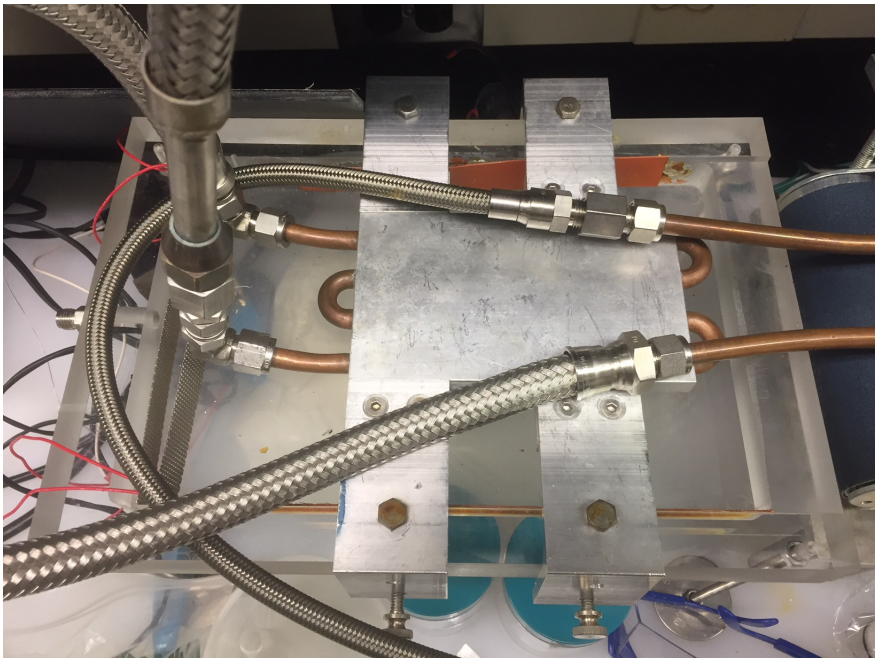

Figure E.2: Water-Ice system main bath top view: Main bath, cooling plate and pipes, heating strips, mesh flow breaker.

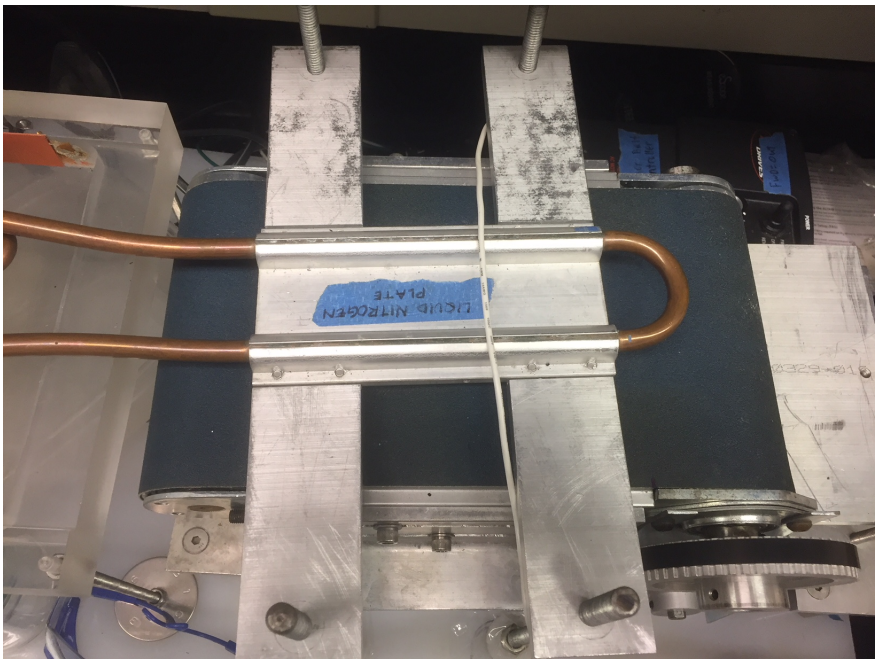

Figure E.3: Water-Ice pulling system top view: conveyable belt with sand paper, additional cooling plate.

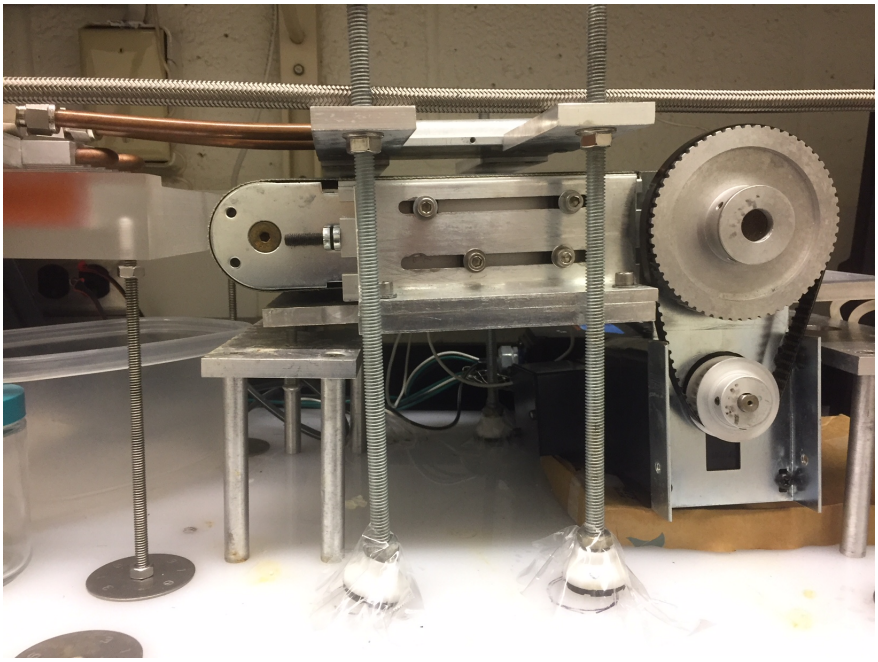

Figure E.4: Water-Ice pulling system side view: the distance and height of pulling stand is adjusted to ensure positive pulling angle.

Appendix F

Preliminary Control design

Control Strategy

In the HRG process, one of the major targets is the stable production of thin wafer, which is correlated with the cooling condition/rate and the withdraw speed of the thin wafer. Meanwhile, the wedge factor (length/thickness) of the thin wafer have an indication for the stability of the operating condition, which is further correlated with the lower meniscus shape in the HRG process. Currently, our attention about this control problem mainly focuses on the crystal wafer and we define the wedge shape wafer as our system of interest. The mass and energy balance for the solid crystal can be represented as:

$$\frac{dM_s}{dt} = \dot{P}s - v_s\rho\delta w, \tag{F.1}$$

—

$$\frac{dU}{dt} = Q_0 - Q_c - H_s v_s \rho \delta w. \tag{F.2}$$

where M_s and U are the total mass and internal energy, respectively, of the solid crystal in the system. The output is the thickness of the produced wafer.

We treat the pulling velocity v_s and the cooling rate Q_c as the manipulated variables(MVs), no disturbances(DVs) is assumed for the system. The measurement of crystallization rate $\dot{P}s$ and heat conduction from the melt Q_0 is not reliable. Thus, they are treated as unmeasured disturbances. In addition, the cooling rate can be further manipulated by the cooling temperature T_c.

System Identification And RGA

In order to better understand the system behavior, a step change analysis is performed for transfer function models estimation. A relative gain array (RGA) method is used to determine the best pairing. Open-loop analyses are performed to study the response of the system. As shown in Figure F.1, a pulling velocity step change is performed while the cooling temperature is kept constant. The transfer function is found by a Matlab nonlinear optimization solver. Following the same procedure, the system close to a certain operation point(v_s from $120-150(mm/min)$ and T_c from $190-230K$) can be represented as the following transfer function model. It is notable that this transfer function model highly depends on the operating points since the system is highly nonlinear. RGA analysis is performed using this transfer function model.

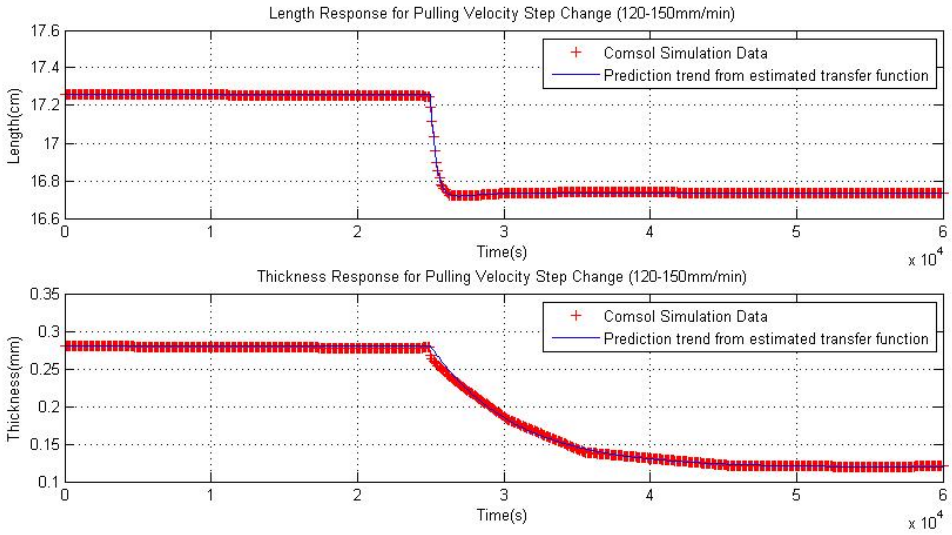

Figure F.1: Transfer Function Estimation from step change analysis (Pulling Velocity)

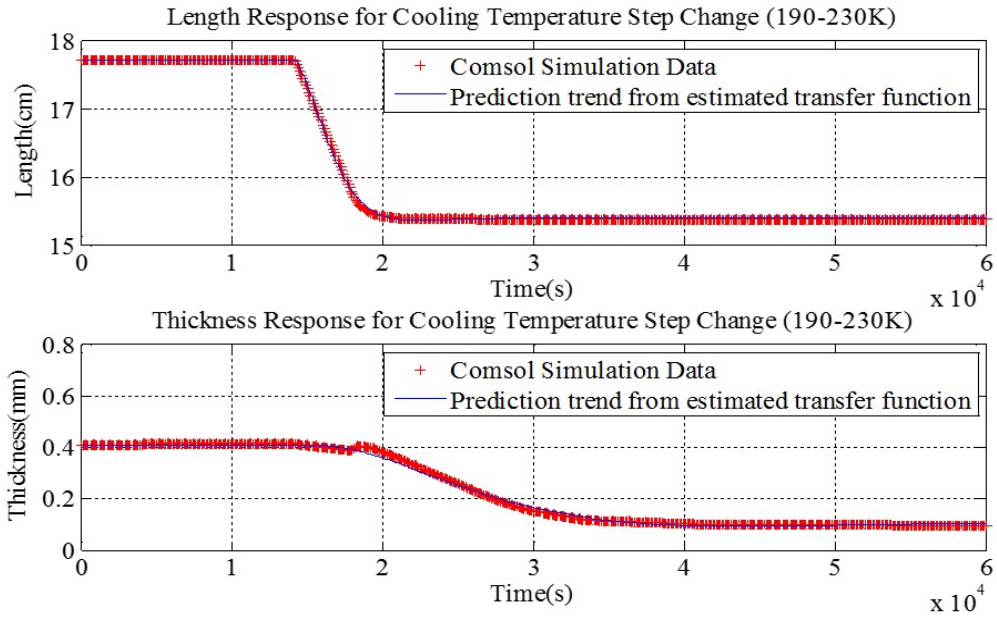

Figure F.2: Transfer Function Estimation from step change analysis (Cooling Temperature)

$$G(s) = \begin{bmatrix} \frac{-0.05826\cdot(56.72s+1)}{99700s^2+512.2s+1} & \frac{-0.0173\cdot(422s+1)}{(385.187s+1)(78.1029s+1)} \\ \frac{-0.007547\cdot\exp(-1500s)}{(908.8s+1)(474.7s+1)} & \frac{-0.005386}{1120s+1} \end{bmatrix} \tag{F.3}$$

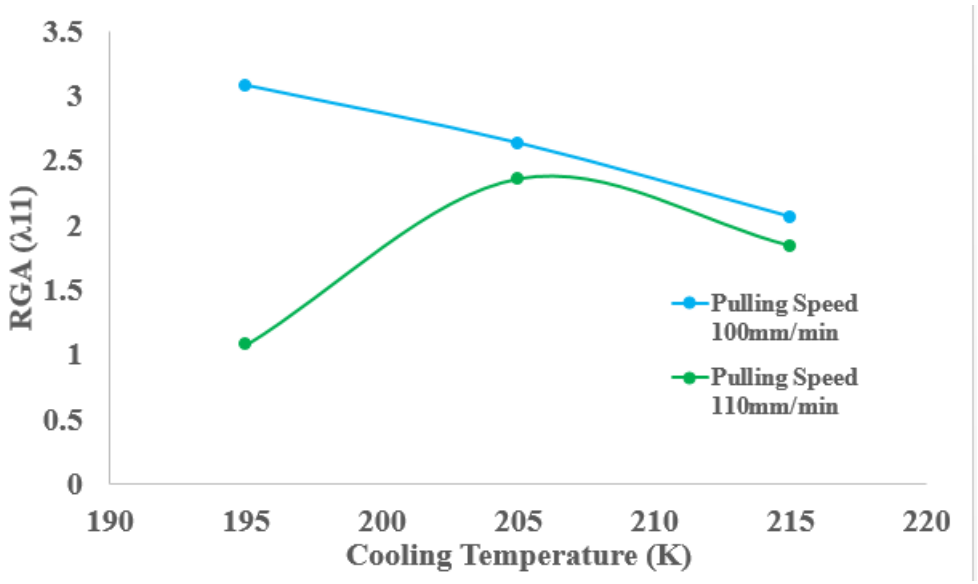

Figure F.3: RGA analysis at different operating conditions

The relative gain array (RGA) is a normalized gain matrix between the impact of each CVs on the output and its impact on other variables. For a MIMO (multi-input-multi-output) system, the RGA method can be used to determine the optimal input-output variable pairings. We performed RGA analysis to determine the pairings of the multi-loop feedback control scheme. As shown in Figure F.3, the RGA analysis highly depends on the operating conditions.

Implementation of Adaptive Controller

Our previous control study for the water-ice ribbon growth process is a simple feedback PI control scheme. Now we define:

$$y = \begin{bmatrix} \delta \\ l \end{bmatrix},$$

$$Z = \begin{bmatrix} M_s \\ U_s \end{bmatrix},$$

$$u = \begin{bmatrix} v_s \\ Q_c \end{bmatrix}.$$

Then we can write the time derivative of Z as:

$$\frac{dZ}{dt} = u + \theta^T \mu(x, d), \tag{F.4}$$

where

$$\theta = (\theta_1, \theta_2)^T, \tag{F.5}$$

$$\mu(x, d) = (\dot{P}_s, Q_0)^T. \tag{F.6}$$

The measurement functions are:

$$Z = \begin{bmatrix} M_s \\ U_s \end{bmatrix} = \begin{bmatrix} \frac{1}{2}\delta l w \rho_s \\ \frac{1}{2}\alpha \rho l w T C_p \end{bmatrix}. \tag{F.7}$$

Thus, the inventory Z can be estimated from the measurement of output y. And the setpoint Z^* is constant. So we can derive our control law as following:

$$u = -\hat{\theta}^T \mu(x, d). \tag{F.8}$$

and θ can be estimated on-line by using the following procedure.

Define the Lyapunov function of close-loop system as follows:

$$V = \frac{1}{2}e^2 + \frac{1}{2}(\theta - \hat{\theta})^T G^{-1}(\theta - \hat{\theta}), \tag{F.9}$$

where

$$\begin{aligned} e &= Z^* - Z \\ , G &= diag(g_1, g_2). \end{aligned} \tag{F.10}$$

Then together with Eqn. (F.1) and (F.2), we have,

$$\begin{aligned} \frac{dV}{dt} &= (M_s - M_s^*)\frac{dMs}{dt} + (U_s - U_s^*)\frac{dU_s}{dt} + \frac{1}{g_1}(\hat{\dot{P}s} - \dot{P}s)\frac{d\hat{P}s}{dt} + \frac{1}{g_2}(\hat{Q}_0 - Q_0)\frac{d\hat{Q}_0}{dt} \\ &= (M_s - M_s^*)(\hat{P}s - v_s\delta w\rho + Ps - \hat{P}s) + (U_s - U_s^*)(\hat{Q}_0 - Q_c - H_s v_s \delta w \rho + Q_0 - \hat{Q}_0) \\ &\quad + \frac{1}{g_0}(\hat{\dot{P}s} - \dot{P}s)\frac{\hat{dP}s}{dt} + \frac{1}{g_2}(\hat{Q}_0 - Q_0)\frac{d\hat{Q}_0}{dt}. \end{aligned}$$

So we can define the unknown parameter estimation as:

$$\frac{d\hat{\dot{P}}s}{dt} = -g_1(M_s^* - M_s), \tag{F.11}$$

$$\frac{d\hat{Q}_0}{dt} = -g_2(U_s^* - U_s). \tag{F.12}$$

where g_1 and g_2 are control tuning parameters.

The proposed control scheme for the HRG process is preseneted in Figure F.4.

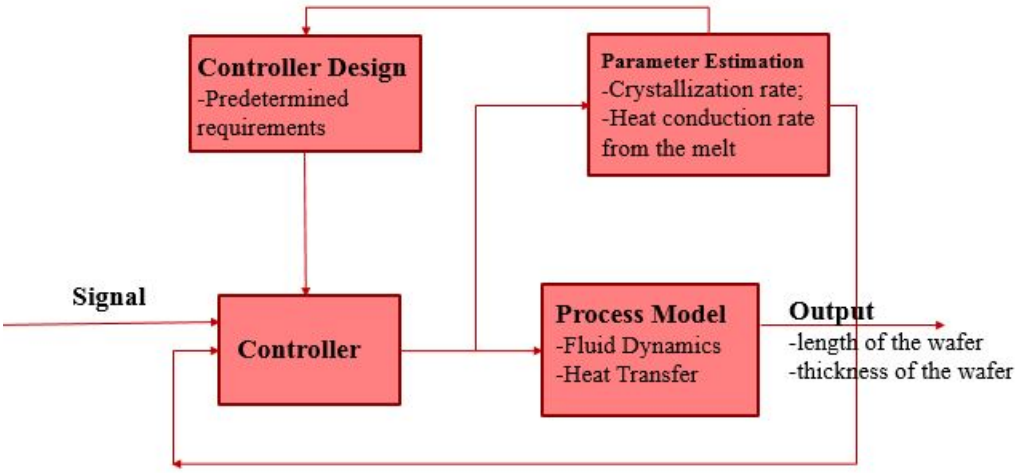

Figure F.4: The proposed control Scheme for the HRG process

Simulation Results

The ice-water HRG process with adaptive controller is simulated in COMSOL Multi-physics environment (4.4) and coupled with Matlab R2013a. The process model built in COMSOL is based on the governing equations proposed previously. A simple feedback PI controller was tested at the beginning. The output of the model with this PI controller is presented in Figure F.5. Corresponding manipulated variables are shown in Figure F.6.

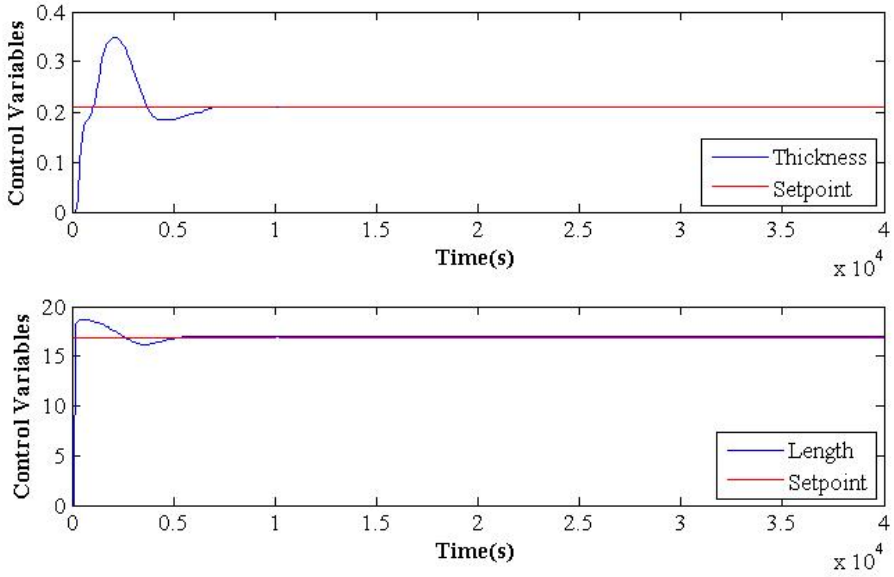

Figure F.5: The outputs of the model with PI control

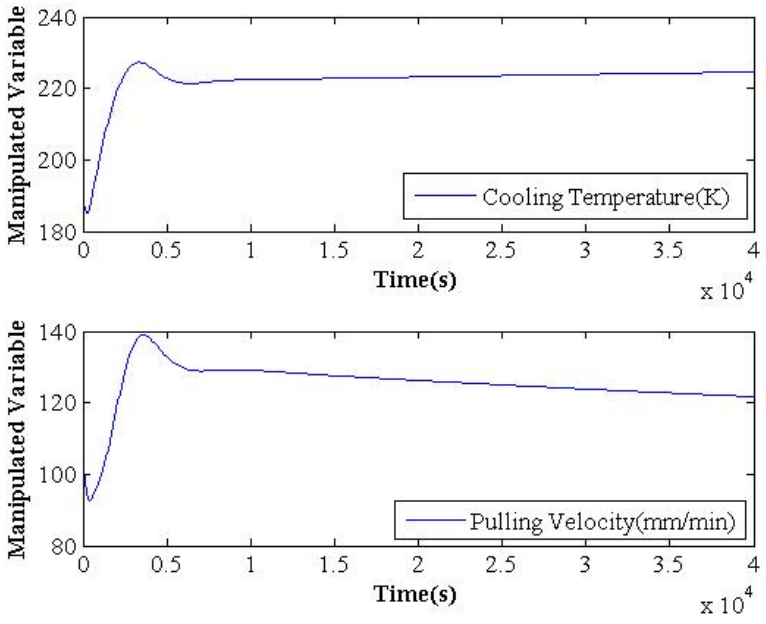

Figure F.6: The inputs of the model with PI control

It is notable that the performance of multiloop PI control scheme cannot meet our requirements. The two manipulated variables are not stable even when the control targets have been achieved. This is due to the highly coupled states feature of the HRG system.

Then the adaptive control strategy is applied. Corresponding performance comparison of the output results and inputs are shown in Figure F.7 and F.8. The performance of the adaptive controller is much better than the previous PI control scheme. In particular, the control objective here is to produce ribbon with specific length ($17cm$) and thickness ($0.21mm$). The results show that adaptive control can eliminate the undesired control loop interactions shown in the previous PI control scheme.

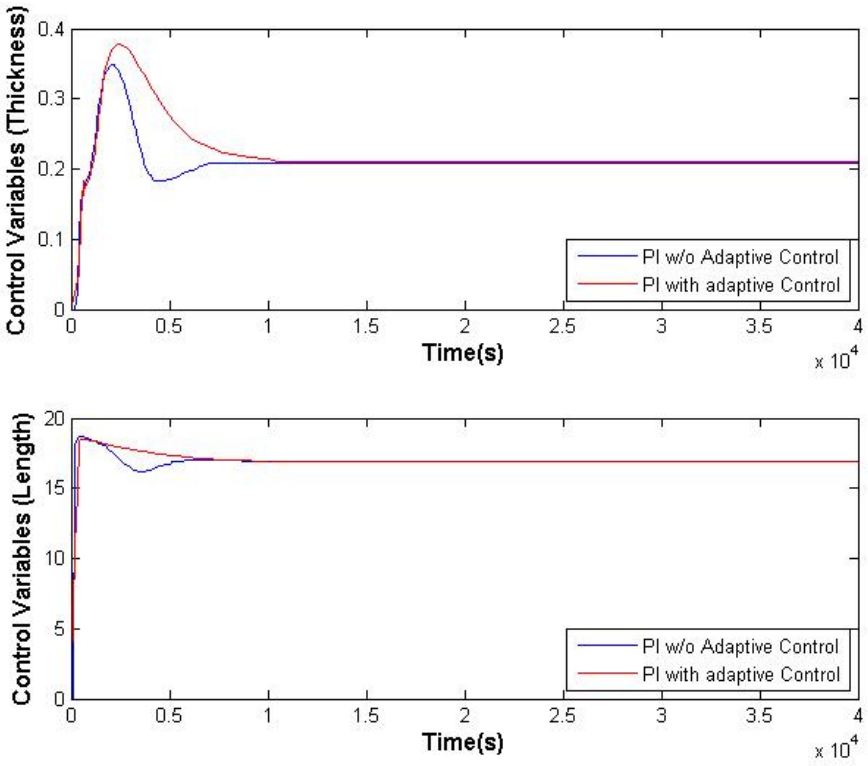

Figure F.7: The outputs of adaptive control

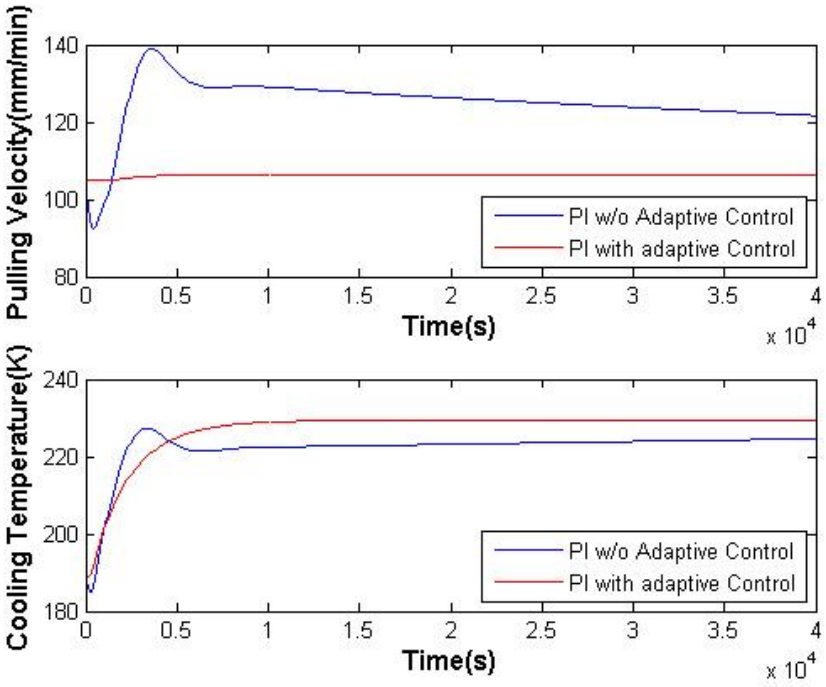

Figure F.8: The inputs of adaptive control

The setpoint step change analysis is then performed and the output responses are presented in Figure F.9.

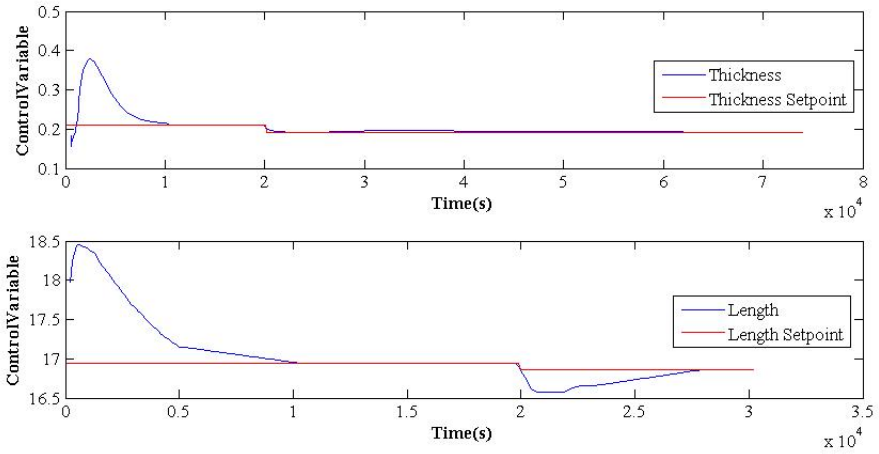

Figure F.9: Step change test for adaptive control

Bibliography

[1] D.K. Bandyopadhyay, D.M. Stefanescu, I. Minkoff, S.K. Biswal, G. Ohira, T. Kusakawa, and E. Niyama (Eds.). Physical metallurgy of cast iron iv. *Proceedings of the Materials Research Society*, page 27, 1989.

[2] RO Bell and JP Kalejs. Growth of silicon sheets for photovoltaic applications. *Journal of materials research*, 13(10):2732–2739, 1998.

[3] Lazaro Beltran-Sanchez and Doru M Stefanescu. A quantitative dendrite growth model and analysis of stability concepts. *Metallurgical and Materials Transactions A*, 35(8):2471–2485, 2004.

[4] C Bleil. Horizontal growth of crystal ribbons, September 18 1973. US Patent 3,759,671.

[5] CE Bleil. A new method for growing crystal ribbons. *Journal of Crystal Growth*, 5(2):99–104, 1969.

[6] Robert A Brown. Theory of transport processes in single crystal growth from the melt. *AIChE Journal*, 34(6):881–911, 1988.

[7] PC Carman. Fluid flow through granular beds. *Chemical Engineering Research and Design*, 75:S32–S48, 1997.

[8] Bruno Ceccaroli and Otto Lohne. Solar grade silicon feedstock. *Handbook*

of Photovoltaic Science and Engineering, Second Edition, pages 169–217, 2011.

[9] David P Chock. Direct integration method applied to soret-driven instability. *Physics of Fluids (1958-1988)*, 18(11):1401–1406, 1975.

[10] TF Ciszek. Edge-defined, film-fed growth (efg) of silicon ribbons. *Materials Research Bulletin*, 7(8):731–737, 1972.

[11] Roger F Clark. Method and apparatus for the production of crystalline silicon substrates, September 11 2012. US Patent 8,262,795.

[12] SR Coriell, MR Cordes, WJ Boettinger, and RF Sekerka. Convective and interfacial instabilities during unidirectional solidification of a binary alloy. *Journal of Crystal Growth*, 49(1):13–28, 1980.

[13] SR Coriell, GB McFadden, RF Boisvert, and RF Sekerka. Effect of a forced couette flow on coupled convective and morphological instabilities during unidirectional solidification. *Journal of crystal growth*, 69(1):15–22, 1984.

[14] Parthiv Daggolu, Andrew Yeckel, Carl E Bleil, and Jeffrey J Derby. Thermal-capillary analysis of the horizontal ribbon growth of silicon crystals. *Journal of Crystal Growth*, 355(1):129–139, 2012.

[15] Parthiv Daggolu, Andrew Yeckel, Carl E Bleil, and Jeffrey J Derby. Stability limits for the horizontal ribbon growth of silicon crystals. *Journal of Crystal Growth*, 363:132–140, 2013.

[16] Parthiv Daggolu, Andrew Yeckel, and Jeffrey J Derby. An analysis of segregation during horizontal ribbon growth of silicon. *Journal of Crystal Growth*, 390:80–87, 2014.

[17] SN Dermatis and JW Faust. Semiconductor sheets for the manufacture of semiconductor devices. *Transactions of the American Institute of Electrical Engineers, Part I: Communication and Electronics*, 82(1):94–98, 1963.

[18] Ch-A Gandin and Michel Rappaz. A coupled finite element-cellular automaton model for the prediction of dendritic grain structures in solidification processes. *Acta metallurgica et materialia*, 42(7):2233–2246, 1994.

[19] Ch-A Gandin and Michel Rappaz. A 3d cellular automaton algorithm for the prediction of dendritic grain growth. *Acta Materialia*, 45(5):2187–2195, 1997.

[20] Frédéric Gibou, Ronald Fedkiw, Russel Caflisch, and Stanley Osher. A level set approach for the numerical simulation of dendritic growth. *Journal of Scientific Computing*, 19(1-3):183–199, 2003.

[21] Brian T Helenbrook and Nathaniel S Barlow. Spatial–temporal stability analysis of faceted growth with application to horizontal ribbon growth. *Journal of Crystal Growth*, 454:35–44, 2016.

[22] Brian T Helenbrook, Peter Kellerman, Frederick Carlson, Nandish Desai, and Dawei Sun. Experimental and numerical investigation of the horizontal ribbon growth process. *Journal of Crystal Growth*, 453:163–172, 2016.

[23] Damir Juric and Grétar Tryggvason. A front-tracking method for dendritic solidification. *Journal of computational physics*, 123(1):127–148, 1996.

[24] Alain Karma and Wouter-Jan Rappel. Quantitative phase-field modeling

of dendritic growth in two and three dimensions. *Physical review E*, 57 (4):4323, 1998.

[25] Peter Kellerman. Floating silicon method. Technical report, Applied Materials-Varian Semiconductor Equipment, 2013.

[26] Peter Kellerman, Brian Kernan, Brian T Helenbrook, Dawei Sun, Frank Sinclair, and Frederick Carlson. Floating silicon method single crystal ribbon–observations and proposed limit cycle theory. *Journal of Crystal Growth*, 451:174–180, 2016.

[27] W Koch, AL Endrös, D Franke, C Häßler, JP Kalejs, and HJ Möller. Bulk crystal growth and wafering for pv. *Handbook of photovoltaic science and engineering*, pages 205–252, 2003.

[28] B Kudo. Improvements in the horizontal ribbon growth technique for single crystal silicon. *Journal of Crystal Growth*, 50(1):247–259, 1980.

[29] W 1 Kurz, B Giovanola, and R Trivedi. Theory of microstructural development during rapid solidification. *Acta metallurgica*, 34(5):823–830, 1986.

[30] H Lange and IA Schwirtlich. Ribbon growth on substrate (rgs)a new approach to high speed growth of silicon ribbons for photovoltaics. *Journal of Crystal Growth*, 104(1):108–112, 1990.

[31] Jean Claude Legros, D Longree, Guy Chavepeyer, and Jean Karl Platten. On the two-component benard problem a numerical solution. *Physica A: Statistical Mechanics and its Applications*, 80(1):76–88, 1975.

[32] Peter J Linstrom and WG Mallard. Nist chemistry webbook; nist standard reference database no. 69. 2001.

[33] Y Liu, T Baudin, and R Penelle. Simulation of normal grain growth by cellular automata. *Scripta Materialia*, 34(11), 1996.

[34] William W Mullins and RF Sekerka. Stability of a planar interface during solidification of a dilute binary alloy. *Journal of applied physics*, 35(2): 444–451, 1964.

[35] L Nastac. Numerical modeling of solidification morphologies and segregation patterns in cast dendritic alloys. *Acta Materialia*, 47(17):4253–4262, 1999.

[36] German A Oliveros, Ruochen Liu, Seetharaman Sridhar, and B Erik Ydstie. Silicon wafers for solar cells by horizontal ribbon growth. *Industrial & Engineering Chemistry Research*, 52(9):3239–3246, 2013.

[37] German A Oliveros, Seetharaman Sridhar, and B Erik Ydstie. Existence and static stability of the meniscus in horizontal ribbon growth. *Journal of Crystal Growth*, 411:96–105, 2015.

[38] German Andrés Oliveros Patiño. Modeling and stability of the horizontal ribbon growth process. 2014.

[39] Suhas Patankar. *Numerical heat transfer and fluid flow*. CRC Press, 1980.

[40] Doug M Powell, Mark T Winkler, HJ Choi, Christie B Simmons, D Berney Needleman, and Tonio Buonassisi. Crystalline silicon photovoltaics: a cost analysis framework for determining technology pathways to reach baseload electricity costs. *Energy & Environmental Science*, 5(3):5874–5883, 2012.

[41] Weilin Qu, Gh Mohiuddin Mala, and Dongqing Li. Heat transfer for water

flow in trapezoidal silicon microchannels. *International Journal of Heat and Mass Transfer*, 43(21):3925–3936, 2000.

[42] S Ranjan, S Balaji, Rocco A Panella, and B Erik Ydstie. Silicon solar cell production. *Computers & Chemical Engineering*, 35(8):1439–1453, 2011.

[43] REN21.2017. *Renewables 2017 Global Status Report*. Paris:REN21 Secretariat, 2017.

[44] R Sasikumar and R Sreenivasan. Two dimensional simulation of dendrite morphology. *Acta Metallurgica et Materialia*, 42(7):2381–2386, 1994.

[45] A Schonecker, L Laas, A Gutjahr, P Wyers, A Reinink, and B Wiersma. Ribbon-growth-on-substrate: Progress in high-speed crystalline silicon wafer manufacturing. In *Photovoltaic Specialists Conference, 2002. Conference Record of the Twenty-Ninth IEEE*, pages 316–319. IEEE, 2002.

[46] Andreas Schönecker, LJ Geerligs, and Armin Müller. Casting technologies for solar silicon wafers: block casting and ribbon-growth-on-substrate. In *Solid State Phenomena*, volume 95, pages 149–158. Trans Tech Publ, 2004.

[47] RG Seidensticker and RH Hopkins. Silicon ribbon growth by the dendritic web process. *Journal of Crystal Growth*, 50(1):221–235, 1980.

[48] William. Shockley. Process for growing single crystals. *U.S. Patent 3,031,275, 24*, April 1959.

[49] D.M. Stefanescu, H. Fredriksson, and M. Hillert (Eds.). The physical metallurgy of cast iron. *Proceedings of the Materials Research Society*, 34:151, 1985.

[50] Paul D Thomas and Robert A Brown. Rate limits in silicon sheet growth:

the connections between vertical and horizontal methods. *Journal of Crystal Growth*, 82(1-2):1–9, 1987.

[51] Vaughan R Voller and C Prakash. A fixed grid numerical modelling methodology for convection-diffusion mushy region phase-change problems. *International Journal of Heat and Mass Transfer*, 30(8):1709–1719, 1987.

[52] W Wang, Peter D Lee, and M_ Mclean. A model of solidification microstructures in nickel-based superalloys: predicting primary dendrite spacing selection. *Acta materialia*, 51(10):2971–2987, 2003.

[53] Oleg Weinstein and Simon Brandon. Dynamics of partially faceted melt/crystal interfaces i: computational approach and single step–source calculations. *Journal of crystal growth*, 268(1-2):299–319, 2004.

[54] Adam A Wheeler, Bruce T Murray, and Robert J Schaefer. Computation of dendrites using a phase field model. *Physica D: Nonlinear Phenomena*, 66(1-2):243–262, 1993.

[55] David Phillip Woodruff. *The solid-liquid interface*. CUP Archive, 1973.

[56] MF Zhu and CP Hong. A modified cellular automaton model for the simulation of dendritic growth in solidification of alloys. *Isij International*, 41(5):436–445, 2001.

[57] MF Zhu, SY Lee, and CP Hong. Modified cellular automaton model for the prediction of dendritic growth with melt convection. *Physical Review E*, 69(6):061610, 2004.

[58] John A Zoutendyk. Theoretical analysis of heat flow in horizontal ribbon growth from a melt. *Journal of Applied Physics*, 49(7):3927–3932, 1978.

[59] John A Zoutendyk. Analysis of forced convection heat flow effects in horizontal ribbon growth from the melt. *Journal of Crystal Growth*, 50 (1):83–93, 1980.